Design, Development, and Testing of a Stochastically Modulated Raman Spectrometer

by

Michael J. Zervas

B.S., Worcester Polytechnic Institute (2010)
M.S., Worcester Polytechnic Institute (2011)

Submitted to the Department of Mechanical Engineering
in partial fulfillment of the requirements for the degree of

Doctor of Philosophy in Mechanical Engineering

at the

MASSACHUSETTS INSTITUTE OF TECHNOLOGY

June 2019

Author .... Signature redacted ......
Department of Mechanical Engineering
May 1, 2019

Certified by.................. Signature redacted ....
Ian W. Hunter
George N. Hatsopoulos Professor in Thermodynamics
Thesis Supervisor

Accepted by .... Signature redacted ....
Nicolas G. Hadjiconstantinou
Chairman, Department Committee on Graduate Theses

Design, Development, and Testing of a Stochastically Modulated Raman Spectrometer

by

Michael J. Zervas

Submitted to the Department of Mechanical Engineering
on May 1, 2019, in partial fulfillment of the
requirements for the degree of
Doctor of Philosophy in Mechanical Engineering

Abstract

Detection of cancerous tumors and identification of counterfeit medications are just two examples that demonstrate the chemical specificity provided by Raman Spectroscopy. Yet, the widespread use of Raman Spectroscopy as an analytical tool has been limited to large bench-top systems in controlled laboratory environments. Existing technology, specifically in portable or handheld formats, suffers from a high false detection rate and relatively low sensitivity compared to other spectroscopic techniques.

The present work addresses these issues through the design and development of a new system architecture that stochastically modulates the laser excitation wavelength. Small changes in excitation will proportionally shift the Raman scatter while having little effect on other spectral artifacts, including fluorescence. A custom confocal Raman Spectrometer was built and characterized that can rapidly shift the excitation wavelength by selectively straining an externally mounted Fiber Bragg Grating (FBG). When combined with a superluminescent diode (SLED), a modulation bandwidth of over half a nanometer was achieved. The functionality of the system was tested and benchmarked against Raman spectra that have been well characterized in literature. In addition, a novel signal processing approach was used to obtain a difference spectrum from a stochastic input excitation sequence. Simulations were conducted that compare the performance to conventional methods, which were then verified experimentally. Results indicate that the stochastic modulation was able to effectively isolate Raman scatter with a higher SNR compared to conventional methods.

Finally, it was demonstrated that the developed system could be applied to Surface Enhanced Raman Spectroscopy (SERS). SERS substrates increase the Raman scatter signal, but also compete with significant fluorescence and a strong background signal. Rhodamine 6G, a fluorescent dye, was tested using the developed system on a SERS substrate. Concentrations on the order of several hundred parts per million (ppm) were successfully measured, with significantly lower limits of detection possible. The experimental data shows that the combination of SERS with stochastically modulated techniques reduces the false detection rate and improves the detection sensitivity by several orders of magnitude, addressing both of the major existing limitations.

Thesis Supervisor: Ian W. Hunter
Title: George N. Hatsopoulos Professor in Thermodynamics

Acknowledgments

The time I've spent at MIT has been one of the most valuable experiences I've had in my life. I've become a better engineer and scientist and built long-lasting relationships with many people in the MIT community. I owe the biggest thanks to my Advisor, Professor Ian Hunter, who is truly someone I admire for both his extraordinary ambition and his character. Ian's support has been unwavering and the resources and research independence he has provided have given me the opportunity to explore some of the most challenging problems. I would also like to thank the members of my thesis committee - Doug Hart, Mathias Kolle, and Harry Hemond - for their guidance, feedback, and encouragement throughout the research process. They helped significantly to define the scope and focus of my research.

There are many other's I would like to thank at MIT, which includes other members of the MIT Bioinstrumentation Lab - Cathy Hogan, Nick Demas, Craig Cheney, Ashley Raynal, Geehoon Park, Ashin Modak, John Liu, and the many visiting students that I've interacted with from all over the world throughout the years. They have all contributed most significantly to my breadth of knowledge I've gained at MIT. I would also like to thank Leslie Regan, Una Sheehan, and Shibani Joshi who have been helpful and supportive throughout my time here at MIT. In addition, I would like to thank MIT Lincoln Laboratory for their support through the Lincoln Scholars Program and for the freedom they've provided in pursuing my research interests. Specifically, I would like to thank Mike Shatz, Dennis Burianek, Ken Estabrook, and Jim Ward for advocating for and supporting my educational objectives.

Finally, I would like to thank my friends and family for their unconditional support. In particular, I would like to thank my parents for their patience and guidance. I admire them for their hard work and persistence - they truly lead by example. Most importantly, I would like to thank my fiancé, Corinna, for her unconditional love and constant encouragement. She has been supportive in so many ways - providing feedback on my many presentations and motivation during the most challenging times. Thank you!

THIS PAGE INTENTIONALLY LEFT BLANK

Contents

List of Figures

List of Tables

THIS PAGE INTENTIONALLY LEFT BLANK

Chapter 1

Introduction

A broad range of disciplines are dependent upon chemical sensing technology. Consequently, there has been significant growth in detection technologies and capabilities. Yet, a growing number of applications, some of which are described below, require further innovation and development.

1.1 Motivation

Chemical and biological detection and identification has become increasingly important for a wide range of fields over recent years and will continue to grow. One example is the rapid spread of counterfeit medicines, which can pose a significant health risk [17]. In the United States, the Food and Drug Administration (FDA) works with other government agencies and companies to prevent the spread of counterfeit medicines. Development of rapid detection techniques will support the agency's mission and help to prevent the spread of these illegal drugs. Another example is in the detection of explosive materials to counter the growing threat of global terrorism [18, 19, 20]. These materials can be in the form of airborne aerosols or solid chemical composition. Effective prevention and treatment requires early and rapid detection.

The importance of chemical and biological detection in other industries is also worth noting. Drug development involves time-sensitive clinical research to ensure that the compound is safe and effective [21]. The use of a chemical and biological detection system has the potential to expedite this research period through active monitoring of interactions. Similarly, the food processing industry is highly regulated and could benefit from advanced detection capabilities of trace substances, such as mycotoxins or allergenic proteins. This is critical to reduce the spread of disease or accidental cross contamination of products that could lead to allergic reactions in certain individuals. Finally, forensic science could benefit greatly from rapid analysis of trace chemical and biological substances to provide evidence in active investigations. Examples can also be found in many other industries that demonstrate the significance and need for research in this area.

The examples described above can be used as a framework to develop requirements for a chemical and biological detection system. Across all disciplines, there is a focus on portability of these systems across many individuals with a focus on an ever decreasing size, weight, and power (SWaP). Historically, as the size of the device decreases, the limits of detection (LOD) increase, which results in lower sensitivity. The LOD typically increases from added environmental noise under field conditions and from reductions in device performance as there are trade offs in small formats. Improving the sensitivity for trace detection in a portable format is necessary for many applications. High specificity is required to differentiate between chemicals with close analogs and ensure low false detection rates. The Joint Science and Technology Office for Chemical and Biological Defense (JSTO-CBD) identifies "non-specific detection" as one of the key shortfalls of the state-of-the-art portable systems [22]. In addition, many of these chemical and biological samples can be in different phase states (i.e. solid, liquid, gas/aerosol) and the detection technique should be versatile to accommodate such states. Development of a system that has this type of versatility has been recognized as a significant challenge [23].

1.2 Applicable Technology

In evaluating applicable technologies, there is a specific focus on systems that can non-destructively detect multiple analytes in different phase states and with high molecular specificity in a single system. Although there are a number of potential technologies, many fall short in meeting all of these capabilities. One example is Mass Spectroscopy (MS), which categorizes molecules by their molecular weight. Yet, this technique is limited to the gas phase as it requires both ionization of the sample and that multiple analytes have different molecular weights [24]. Another example is UV-Vis Spectroscopy, which is an absorption technique that is capable of detecting organic and inorganic molecules in different phase states [25]. This technique is limited in the molecular specificity that can be achieved because of spectral broadening caused by the superposition of vibrational and rotational absorption states. Therefore, differentiating between close molecular analogs is challenging.

Operating in the infrared region using Fourier Transform Infrared (FT-IR) Spectroscopy could provide advantages. For instance, it has higher spectral resolution as the photon energy is lower and discretization of absorption bands from different vibrational and rotational energy levels becomes more apparent. Yet, FT-IR Spectroscopy is fundamentally limited by working in the Infrared wavelength range. Specifically, water is a significant absorber in the IR spectrum, which makes many *in-vivo* measurements impractical [26, 27]. Alternatively, Raman Spectroscopy provides the same high specificity with the ability to test samples non-destructively in different phase states, including water based samples. FT-IR Spectroscopy and Raman Spectroscopy are typically viewed as complementary techniques, since they both are related to molecular vibrations with complementary "selection rules". In the case of Raman Spectroscopy, a non-zero change in polarizability as a function of interatomic distance of the molecule results in scattering at a signature wavelength representative of the bond stiffness of the molecule. In the case of FT-IR Spectroscopy, a non-zero oscillating dipole moment from the molecule vibration causes selective photon absorption at a signature wavelength [28].

A comprehensive list of the most applicable technologies is presented in Table 1.1 along with their ability to meet the required capabilities outlined in the previous section. By comparing the chart above and the relative benefits of each technology, it becomes apparent that Raman Spectroscopy offers significant advantages and the

Table 1.1: Applicable Technology

Adaptable Technology	Specificity (Differentiation)	Non-Destructive	Multi-Analyte Detection	Sample Versatility
Surface Acoustic Wave	✗	✓	✗	✗
Mass Spectroscopy	✓	✗	✓	✗
Nuclear Magnetic Resonance	✓	✗	✓	✗
Absorption Spectroscopy:				
FT-IR	✓	✓	✓	✗
UV-Vis	✗	✓	✓	✓
Raman Spectroscopy	✓	✓	✓	✓

most promise in meeting the capability of the next generation of chemical detection devices. A deeper understanding of this technique is required to evaluate its limitations and explore options to mitigate those limitations.

1.3 Thesis Chapter Breakdown

For convenience, the proceeding chapters are outlined as follows. Chapter 2 will discuss the basic principles of Raman Spectroscopy. It will talk about the existing systems and their main limitations. The major novelties of this work will be highlighted in regards to the existing limitations. Then, Chapter 3 will talk about the design of a novel Raman Spectroscopy system architecture. It will highlight the advantages of the design and walk through the process of component selection and development of the system. Chapter 4 will then focus on the characterization at both the component level and system level. Chapter 5 will describe the data acquisition process and signal processing technique. The approach described in this work will be compared to conventional techniques. Results are shown in Chapter 6 and their significance and improvements compared to conventional methods are detailed and discussed. Finally, Chapter 7 will summarize the key findings and discuss future work.

Chapter 2

Theory: Raman Spectroscopy

Raman Spectroscopy is a non-contact measurement technique with high molecular specificity needed for many sensing applications. The theory behind this technique, its practical implementation, and the corresponding limitations are described in the proceeding sections.

2.1 Classical Theory

When a light source interacts with matter, both elastic and inelastic scattering will occur. Elastic scattering, known as Rayleigh scatter, occurs at the same wavelength as the light source. Conversely, inelastic scattering, occurs at a wavelength that is shifted relative to the light source. Raman scatter, which is one type of inelastic scatter, is due to the excitation of vibrational modes specific to individual molecular bonds. This shift represents a molecular "signature" or "fingerprint" that can provide a breakdown of constitutive components in a material.

The theory of Raman Spectroscopy can be examined at the molecular level. An incident monochromatic light wave will cause the electron cloud to distort, as shown in Figure 2-1. The electrons will oscillate at a frequency consistent with that of the incident light. Consequently, the positively charged and significantly heavier atomic nuclei are no longer in equilibrium and vibrate at a lower characteristic frequency, v_m, representative of the atomic weight and bond stiffness. The electrons essentially

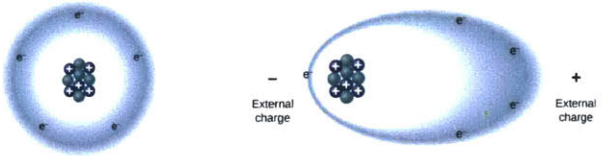

Figure 2-1: Left: Atom in equilibrium; and Right: Distorted electron cloud due to an externally applied electric field (taken from [1]).

act as dipole emitters that provide information on the vibrational characteristics of the molecule.

The magnitude of the electron cloud distortion is defined as the polarizability, given by α. The time dependent total dipole moment (μ) becomes a function of the polarizability and the applied electric field (E). In addition, there are nonlinear components that become significant at high power. In the general case, the equation for the time-dependent total dipole moment is shown in Equation 2.1 using Einstein summation notation,

$$\mu_i(t) = \mu_i^o + \alpha_{ij}E_j(t) + \beta_{ijk}E_j(t)E_k(t) + \gamma_{ijkl}E_j(t)E_k(t)E_l(t). \tag{2.1}$$

The hyperpolarizability (β) is relevant in phenomena like Resonance Raman Scattering (RRS) and the second hyperpolarizability (γ) is exploited in coherent Raman techniques, like Coherent Anti-Stokes Raman Scattering (CARS) and Stimulated Raman Scattering (SRS). If we are examining an isotropic non-polar diatomic molecule then we can assume that $\mu_i^o = 0$. In addition, if a low power laser source is used then we can assume that nonlinear terms in Equation 2.1 are negligible. Thus, Equation 2.1 can be simplified to,

$$\mu(t) = \alpha E(t). \tag{2.2}$$

The above equation assumes that the polarizability is independent of time. Yet, this can be expanded further by realizing that the value of polarizability is a function of the interatomic distance between atoms that make up the molecule, which is time-dependent and the basis for the inelastic light-matter interaction involved in Raman scattering. This can be approximated as a Taylor series expansion,

$$\alpha(t) = \alpha_o + (\frac{\partial \alpha}{\partial Q})dQ(t), \tag{2.3}$$

where the α_o term represents the polarizability of the molecule in the equilibrium state and Q is the interatomic distance. The interatomic distance will oscillate with with an amplitude Q_o and a frequency governed by the molecular vibration,

$$dQ(t) = Q_o cos(w_m t), \tag{2.4}$$

where w_m is the frequency of the molecular vibration, which is different than the frequency of the incident laser (w_i). The equation of the time-dependent applied electric field has the form:

$$E(t) = E_o cos(w_i t), \tag{2.5}$$

where E_o is the amplitude of the electric field. Substitution of Equations 2.3 through 2.5 into Equation 2.2 results in the following total time-dependent induced dipole moment equation:

$$\mu(t) = \alpha_o E_o cos(w_i t) + (\frac{\partial \alpha}{\partial Q})E_o Q_o cos(w_i t)cos(w_m t). \tag{2.6}$$

A trigonometric identity states that $cos(\alpha)cos(\beta) = \frac{cos(\alpha+\beta)+cos(\alpha-\beta)}{2}$. This can be applied to the above equation to obtain the following form of the time-dependent induced dipole moment:

$$\mu(t) = \alpha_o E_o cos(w_i t) + \frac{1}{2}(\frac{\partial \alpha}{\partial Q})E_o Q_o \Bigg[cos([w_i + w_m]t) + cos([w_i - w_m]t)\Bigg]. \tag{2.7}$$

The first term in Equation 2.7 is the Rayleigh scatter term and the second term is the Raman scatter term that occurs at a frequency shifted from that of the incident laser source. This derivation is based on a classical mechanical description of the molecular vibration. This description accurately describes the shifted wavelength location relative to the incident laser and the fact that this scattering occurs at both longer wavelengths (Stokes shift) and shorter wavelengths (anti-Stokes shift). An example spectrum is shown in Figure 2-2, where the Stokes shift and anti-Stokes shift is shown for oxygen, O_2 and nitrogen, N_2. The differences in amplitude between Stokes and anti-Stokes amplitude seen in practice are a fundamental feature not predicted by the classical model.

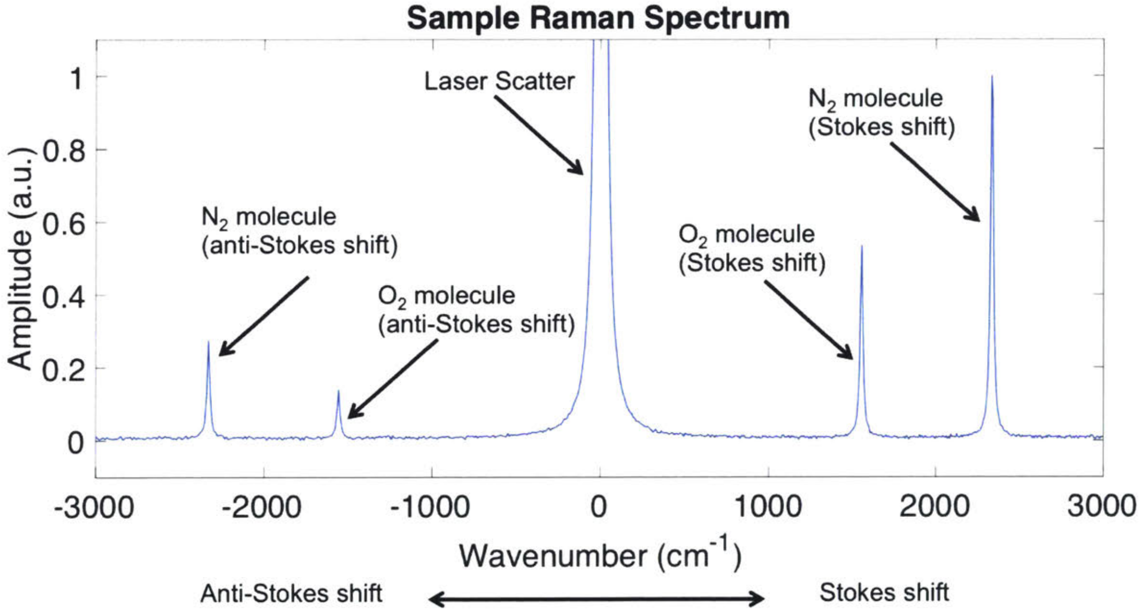

Figure 2-2: Sample Raman Spectrum of two diatomic molecules N_2 and O_2 showing Stokes and anti-Stokes shifts

As shown in the figure, Raman scatter is typically plotted in wavenumbers (i.e. cm^{-1}) relative to the input excitation. The location of the peaks can be understood by considering the diatomic molecule as a harmonic oscillator, where the relative shift is a function of the effective mass m_e and the bond strength represented by a spring of stiffness k [29]. This relationship is given by Equation 2.8. In the sample spectrum, the N_2 molecule has both a lower molecular weight and a stiffer bond (i.e. triple bond) than the O_2 molecule, which results in a significantly larger relative Raman shift, given by:

$$v_{shift} = \frac{1}{2\pi}\sqrt{\frac{k}{m_e}}. \tag{2.8}$$

Another important concept is that the intensity of the Raman scatter is proportional to the concentration of the molecules. Yet, to accurately predict these intensity values and the relative intensity between Stokes and Anti-Stokes shifts, a full Quantum Mechanical description is needed [11]. The key elements of the Quantum Mechanical model can be understood by looking at a Jablonski diagram as shown in Figure 2-3.

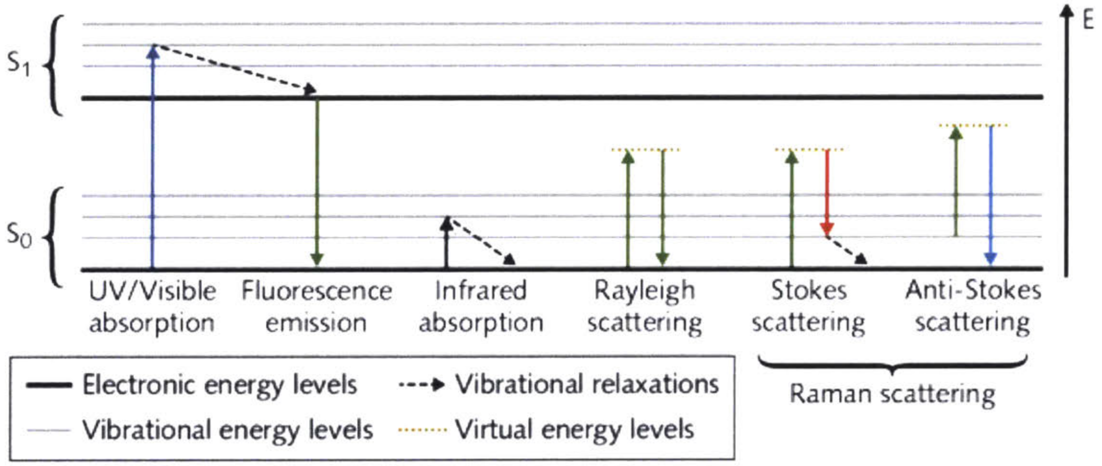

Figure 2-3: Jablonski energy level diagram for different scattering processes (taken from [2, 3]).

The electrons are excited to a *virtual* energy state, which is important for two reasons. First, the process is nearly instantaneous since there is no change in electronic state. Second, the process is nonparametric, meaning that there is an energy transfer that occurs in the interaction [30]. Therefore, depending on the initial electronic state of the molecule, there will be a difference in the number of Stokes vs. Anti-Stokes scattered photons. In thermal equilibrium, the ground state is more populated based on Boltzmann statistics, thus indicating that the intensity of the Stokes shift will be greater than Anti-Stokes shift [29]. Again, as shown in Figure 2-3 the Stokes shift corresponds to a red shift, or lower energy scattered photon, while the Anti-Stokes corresponds to a blue shift, or higher energy scattered photon. In addition, Figure

2-2 shows this difference in amplitude.

Another key element to highlight is the process of fluorescence. The Jablonski energy level diagram shows that fluorescence emission occurs from a higher electronic state to a lower electronic state. In addition, it's important to note that the fluorescence always occurs from the lowest vibrational energy level within a given electronic state, also known as "Kasha's Rule" [31]. Thus, small changes in incident laser wavelength (or energy) will have little effect on the fluorescence spectrum. Conversely, Equation 2.7 shows that small changes in incident laser wavelength cause a proportional shift in relative Raman scatter. This concept will be explored further in later chapters.

2.2 Existing Implementations

The most reliable Raman Spectrometers exist in large formats and in laboratory environments. Gas lasers, like Helium-Neon (HeNe) or Argon-ion, are typically used for their narrow atomic line output. In addition, shot-noise limited detectors are used (usually with cooling) to obtain the highest sensitivity from the detectors. These systems, although reliable, make large networks of distributed or wearable systems impractical. Therefore, there have also been a number of handheld devices developed to meet the needs that portable systems provide. Figure 2-4 shows a number of different handheld devices currently available on the market.

Figure 2-4: Existing handheld devices from Ocean Optics [4] (Left), Rigaku Analytical Devices [5] (Middle), and B&W Tek [6] (Right).

These systems are based on passive system architectures. This means that a single continuous laser source is used to excite a sample and a dispersive element spectrometer is used to record the spectrum. There is no active modulation or stray light/fluorescence suppression used, separate from the inherent device geometry (i.e. baffling and sample containment).

2.3 Current System Limitations

Although large lab-based systems have been traditionally used, several limitations have affected the implementation and widespread use of handheld Raman devices. Lopez and Ruiz mention that higher signal to noise ratios and better limits of detection are key areas for improvement [19]. Approximately 1 photon out of 10^6 to 10^7 is a Raman scattered photon [32]. This low sensitivity makes environmental light contamination, cosmic rays, and flicker or thermal noise from laser sources a large disruptive factor in spectral quality. These consequently increase the likelihood of false detection.

Another significant challenge is that the Raman signal can be saturated by fluorescence from samples. Many standard handheld systems, like the Ahura and DeltaNut Inspector Raman, sacrifice Raman intensity to operate in the near infrared spectral regime (typically around 785 nm) thereby obtaining minimal fluorescence and visible light interference [33]. Yet, Raman scattering intensity scales by λ^{-4}, which means that these longer wavelengths require detectors with much higher sensitivity [34]. In addition, reliability and repeatability between instruments has been shown to be limited [35]. Ultimately, the existing shortcomings of these handheld devices can be categorized into two main areas:

1. **Low Sensitivity:** Relative to other processes, Raman Scattering is a low intensity phenomena that can be completely saturated by other spectral features.
2. **High false detection rates:** Handheld systems suffer from spectral contamination that leads to unacceptably high false detection for many applications from fluorescence, environmental light, etc.

To overcome these challenges, there have a been a long list of supplemental Raman techniques developed with significant research specifically into methods of increasing the Raman scatter intensity. These can be categorized as coherent Raman techniques, enhancement techniques, and time gating techniques. Each of these are described in more detail below with an emphasis on the benefits, challenges, and practical limitations when implementing the technique in a handheld format for general use in the field.

Coherent Raman Techniques:

Typically use multiple high-power pulsed laser sources to generate nonlinear optical effects in a sample. When the optical beating frequency between the "pump" and "probe/Stokes" laser match the molecular vibrational frequency, there is an enhancement of up to 10^5 in the Raman scattering intensity. This enhancement occurs at a narrow bandwidth so the chemical constituent of interest must be known in advance to design an effective system, which is oftentimes impractical. Some examples of coherent techniques are Coherent Anti-Stokes Raman Scattering (CARS) and Stimulated Raman Scattering (SRS). The diagrams shown in Figure 2-5 depicts the difference between these two nonlinear techniques, where w_p is the pump frequency, w_s is the Stokes frequency, ΔI_p is the change in pump intensity, and ΔI_s is the change in Stokes intensity.

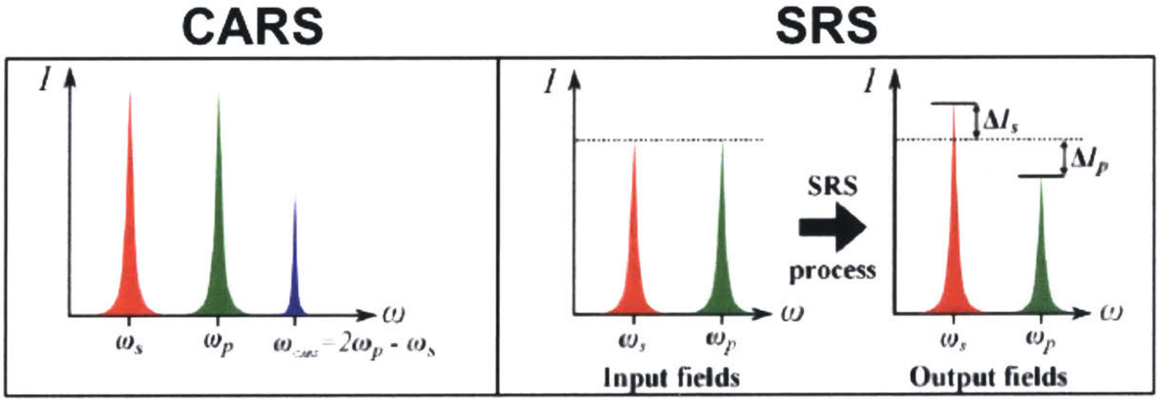

Figure 2-5: Energy diagrams showing the difference between CARS and SRS (taken from [7]).

In CARS, the enhancement is derived from constructive interference at the beat frequency as the molecules are driven into forced oscillations. This process is parametric, meaning that there is no change in the energy state of the material, but rather energy is transferred between the incident photons. In addition to the enhancements in Raman scattering at the vibrational frequency, there are also strong non-resonant background effects, which can saturate the spectrum. Conversely, SRS is based on a change in the relative intensity between the pump and probe beam as it interacts with the material, which makes it a non-parametric process, as shown by the energy diagram in Figure 2-5. Detection is accomplished by measuring the relationship between the pump and Stokes beams, so there are no contributions from other non-resonant or background effects, as in CARS. Lock-in detection techniques are typically used to amplify the changes in the signal, since they are typically very weak. Another unique difference between SRS and CARS is that they each scale differently with concentration. SRS is linear with concentration, while CARS scales nonlinearly. Depending on the application requirements, one technique may be more applicable than the other [36, 37].

There are a number of challenges associated with practically implementing coherent techniques. For example, phase matching is required between the "pump" and "probe/stokes" lasers to generate a non-zero nonlinear contribution to the scattering. From a hardware perspective, the cost and power requirements for multiple pulsed lasers in a handheld/portable format is significant. Again, the limitations in bandwidth of these techniques reduces the adaptability of this system for detection of different chemicals.

Enhancement Techniques:

Enhancement techniques aim to broadly enhance the Raman scatter and include Surface Enhanced Raman Spectroscopy (SERS) and Tip Enhanced Raman Spectroscopy (TERS), among others. It was discovered that molecules absorbed on the surface of roughened silver and gold substrates enhances the Raman scattering intensity by six or more orders of magnitude through surface plasmon and charge transfer effects associated with molecules near metallic micro- and nano-structures [34]. Surface plasmons are coupled oscillations of electrons within the metal due to the incident laser and will change depending on the size of the nanoparticles involved and the excitation wavelength. Therefore, substrates need to be tuned based on the particular wavelength excitation. Gap spaces between the metal nanoparticles produce "hotspots" or areas of high, localized electromagnetic field enhancements due to these surface plasmons as shown in Figure 2-6 [38].

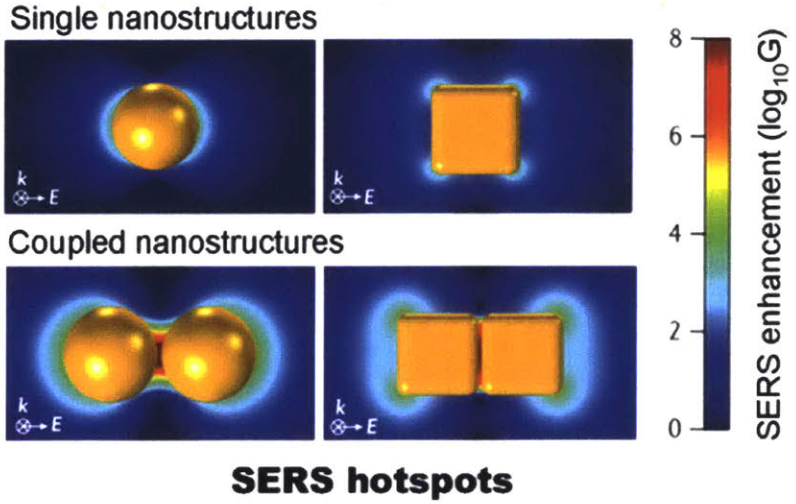

Figure 2-6: Example of SERS "hotspots" between metal nanostructures due to coupled surface plasmons induced from an incident laser on a SERS device (taken from [8]).

The main source of these localized hotspots is derived from the dielectric properties of metals that are unique compared to other material classes. In particular, the real part of the dielectric permittivity for silver and gold is negative, which becomes the critical factor for achieving a high local electric field. As an example, the electric field inside a metal sphere surrounded by a dielectric is given by the equation below (assuming that the sphere diameter is much smaller than the incident wavelength),

$$E_{loc} = \frac{3\epsilon_m(\omega)}{\epsilon(\omega) + 2\epsilon_m(\omega)} E_{in}, \tag{2.9}$$

where, $\epsilon(\omega)$ is the dielectric function of the metal, $\epsilon_m(\omega)$ is the dielectric function of the surrounding medium, and E_{loc} and E_{in} are the local and incident electric fields.

In the case where $\epsilon(\omega) \approx -2\epsilon_m(\omega)$, the local electric field is significantly enhanced [38]. Depending on the SERS geometry and interfaces, the resonant condition can be tuned. Although this is the primary source of the enhancement in the Raman signal, it's also important to note that molecules absorbed onto the metal surface will also have a modified polarizability. This results in a "chemical enhancement" from charge transfer effects associated with a redistribution of the electrons. A complete understanding of the dominant enhancement mechanism is still an area of active research and has driven the design of a variety of SERS substrates [38].

SERS has been applied for detection of a wide range of chemicals and has applicability in many fields. In addition, it has been shown that single molecules can be detected using SERS substrates. Despite the significant promise of SERS, there are still numerous challenges associated with the technique:

1. Fluorescence is also enhanced. This relationship is complex and may be more prominent in some samples than others. Yet, ultimately, the enhancements are not only isolated to the inelastic Raman scattering. Thus, separating the Raman scatter from the fluorescence spectrum can still be a challenge.

2. The surface chemistry is complex and may not be applicable to all samples without manipulation of the surface. In particular, molecules have to be within nanometers of the metal surface and some molecules have a stronger affinity than others. For instance, thiol groups, which are typically a sulfur and hydrogen atom (-SH), will "cling" well to the surface of metals. This relationship can be explained qualitatively through the "Hard Soft Acid Base" (HSAB) concept, which links the polarizability and charge states of the molecule to its affinity for other molecules [39].

3. Photo-bleaching can occur and result in an evolving spectrum. This is true for both SERS and spontaneous Raman conditions, but the enhancements in SERS can change the photo-bleaching properties of the particular molecule. This is particularly relevant for dyes.

4. A strong background signal from the "matrix" or "continuum" is apparent. The origin of this background is still unclear, but has been documented and is being studied [40].

5. Signal fluctuations, both in point measurements and across a scanned surface lead to low repeatability and non-uniform enhancements. This limits the quantitative ability of the technique to compare concentrations between samples.

Ultimately, research into SERS has focused on the development of more robust SERS substrates to address these issues. This includes the use of novel materials like graphene for fluorescence suppression and different geometries for a more uniform, repeatable enhancement [41]. As an example, three different substrates are shown in Figure 2-7 from three different SERS manufacturers.

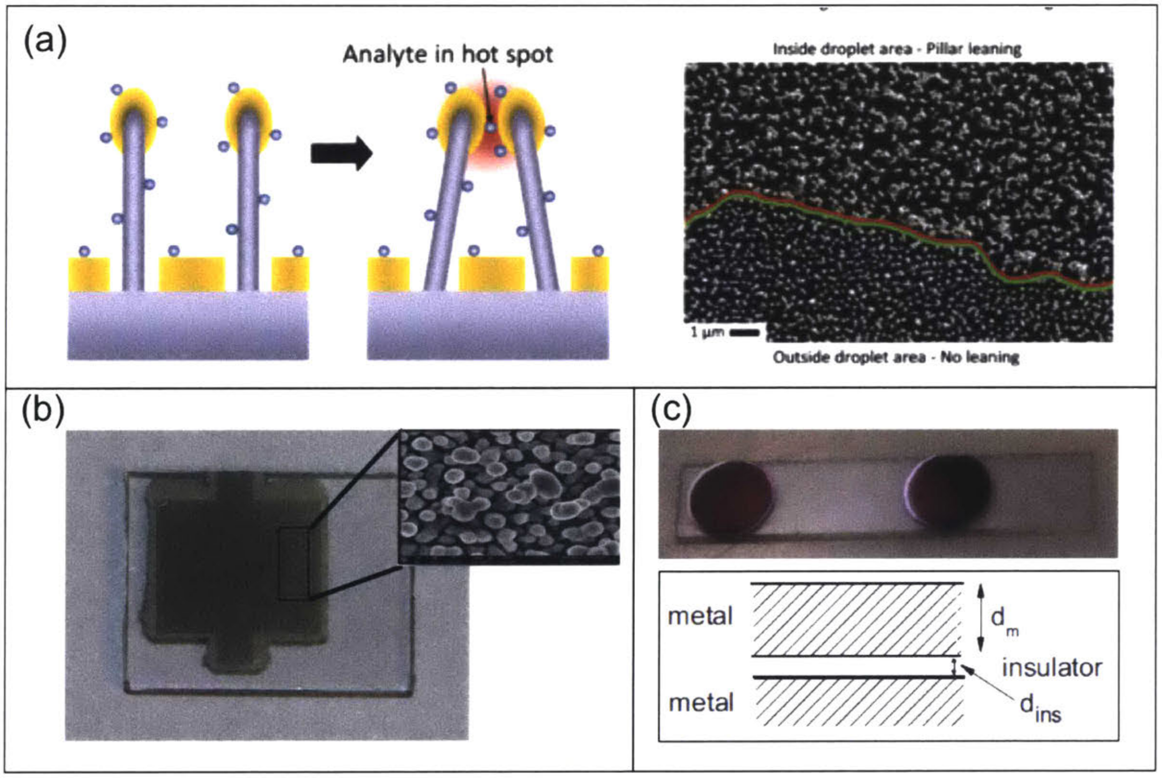

Figure 2-7: Basic mechanics of three different SERS substrates from: (a) Silmeco (taken from [9]), (b) SERSitive (taken from [10]), and (c) Enspectr (taken from [11]).

A company called Silmeco uses pillar-like features. When the surface is saturated with a liquid sample, capillary action draws the pillars together to create local "hotspots" when the fluid dries. This concept is shown in Figure 2-7(a) from a paper published by Schmidt et. al., where these pillars can be visualized [9]. Yet, this design also makes the substrates highly sensitive to thermal effects and laser power is limited. Another company called SERSitive makes substrates that are prepared on glass slides as to eliminate background features associated with silicon. Gold and silver nanoparticles of varying dimensions are deposited using an electrodeposition process to create the roughened metal that acts to enhance the Raman scattering. These substrates are shown in Figure 2-7 (b). A third company called Enspectr is exploring the use of dielectric intermediate layers between the substrates to create a more uniform enhancement area. These substrates and their primary design mechanics are shown in Figure 2-7(c). A number of other companies exist that manufacture SERS devices, but the companies selected provide a representative sample of the different manufacturing techniques.

Time-Gating Techniques:

Notably, it has been mentioned that Raman scattering is a nearly instantaneous process [42]. This characteristic of Raman scattering can be utilized by collecting data before longer lifetime processes occur. For example, fluorescence lifetimes are on the order of nanoseconds and can be even longer depending on the sample. The general requirements of this type of system are similar to the coherent techniques described previously, with the added complication of synchronizing a high-speed imaging/detection system. Gating times are typically on the order of picoseconds and Kerr cells, which become birefringent when an electric field is applied, are used as high-speed shutters [42, 43]. The main benefit of time gating is that there is a significant increase in the signal-to-noise ratio due to the reduction in background and fluorescence artifacts in the spectrum. Yet, the complexity of the system and power requirements make it difficult to implement in a portable format.

Although each of these advanced Raman techniques attempts to solve the sensitivity and high false detection rate problems, they are either not scalable to a handheld device, still unreliable, or result in new challenges. The goal of this research is to implement a novel system architecture that moves from the standard passive handheld Raman systems to an active system architecture. To understand how an active system architecture would work, it's important to recognize the unique properties of the Raman scattering signature compared to other artifacts in the spectrum. This is discussed in the next chapter.

Chapter 3

Conceptual System Design

The proceeding sections will discuss the basis of the active system architecture, the novel aspects of the design, component selection, and the system development.

3.1 System Architecture

Handheld systems are reliant on a passive architecture. A passive system will irradiate a sample, capture the incident light, then pass it through a Fourier Transform (FT) or dispersive-element spectrometer for analysis. Data processing may be done to remove low frequency components in the form of broadband fluorescence, while maintaining the high frequency components indicative of the sharp peaks associated with the molecular vibrations. As mentioned, one of the unique characteristics of Raman scattering is that it is always relative to the incident laser wavelength. For small changes in wavelength, if the system is not excited to a new electronic state then the fluorescence spectrum remains relatively unchanged. This has been demonstrated with the use of tunable laser sources and laser diodes in a technique called "Shifted Excitation Raman Difference Spectroscopy," or SERDS. Two different spectrum are collected at two excitation wavelengths, and then one is subtracted from the other. SERDS has been implemented in a large system format using tunable lasers and, more recently, in a portable format. An example of each of these systems is shown in Figure 3-1.

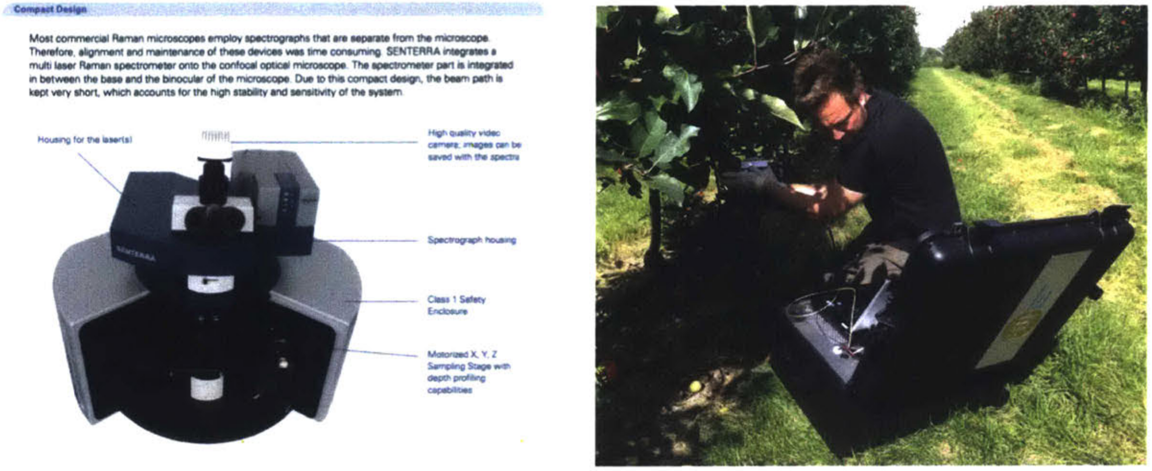

Compact Design

Most commercial Raman microscopes employ spectrographs that are separate from the microscope. Therefore, alignment and maintenance of these devices was time consuming. SENTERRA integrates a multi laser Raman spectrometer onto the confocal optical microscope. The spectrometer part is integrated in between the base and the binocular of the microscope. Due to this compact design, the beam path is kept very short, which accounts for the high stability and sensitivity of the system.

Figure 3-1: Existing available implementation of SERDS systems: (Left) large format Brüker-Optic (taken from [12]) and (Right) portable system (taken from [13]).

The SERDS technique directly addresses one of the existing limitations of the handheld devices - the high false detection rate. The subtracted spectrums from two measurements isolate the Raman scattering relative to other spectral features in the data. However, the main challenge is implementing this in a handheld format. The use of laser diodes is not ideal because they are temperature sensitive and must be isolated from environmental temperature swings or have an embedded temperature control system. More importantly, laser diodes operate through amplification in a gain medium. This amplification process gives rise to specific excitation modes or wavelengths that have an effective full width half maximum (FWHM) that is significantly broadened. Each of these modes contributes to the Raman scattering at the respective wavelength shift. Consequently, the Raman peaks broaden and their spectral profile changes as the different modes have different intensities. In addition, the strength of each mode may not be linear with temperature, which can further affect the relative shape of the spectrum. The quality of the Raman spectrum is critical as it is referenced against existing curves and peaks to identify chemical constituents. Another impact of using temperature to modulate the excitation wavelength is the time required for the laser to stabilize, which can range from seconds to minutes, depending on the diode and the external environment. Thus, minimizing the stabilization time is necessary to reduce the overall duration of the measurement.

Traditional approaches to the development of a handheld Raman Spectrometer have to be reconsidered when focusing on shifted excitation. A number of new lasers have been developed in a compact format that provide narrow linewidths at a single frequency. Some examples include Distributed Bragg Reflectors (DBR), Distributed Feedback (DFB) Lasers, and Vertical Cavity Surface Emitting Lasers (VCSELs). The narrow linewidth is ideal for Raman Spectroscopy and many of these devices operate in the visible to NIR/IR wavelength range, yet the modulation bandwidth is limited. These devices cannot be adjusted by more than a few picometers in operational wavelength and are prone to mode hopping as they are adjusted, which can vary from device to device.

A novel system architecture is required that enables rapid modulation between two input wavelengths with a narrow laser linewidth that is both low cost and compact to fit into a handheld design. The design for such a system was inspired by applications in structural health monitoring, where strain and temperature variations induce changes in optical properties of a Fiber Bragg Grating (FBG). Optical interrogators, which are narrow bandwidth, high resolution spectrometers, are used to monitor the optical changes in the FBG. FBGs have been commonly used for strain sensing in a variety of structures that require immunity to electromagnetic interference and in geotechnical health monitoring due their long-term stability. They have also served as relative humidity sensors by coating the FBG with a hydrogel that swells depending on the humidity [44, 45, 46]. In addition, their ability to be multiplexed makes them ideal for multi-point detection.

The characteristics of FBGs make them well suited for applications in shifted excitation Raman Spectroscopy because of both the mechanics of how they operate and the added available functionality. They act as both a filter and an isolator by reflecting only a narrow portion of a beam that is transferred through the fiber. This portion of the beam can be modulated externally through an applied strain or temperature. As a result, a narrow "artificial" laser can be produced and modulated using an FBG for Raman Spectroscopy applications. Their small geometry, relatively

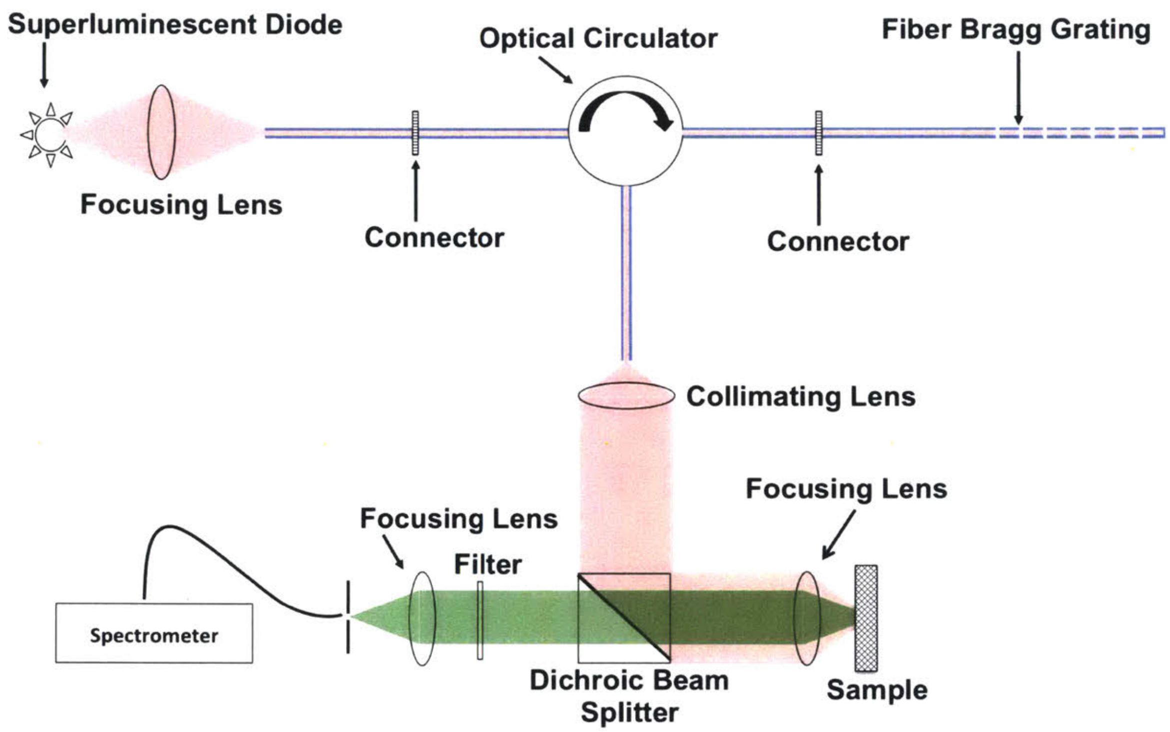

Figure 3-2: Schematic showing the novel conceptual design of the modulated Raman Spectrometer system architecture.

low cost, and long term stability make them applicable for use in a small format. In addition, they allow for decoupling of the light source from the modulation source. Therefore, the spectral power can be controlled independently (i.e decoupled) from the modulation source. This reduces effects like mode hopping that are seen in standard temperature controlled laser diode systems. A schematic of the proposed handheld modulated Raman Spectrometer is shown in Figure 3-2, which highlights the key elements.

A superluminescent diode (SLED) is coupled into a single-mode fiber. The single-mode fiber acts as a spatial filter to produce a Gaussian beam profile with the high frequency components removed. The beam is then coupled into a three way optical circulator. The first output of the optical circulator sends the beam to a custom FBG. The FBG reflects only a narrow spectral portion of the beam back to the circulator. The reflected spectrum can be tuned based on how much strain is applied to the FBG through a mounted piezo-actuator. The mechanics of how this back reflection works will be discussed in Section 3.1.2. All other components of the spectrum continue to pass through the FBG and exit the optical setup. The FBG thus acts as an optical filter. The narrow spectrum back-reflected then re-enters the optical circulator, which is a nonreciprocal device. A combination of a high Verdet constant and birefringent crystal are used to rotate and redirect the beam to the third output of the optical circulator [47]. The beam exits the fiber and is collimated, reflected off a dichroic beam splitter, and focused onto a sample. Scattered light is collected from the sample through the same focusing lens in a backscatter configuration and is propagated back to the dichroic beam splitter. The dichroic has different transmission and reflection characteristics at different wavelengths; thus, any Raman shifted light is transmitted through the dichroic. A second filter acts to further remove any Rayleigh scatter from the laser line. The remaining light then passes through a narrow slit and into a spectrometer. In this configuration, only Stokes shifted (lower frequency shift) Raman signals are isolated, since the amplitude of the Stokes shift is significantly higher than the anti-Stokes amplitudes. The cost in terms of price and reduced resolution outweigh the added benefits of simultaneously measuring the anti-Stokes signal. The two novel elements of this design are the SLED and the FBG for use in a Raman Spectrometer. Each of these elements are described in more detail below, including their basic operation and functionality.

3.1.1 Superluminescent Diode

SLEDs are devices that output a relatively broad spectrum as compared to traditional lasers. These devices can have a 3 dB FWHM ranging from 4 nm to 100 nm and are most commonly found in the center wavelengths at 750 nm up to 1600 nm. Recently, a company called Exalos has been developing these devices in the visible range with the objective of integrating them in projection display systems. Although they have low temporal coherence, they have high spatial coherence. The benefit of the high spatial coherence in Raman Spectroscopy is that the output from these devices is able to be focused to a small spot size and, therefore, maximize the local intensity to produce the corresponding highest intensity Raman scattering. In addition, the high spatial coherence allows them to be efficiently coupled into single-mode fibers for a more compact design. The combination of these devices with FBGs enable a narrow selection of the beam profile that can be modulated.

The basic mechanics of these devices rely on Amplified Spontaneous Emissions (ASE). In this system, there is no direct feedback mechanism, so sharp peaks associated with laser modes are not produced. Rather, a relative broad spectrum at lower power is obtained. A comparison of SLEDs to a standard laser diode is shown in Figure 3-3. Standard laser diodes have a narrow spectrum with discrete, high-intensity modes, while light-emitting diodes have lower energy and a wider spectrum.

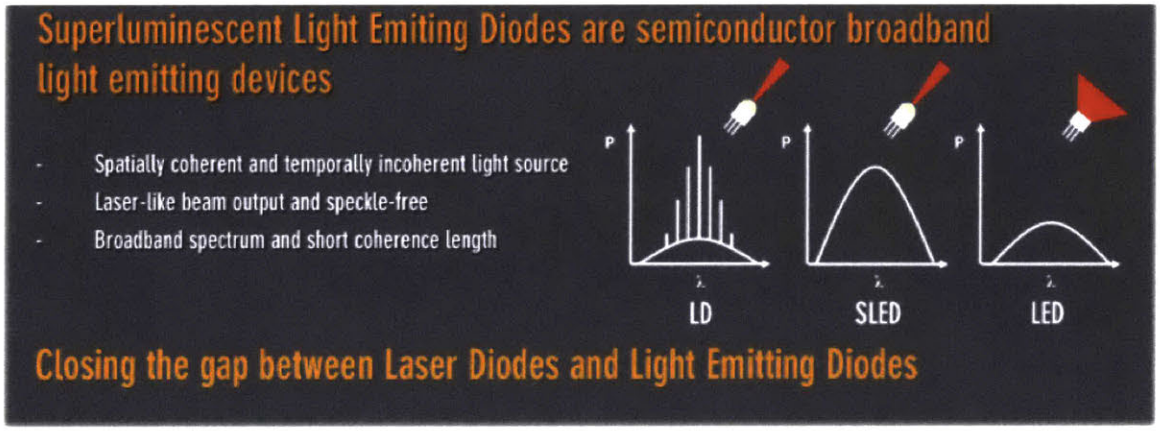

Superluminescent Light Emiting Diodes are semiconductor broadband light emitting devices

- Spatially coherent and temporally incoherent light source
- Laser-like beam output and speckle-free
- Broadband spectrum and short coherence length

Closing the gap between Laser Diodes and Light Emitting Diodes

Figure 3-3: Comparison of different diodes (taken from [14]).

3.1.2 Fiber Bragg Grating

FBGs are specialized optical fibers that reflect a narrow portion of a spectrum, while allowing the remainder of the spectrum to continue propagating, therefore acting as a type of optical filter. As the fibers are strained or expanded due to temperature, the portion of the spectrum that is reflected changes proportionally. FBGs are made from germanium-doped silica single-mode fibers that exhibit periodic refractive index variations along a portion of the fiber. To form such FBGs, an interferometric pattern is projected onto the fiber using UV light, which causes index of refraction changes in the silica. The UV light intensity, spacing, and exposure duration are controlled and actively measured to produce a high quality grating that reflects only a narrow portion of the incident spectrum ranging from several picometers to hundreds of picometers.

Companies that manufacture these FBGs focus on the development in the near-infrared to infrared region of the spectrum from 780 nm to approximately 1600 nm. The main reasons for this are their use in optical communication networks and absorption based chemical sensing applications. In addition, there are fundamental difficulties in manufacturing FBGs in the visible wavelength range, which requires a shorter grating period. High resolution detectors are required to monitor the index change, but since UV light is used, the quantum efficiencies of the detectors at these wavelengths are low and the minimum grating period and process controllability is limited. Most of the FBG manufacturers specify the center wavelength, the expected reflectivity (based on the grating length), the FWHM of the reflected profile, and the side lobe suppression ratio (SLSR). There is an inverse relationship between the FWHM and the SLSR, so a compromise has to be made based on the application requirements. This becomes more predominant at shorter center wavelengths where apodization of the index change is more difficult.

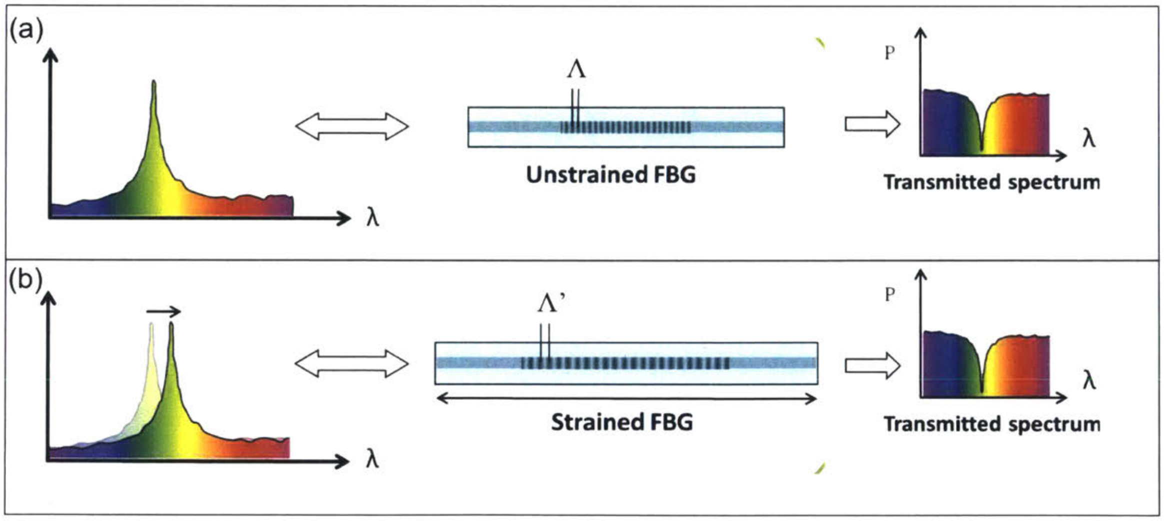

Figure 3-4: FBG principle of operation showing: (a) the narrow reflected spectrum spectrum and the corresponding transmitted spectrum; (b) the change in position of the reflected spectrum as the fiber is strained (Modified from [15]).

Figure 3-4 shows the basic mechanics of the FBG and how the reflected spectrum changes from the unstrained to strained positions. This phenomenon can be explained as a period change in the index of refraction of the fiber core given by,

$$\lambda_{Bragg} = 2n_{eff}\Lambda, \tag{3.1}$$

where n_{eff} is the effective refractive index of the core and cladding of the fiber and Λ is the period of the grating [48, 49]. These variables are affected by both strain and temperature and the coupling between these effects can be challenging to separate. By taking the partial derivative of the Bragg wavelength with respect to strain and temperature, the theoretical sensitivity to each of these can be estimated. M. M. Werneck et al., derived the equation that describes the theoretical sensitivities in Reference [48]:

$$\Delta\lambda_{Bragg} = [(1 - \rho_e)\epsilon + (\alpha + \eta)\Delta T]\lambda_{Bragg}, \tag{3.2}$$

where ρ_e is the coefficient representing the index of refraction sensitivity to strain (i.e. photo-elastic coefficient), ϵ is strain, α is the coefficient of thermal expansion (CTE) of silica fiber, η is the index of refraction sensitivity to temperature (i.e. thermo-optic coefficient), and ΔT is the change in temperature. Estimates for the strain sensitivity and temperature sensitivity are typically on the order of several picometers/$\mu\epsilon$ and picometers/°C, respectively. The exact values depend on the center wavelength, the duration of UV irradiance on the germanium doped fiber, and other fiber characteristics. To minimize the thermal effects in the current design, the FBG is bonded to the piezo-actuator with an epoxy that has a low coefficient of thermal expansion (CTE) and low thermal conductivity. In addition, the piezo actuation time and measurement time are short duration, therefore limiting heat generation from the unit.

3.2 System Requirements

Transitioning from the design phase to a physical system requires matching component specifications and also finding the combination of components and excitation wavelength that produce the highest relative signal-to-noise ratio (SNR). The SNR can be defined as the Raman signal divided by the standard deviation of the photon count [50]. The photon count can be decomposed into contributions from several system elements as,

$$SNR = \frac{S_R}{\sqrt{\sigma_s^2 + \sigma_b^2 + \sigma_d^2 + \sigma_f^2 + \sigma_r^2}}, \tag{3.3}$$

where S_R is the Raman signal, σ_s is the standard deviation of the signal, σ_b is the background noise that includes the fluorescence, σ_d is the dark noise, σ_f is the flicker noise, and σ_r is the readout noise. This equation can be simplified by making a number of assumptions:

1. The laser power is stabilized such that flicker noise is negligible ($\sigma_f \approx 0$). In addition, it is assumed that a dispersive multi-element spectrometer is used so that relative flicker noise between pixels is eliminated.

2. The detector is cooled such that the photon count is significantly above the dark current (ϕ_d) for a given integration time (t_{int}). Thus, we can assume that $\sigma_d = \sqrt{\phi_d t_{int}} \approx 0$.

3. Readout noise is negligible compared to the signal and background (i.e. fluorescence) noise, such that $\sigma_r \approx 0$.

4. The resolution remains unchanged through the spectrum. This is an important assumption since the shorter wavelength (higher energy) photons will produce more intense Raman scattering, but over a smaller pixel region to maintain the given spectral resolution.

5. The system is shot noise limited, therefore, the standard deviation of each noise source is equal to the square root of the signal itself (i.e. $\sigma_s = \sqrt{S_R}$ and $\sigma_b = \sqrt{S_B}$).

The consequence of the above assumptions is that we can now simplify Equation 3.3 into,

$$SNR = \frac{S_R}{\sqrt{S_R + S_B}}, \tag{3.4}$$

where S_R represents the Raman scattering signal and, now, S_B represents the non-Raman background signal contributions from the sample. The proposed schematic of the system in Figure 3-2 can now be updated to include a number of geometric parameters that represent component coupling efficiencies, detector quantum efficiencies, and laser intensity. An updated schematic is shown in Figure 3-5. Each of these elements contribute to the total Raman signal and background signal.

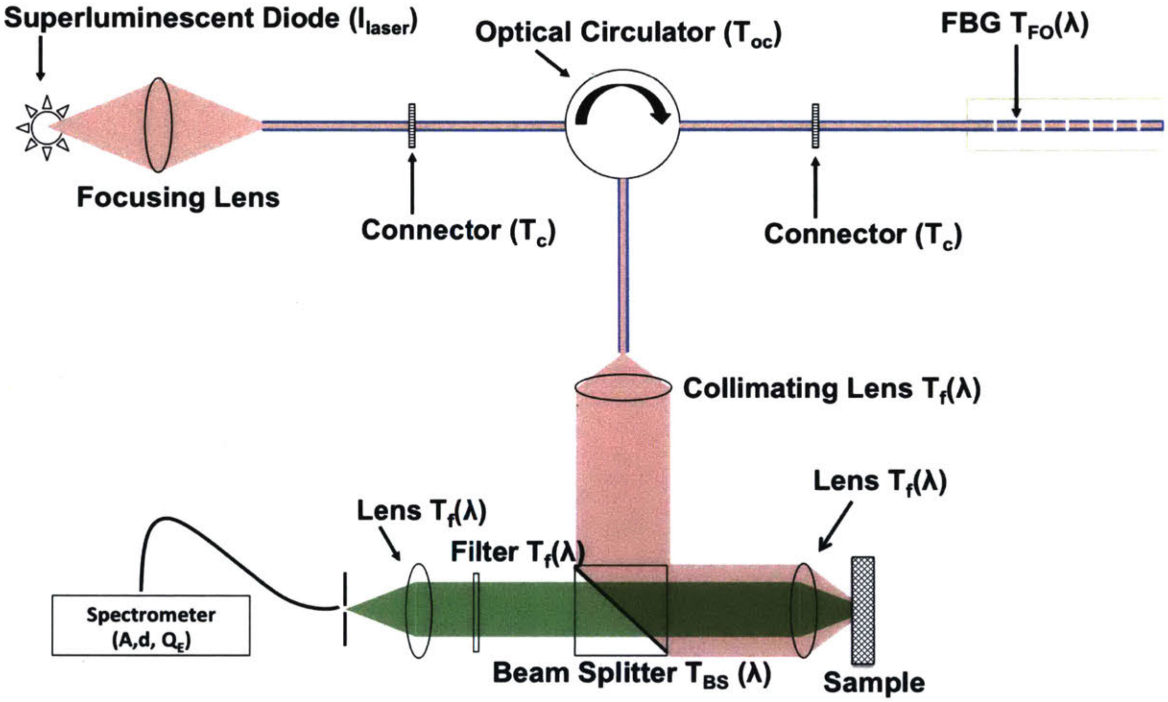

Figure 3-5: Modified optical schematic with assigned transmission efficiencies to each component.

An extensive list of suppliers of these optical elements was explored and the most common values for the transmission at different wavelengths was recorded. It is important to note that suppliers provide discrete dichroic beam splitter cutoff wavelengths and filter options, so not all wavelength options are available for use. Similarly, available lasers generally fall into discrete wavelengths. The total Raman signal measured in photons is given by [50],

$$S_R(\lambda) = \beta_R(\lambda) V I_{Laser} d A_D \Omega T_E(\lambda) Q_E(\lambda) t_{int}, \tag{3.5}$$

where β_R is the cross section, or likelihood of interaction between the photon and sample, as a function of the excitation wavelength (λ) and measured in $\frac{m^2}{molecule\text{-}steridan}$. This term is responsible for the λ^{-4} relationship in Raman scattering intensity commonly observed [50]. V is the density of scatterers in the sample, measured in $\frac{molecules}{m^3}$. There are also a number of geometric and performance-based terms. I_{Laser} is the photon density from the laser in $\frac{photons}{m^2 \cdot s}$. d is the sample depth that is observed by the spectrometer in m; this can change based on the type of confocal system used and the entrance aperture into the spectrometer. Along the same lines, the A_d term is the relative area observed by the spectrometer. Ω is the collection angle in *steridans*, which is proportional to the numerical aperture of the lens. A higher numerical aperture translates directly to a higher collection angle. The transmission efficiencies of each optical component are coupled into a T_E term and are wavelength-dependent. The same is true for the quantum efficiency of the detector (Q_E), which is assumed to be a back thinned CCD. The final term in the equation is the integration time t_{int}, which is measured in *seconds*. The total background signal also follows a similar equation [50]:

$$S_B(\lambda) = \beta_B(\lambda) V I_{Laser} d A_D \Omega T_E(\lambda) Q_E(\lambda) t_{int}. \tag{3.6}$$

The primary difference in the background signal equation is the cross section. Typical cross sections for fluorescence are much greater than those for Raman scatter. The substitution of Equation 3.5 and 3.6 into Equation 3.4 yields for the SNR:

$$SNR(\lambda) = \frac{\beta_R(\lambda)\sqrt{V I_{Laser} d A_D \Omega T_E(\lambda) Q_E(\lambda) t_{int}}}{.} \sqrt{\beta_B(\lambda)} \tag{3.7}$$

It is important to note that the ratio $\frac{\beta_R}{\beta_B}$ varies with excitation wavelength. Specifically, this ratio increases when moving from the visible excitation wavelength range to the NIR excitation range. This is the concept behind using longer wavelengths in

Raman spectrometers, which is typically done in commercial systems. Yet, the other factors outlined in these equations must be considered when identifying the optimal SNR, specifically the quantum efficiencies and transmission efficiencies at different wavelengths. Moreover, this ratio will also change depending on the chemical constituent of interest. Values for terms were estimated and modeled under different cross-section ratios using MatLab [51]. The results are shown in Figure 3-6, where the SNR is define or normalized "relative" to the lowest value.

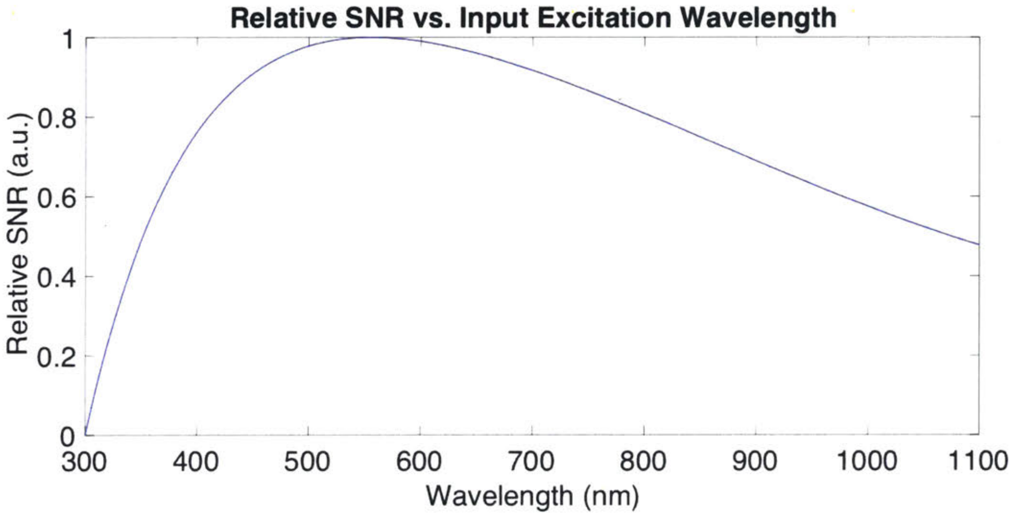

Figure 3-6: SNR curve showing the optimal excitation wavelength range based on Equation 3.7.

The analysis was done using standard spectral curves for the quantum efficiencies of back-thinned CCDs, which can be as high as 90% for some detectors in the visible range and varies depending on wavelength. In addition, it was assumed that the laser intensity remained constant over all wavelengths and that the scattering characteristics, including volume, collection area, and integration time also remained constant. Consequently, these values have no effect on the spectral curve as they are approximated as wavelength-independent. Another important note is that it was assumed that the pixel size varied to maintain the same spectral resolution. This effects the number of photons collected in a given integration time. Research was also done on transmission curves for standard lenses and optical components, which was roughly constant around 90%. As shown by Figure 3-6, the optimal excitation is between

530 nm and 580 nm. Notably, this may vary depending on component availability.

Based on the analysis described above, the requirements for this system were generated and are outlined in Table 3.1. The laser excitation window is given by the analysis provided above for the optimal SNR. The spectral resolution requirement was estimated by analyzing the existing resolution of devices on the market and recognizing that there is a balance between photon count and pixel size. As the pixel size gets smaller, the number of photons hitting the detector will decrease and the integration time will have to increase. The spectral resolution of the NanoRam device is 9 cm^{-1} at 912 nm excitation wavelength, whereas the CBEx device is 12 to 14 cm^{-1} at 785 nm excitation wavelength. The IDRaman device is 16 cm^{-1} at 638 nm excitation wavelength, which is closest to the optimal SNR estimated earlier.

Table 3.1: System Requirements

Parameter	Requirement	Justification
Excitation	530 to 580 nm	Based on the maximum SNR analysis
Spectral Resolution	<12 cm^{-1}	Balance between photon count and pixel size
Laser linewidth	<80 pm	Spectral resolution used to estimate the line width
Minimum spectral shift	>0.250 nm	Estimate of the detector resolution
Spectral Stability	<8 pm	Estimate from pixel size and laser linewidth
Power Stability	<1%	Typical laser intensity stability
SMSR/SLSR	>10 dB	Typical laser SMSR/SLSR values
Input Power	>1 mW	Based on wavelength excitation

In the ideal case, the laser linewidth is a sharp, narrow atomic line similar to the one seen from a Helium Neon laser. Yet, given the spectral resolution, this requirement can be relaxed to be about 80 picometers FWHM, which is less than half the pixel size of the detector. Similarly, the measurable spectral shift must be at least one pixel wide. Therefore, the FBG should be strained to produce a shift of at least 0.250 nm. The minimum shift value is critical because it relates to how much energy is required to strain the fiber. Depending on the FBG strain sensitivity characteristics and the piezo max displacement, this could result in significantly different energy demands. Finally, laser characteristics, including the power, stability, and side mode/lobe suppression ratio (SMSR/SLSR), are estimated based on the performance of standard laser diodes used in Raman spectrometers. Power and size requirements of the device are not highlighted here, but fall within similar metrics as handheld devices mentioned above.

3.2.1 Component Selection

The optimal excitation wavelength was outlined in the previous section. Yet, as mentioned earlier, there may be limitations in the vendors' ability to meet the component level requirements. Specifically, the FBG and SLED devices are typically designed for use in the NIR portion of the spectrum. Therefore, finding compatible components ultimately drove the excitation wavelength. Table 3.2 breaks down the final selection of key components and highlights their specifications.

Table 3.2: Component Selection

Component	Company	Specifications
FBG	Novae-Laser [52]	633 nm center wavelength, FWHM$<$25 pm, SLSR$>$10 db
Optical Circulator	Ascentta [53]	633 nm center wavelength, Insertion loss$<$2.3 db
SLED	Exalos [54]	635 nm center wavelength, FWHM$<$6 nm, TO-56 can, 12 mW minimum power
Objective lens	Mitutoyo [55]	$>$0.7 N.A., $<2\,\mu m$ diffraction limited spot size
Filter	Thorlabs [56]	$<10^{-4}\%$ transmission at Laser wavelength, $>$90% Transmission above 500 cm^{-1} shifts
Connector	Thorlabs	Insertion loss $<$0.5 db
Linear Piezo	PI [57]	$18\,\mu m$ max displacement
Spectrometer	Ocean Optics	$<$ 10 cm^{-1} resolution

The motivation for selecting 633 nm was twofold. First, it overlaps with the HeNe laser wavelength, the importance of which will be discussed in the next section. Second, it most closely overlaps the optimal excitation wavelength range. It is important to note that the SLED does not directly overlap with this wavelength range. Yet, the FWHM is wide enough to cover the excitation wavelength. Another important note is related to the piezo-actuator, where the max displacement is based on theoretical calculations of the FBG strain sensitivity. This sensitivity needs to be evaluated for the FBG and the dimensions of the piezo-actuator must accommodate the FBG length. The implementation approach to testing the novel elements in this design are detailed in the following section.

THIS PAGE INTENTIONALLY LEFT BLANK

Chapter 4

System Development

The theory and analysis outlined in the previous chapters will now be used to systematically develop a testbed that verifies the functionality of the novel elements in the system.

4.1 Implementation Approach

To test the new system architecture, the approach was to build a testbed to characterize and prove out each of these elements independently. The testbed consists of the classical elements used in a Raman Spectrometer at the optimal wavelength that was outlined in the previous chapter. Once a custom working system was built, each element could be systematically replaced to prove out the functionality. A breakdown of items that needed to be proven through this testbed are described below:

- **Proof of concept 1:** Show that a Raman spectrum can be obtained from the back reflection of an FBG beam. If the reflected spectrum is unstable or too broad, then the Raman scattering intensity could be too low to measure.

- **Proof of concept 2:** Verify that a strain in the FBG causes a relative shift in the Raman scatter. Confirming that shift is measurable is a key element of the testbed.

- **Proof of concept 3:** Confirm that "Kasha's rule" is valid at shorter wavelengths. Higher energy photons mean that the maximum wavelength shift before the fluorescence spectrum changes becomes smaller. Given the pixel size and resolution of the detector, the minimum noticeable shift is on the order of 0.25 nm.

- **Proof of concept 4:** Show that a SLED device can be used together with an FBG to isolate a narrow portion of the beam, which is then utilized to obtain Raman scattering. The broad spectrum of the SLED is inherently not ideal for Raman scattering; confirmation is needed that its combination with an FBG produces a narrow, stable beam.

4.2 Testbed: Customizable Type II Confocal Raman Spectrometer

A schematic of the testbed system is shown in Figure 4-1 along with a CAD model that includes the opto-mechanical elements needed for alignment. In this system, a 2 mW helium neon (HeNe) laser source was aligned through a pinhole spatial filter and focused onto a sample using a dichroic beam splitter. Infinity-corrected optics with high numerical apertures allowed for minimization of the spot size to maximize local laser intensity. Both Rayleigh and Raman scattered light were then collected in a backscatter configuration through the same optical component. Raman shifted light was transmitted through the dichroic acting as a long pass filter and was focused into the core of a fiber optic cable. An Ocean Optics QEPro spectrometer was used to analyze the return spectrum.

Each optical element was selected in order to maximize the intensity at the sample, since the Raman scattering intensity scales with the square of the electric field. The first step in this process is to produce an optimal Gaussian beam. Higher spatial frequencies that distort the beam intensity profile become apparent as diffraction rings on the focused beam profile. A spatial filter will only pass the center TEM00 mode of the beam and remove these high spatial frequencies. In theory, the diffraction

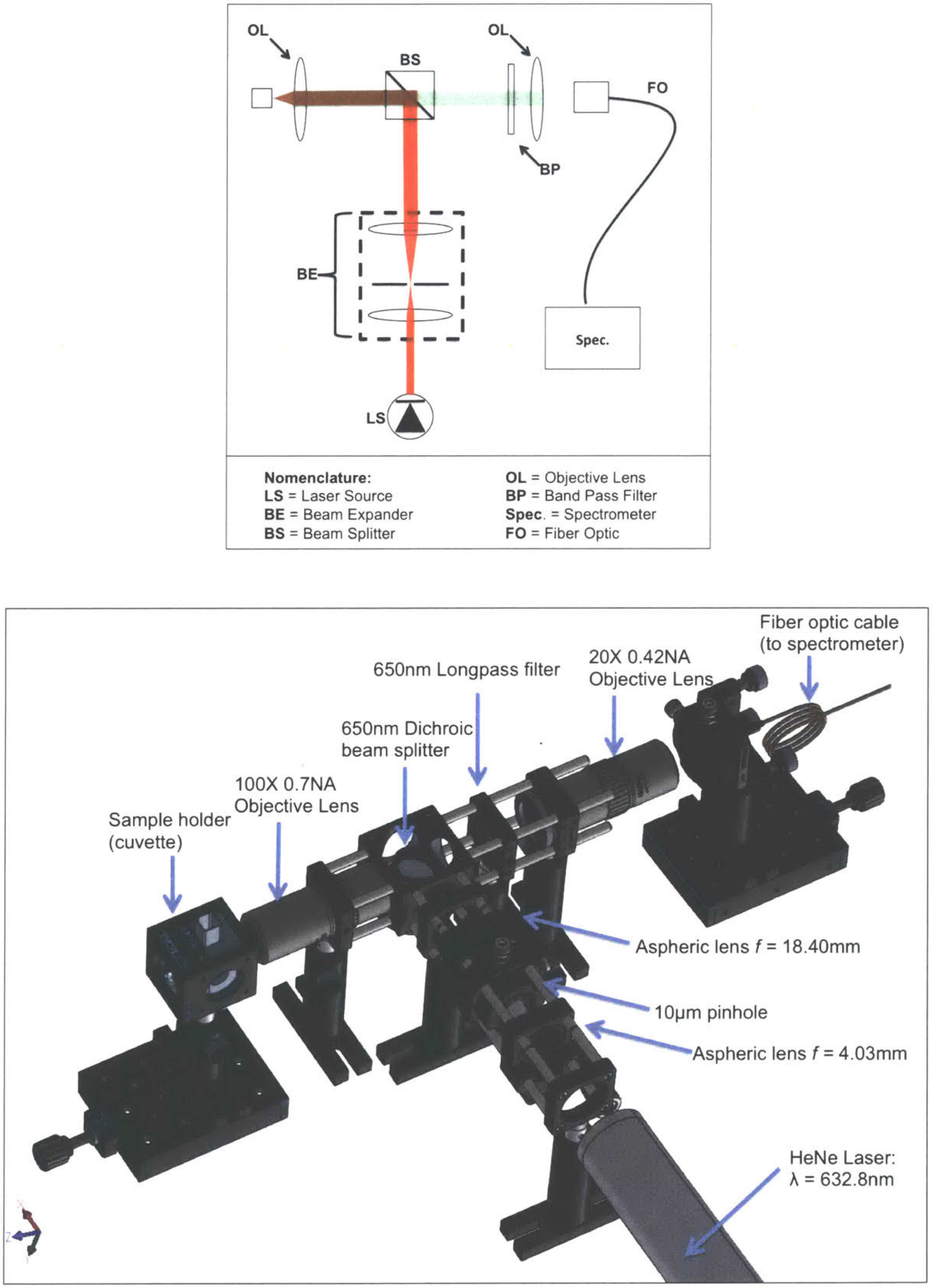

Figure 4-1: Custom Raman optical system showing (top) schematic of components; and (bottom) CAD model with opto-mechanical elements included for alignment.

limited spot size of the beam is given by:

$$d_{spot} = \frac{4\lambda f}{\pi D}. \tag{4.1}$$

It is generally recommended to size the pinhole to be 1.5 times the diffraction limited beam spot size as an optimal balance between maximizing throughput power and removing higher frequency spatial components [58]. This corresponds to approximately a 10 micrometer pinhole in the current system. The beam was then recollimated using a lens with an appropriate focal length such that the collimated beam diameter matched the entrance aperture of the objective lens at the sample. Aspheric lenses with anti-reflection coatings were used in the focusing and recollimating of the beam, as they maintain the beam quality of the wavefront without introducing aberrations.

The next element in the testbed was a dichroic beamsplitter that provided greater than 95% reflectivity at the HeNe excitation wavelength of 633 nm to direct the recollimated beam into the high numerical aperture Mitutoyo objective lens. Given the lens and beam parameters, the focused spot at the sample was approximately $2\,\mu m$ in diameter with an energy density of 6.4x10^{8} W/m^{2}. Raman scattering signal was recollected from the same lens and was transmitted through the dichroic beamsplitter. A frequency cutoff was then provided by a longpass filter that has a sharp cutoff at 650 nm. Another Mitutoyo objective lens then focused the beam into a $50\,\mu m$ core multi-mode optical fiber, which is connected to an Ocean Optics QE Pro spectrometer. The fiber essentially acts as a spatial filter that only allows scattered light corresponding to a narrow depth of focus to be coupled. Additional details on the spectrometer will be discussed in Chapter 5. This system is called a type II confocal system and a realization of the system is shown in Figure 4-2.

4.2.1 Component Level Characterization

Prior to alignment of the system, two key elements were characterized to understand the performance. The first element was the HeNe laser. These lasers generate sig-

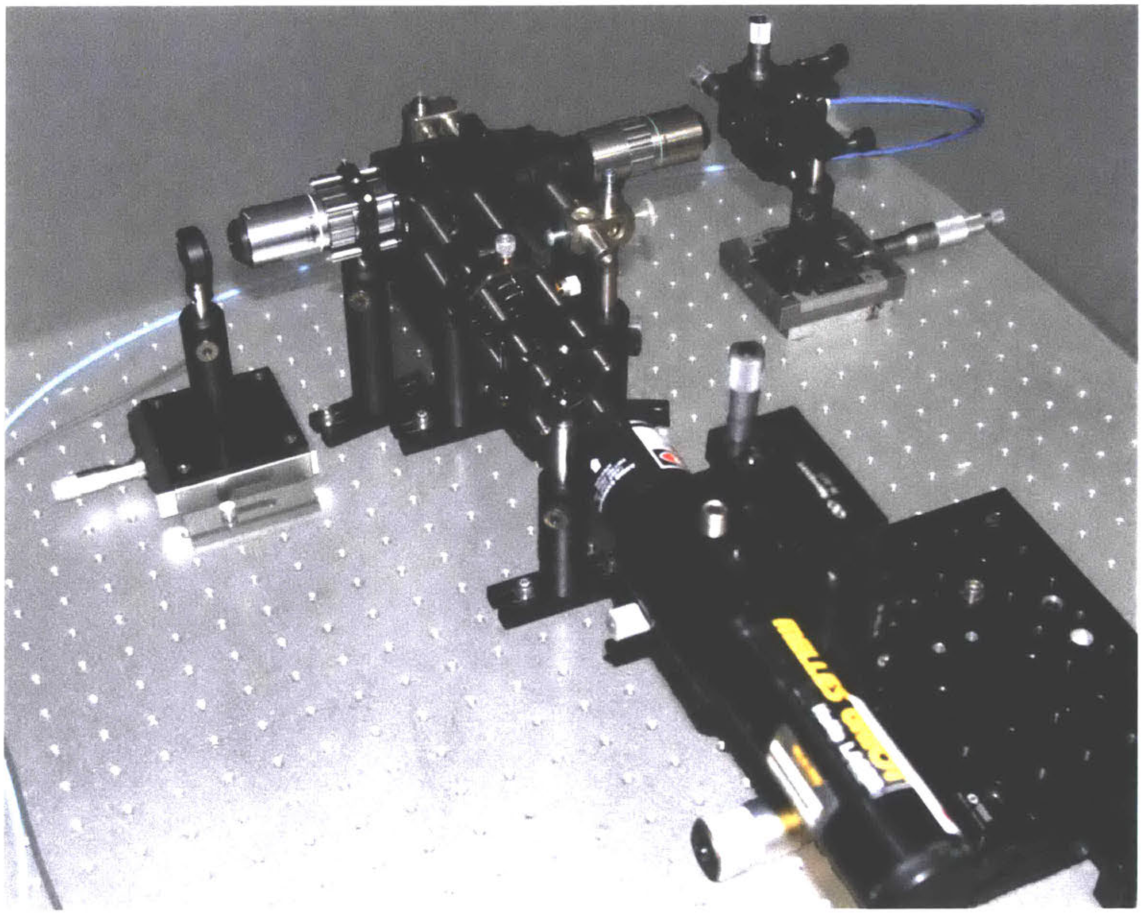

Figure 4-2: Testbed System Realization.

nificant heat, which causes the cavity and mirrors in the tube to expand until they are aligned at the operational temperature. The startup behavior is shown in Figure 4-3. Over 95% of the output intensity is consistently achieved after approximately 10 minutes. The power continued to increase for about one hour, at which point the peak power was reached with dips corresponding to mode hopping in the laser. Competing resonant modes in the laser cavity caused changes in output power, but remained within a margin of 3% and decreased in frequency over time. HeNe lasers are well suited for laboratory-based Raman scattering experiments because they have long-term stable power and frequency. Yet, they are not suited for a compact systems due to their size and extensive warmup time.

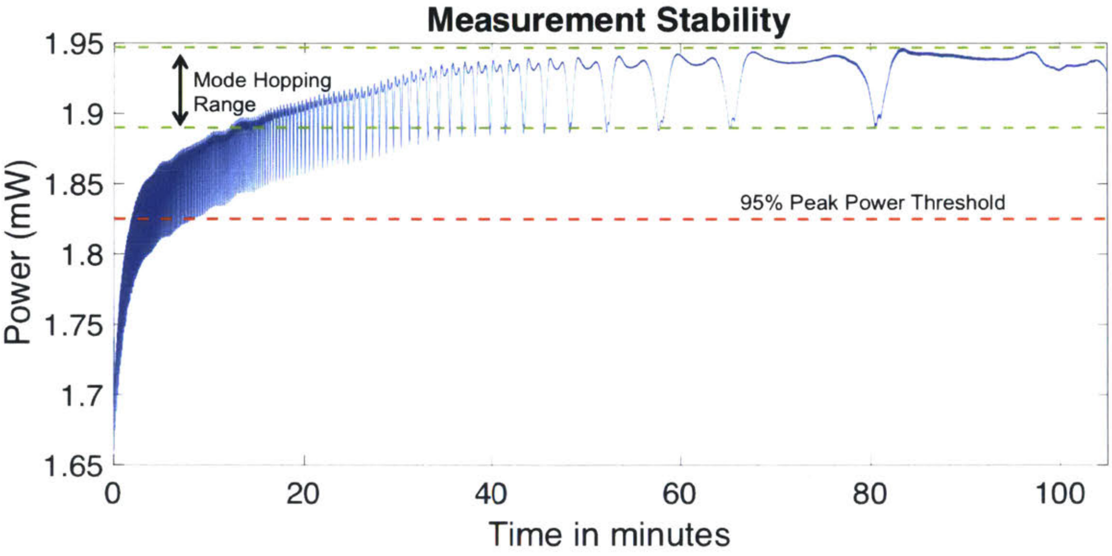

Figure 4-3: HeNe laser warmup.

The second component that required characterization was the dichroic beamsplitter. Obtaining the maximum power at the sample was critical and small changes in the amount of reflected light due to angular misalignment of the dichroic could significantly reduce the Raman scattering intensity. Therefore, an experiment was set up to evaluate the wavelength cutoff sensitivity to angular misalignment by using a rotary stage and broadband light source as shown in Figure 4-4(a). In addition, the transmission and reflection behavior of the dichroic is shown in 4-4(b). The results of the experiment, Figure 4-4(c), show that the sensitivity is approximately

1.2 nm/degree of misalignment. Given the alignment aperture size and spacing, the estimated misalignment should be significantly less than one degree and the reflected power should remain well above 95%. It is also important to note that the relationship was approximated to be linear based on the relatively sparse sampling. Given that the cutoff wavelength was tens of nanometers away from the laser wavelength, further characterization with finer sampling was not necessary.

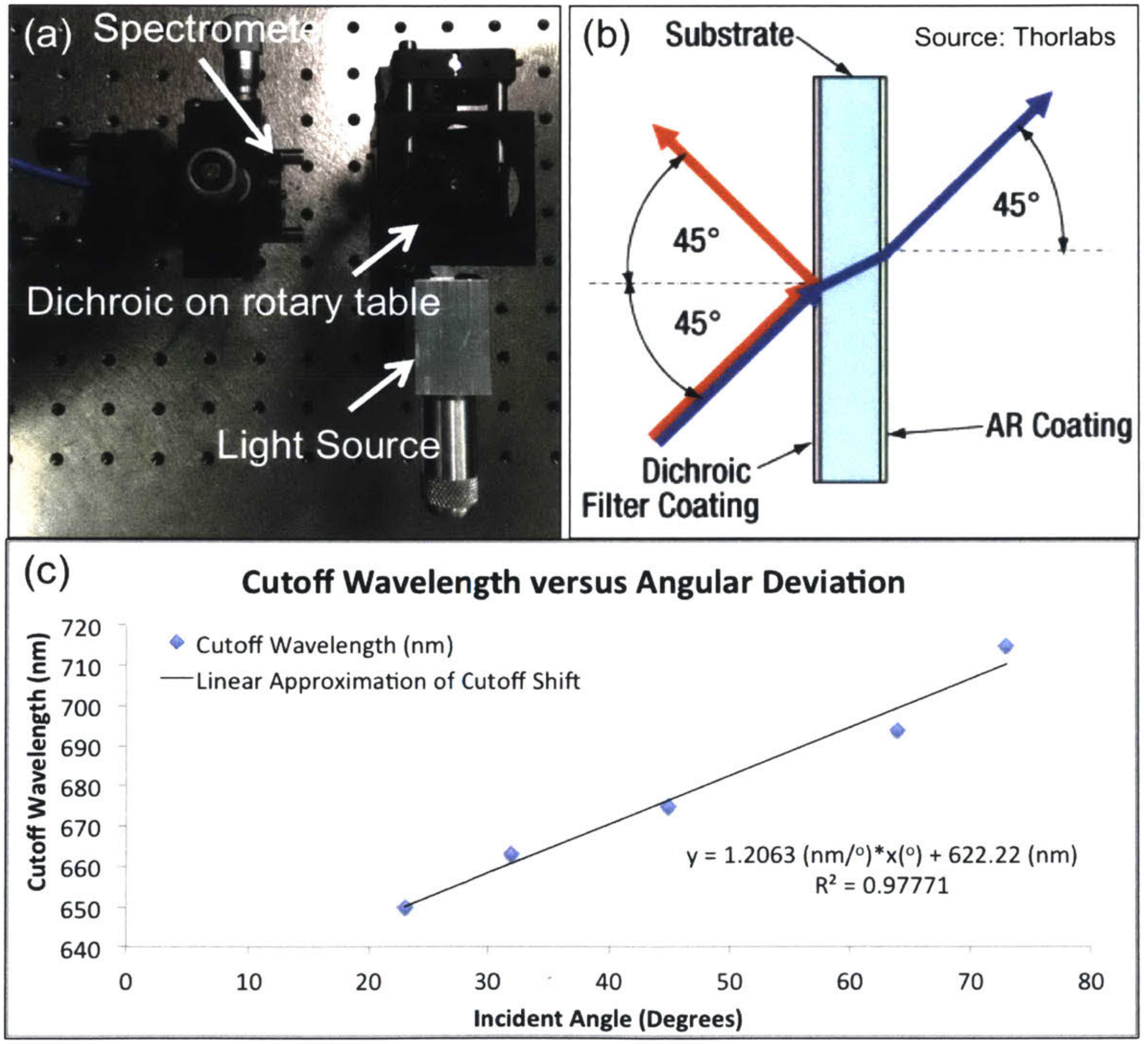

Figure 4-4: Dichroic beamsplitter characterization: (a) Test setup; (b) Dichroic behavior; and (c) Results showing the change in cutoff wavelength versus angle.

4.2.2 Alignment and Performance

Alignment of the system was completed in several stages using a power meter to maximize throughput and reduce system losses. In the first step, the HeNe laser had 3 translational degrees of freedom as well as adjustment in azimuth and elevation. Multiple alignment apertures were used to nominally align the HeNe laser level with the optical table at a given height. Then, focusing through the pinhole was achieved through x-y translation on the pinhole and z-translation on the focusing lens. Once the pinhole was aligned, the next step was to recollimate the beam and align it to the sample using the dichroic. In the final step, a mirror was placed at the sample location and the reflected beam was aligned into the spectrometer. This three-step process is laid out schematically in Figure 4-5.

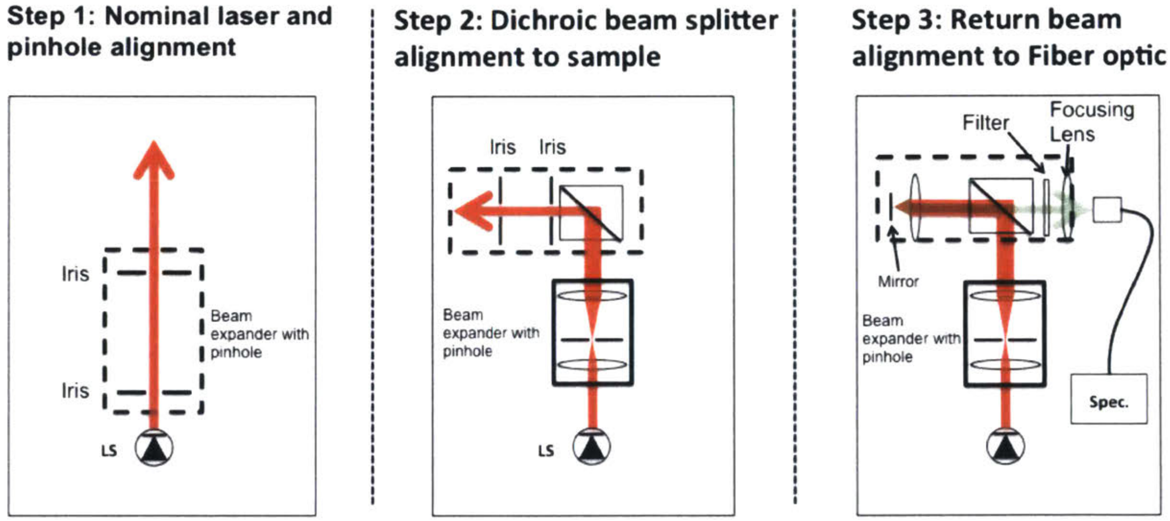

Figure 4-5: Breakdown of the alignment process used for the Type II confocal Raman System.

Once completed, the system was characterized and an evaluation was conducted and benchmarked against data published on existing systems. The results are shown in Figure 4-6 for Chemical Vapor Deposited (CVD) diamond and isopropanol (IPA). The CVD diamond has a characteristic shift at 1332 cm^{-1} that has been well established in the literature and is known to have a large cross-section, or strong relative intensity, compared to other molecules [50]. The associated spectrum of IPA is also consistent with peaks shown in literature that correspond to vibrations of different molecular bonds [59]. Integration times were on the order of 2 seconds and 10 seconds for diamond and IPA, respectively. This data confirms the usability of the setup to measure Raman scattering signals for a number of samples in different phase states.

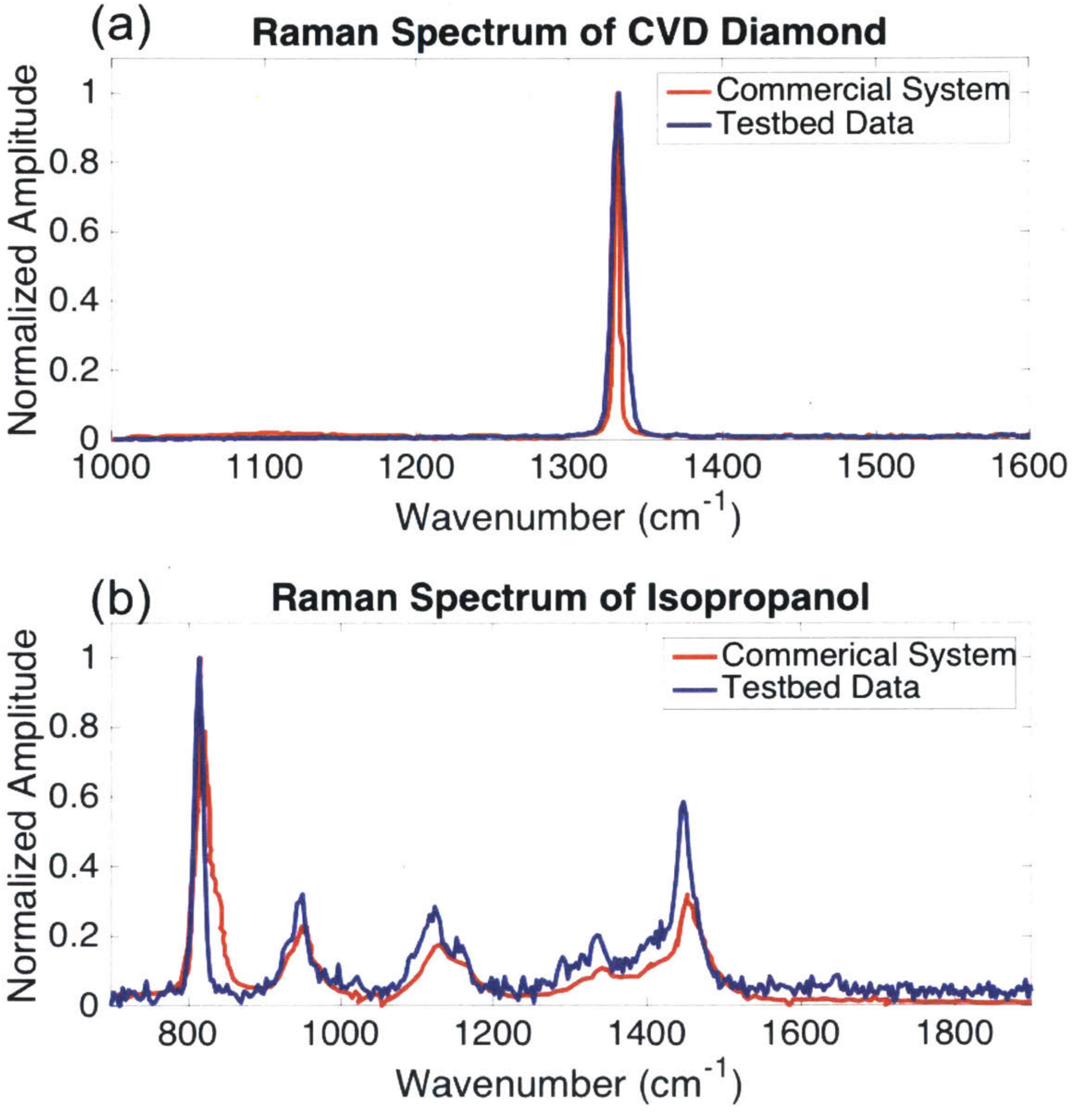

Figure 4-6: Characterization of system by measuring Raman spectra for (a) diamond; and (b) isopropanol.

4.3 Fiber Bragg Grating Integration

The next step in the process was to modify the setup and integrate the FBG. The FBG reflectivity is centered at 633 nm with a tolerance of +/- 0.5 nm. Therefore, the fiber could either be stretched or compressed to match the atomic line of the HeNe laser. Alternatively, the HeNe laser could be replaced with a laser diode module. The benefit of replacing the HeNe with the laser diode module is the increased versatility in measurement and testing of the FBG capabilities. In addition, the laser diode module output wavelength could be changed, since it is temperature sensitive. In theory, Raman scatter should be possible with the laser diode module itself, but with lower intensity and broader spectral lines as the photons are distributed over a wider range of frequencies. The FBG would provide a narrower spectral line once it was integrated. The existing testbed was modified to include a laser diode module along with the FBG. Figure 4-7 shows an updated system setup.

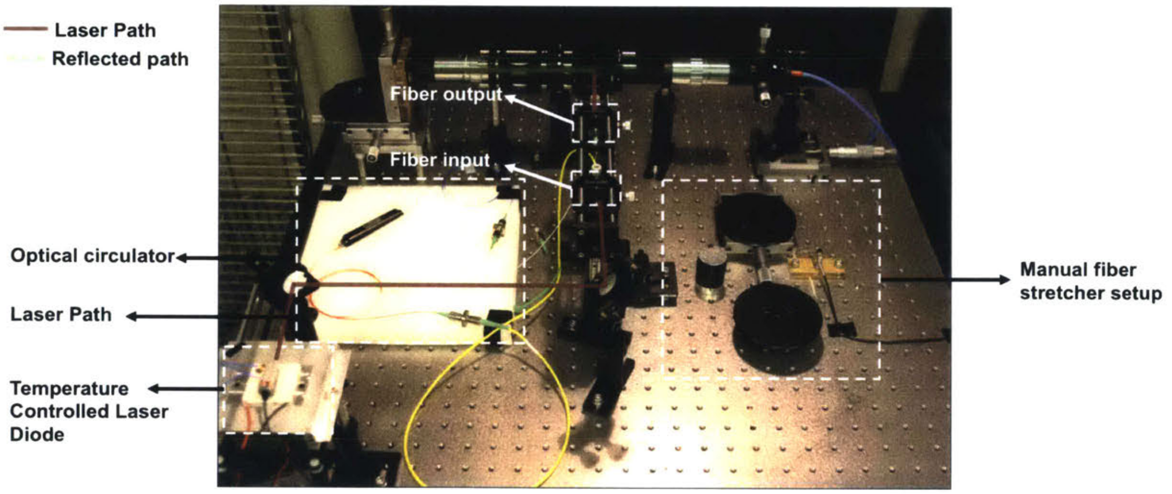

Figure 4-7: Modified system used to test the functionality of the FBG.

The setup consists of a temperature-controlled laser diode module that is coupled into a single-mode fiber. Two mirrors with tip/tilt adjustments were used to couple the free space laser into the fiber. The single-mode fiber was connected to the optical circulator. Then, the output of the optical circulator was connected to the FBG. The FBG was mounted to a custom fiber stretcher, which will be described in more detail in Section 4.3.2. A narrow portion of the beam is reflected and passed back through the same fiber into the optical circulator. The final fiber output from the optical circulator was aligned to the dichroic beam splitter and focused onto the sample. The remainder of the setup is unchanged from Figure 4-2, where the reflected beam from the sample is passed through a filter and coupled into the spectrometer.

4.3.1 Fiber Bragg Grating Characterization

In order to characterize the performance of the FBG, the laser diode module needed to be temperature-controlled and integrated into the setup. The laser diode module was model CPS635S from Thorlabs and had an elliptical output beam profile. Figure 4-8(a) shows the beam profile supplied by Thorlabs. In addition, the temperature sensitivity is shown for three temperatures in 4-8(b). Different modes dominate at different temperatures, which causes the spectrum profile to change accordingly. A high resolution detector is necessary to measure these discrete peaks. The QE Pro spectrometer from Ocean Optics has limited resolution in order to measure a larger bandwidth of the spectrum needed for Raman measurements.

To characterize the temperature sensitivity of the particular diode purchased, a custom setup was necessary. Figure 4-9 shows a schematic of the system. The laser diode module is placed in an aluminum housing that is coated with thermally conductive grease for heat transfer purposes. The aluminum housing interfaces with a thermal electric cooler (TEC) device also using the thermally conductive grease. The TEC was then bonded to an aluminum heat sink using a thermally conductive epoxy. The heat sink has fins that maximize the heat transfer, which is critical to allow the TEC to maintain a reduced temperature on the exposed side. Without the heat sink, the TEC would cool rapidly on one side and then heat transfer would cause the TEC to raise to a higher temperature. A small gap was then left between the heat sink and the cooling fan below to eliminate any vibrations which could be coupled into the laser and cause misalignment.

A picture of the diode mounted to the TEC device on the aluminum plate is shown in Figure 4-9. A thermal simulation was performed in Solidworks that shows the temperature gradient between the top and bottom of the aluminum housing. The

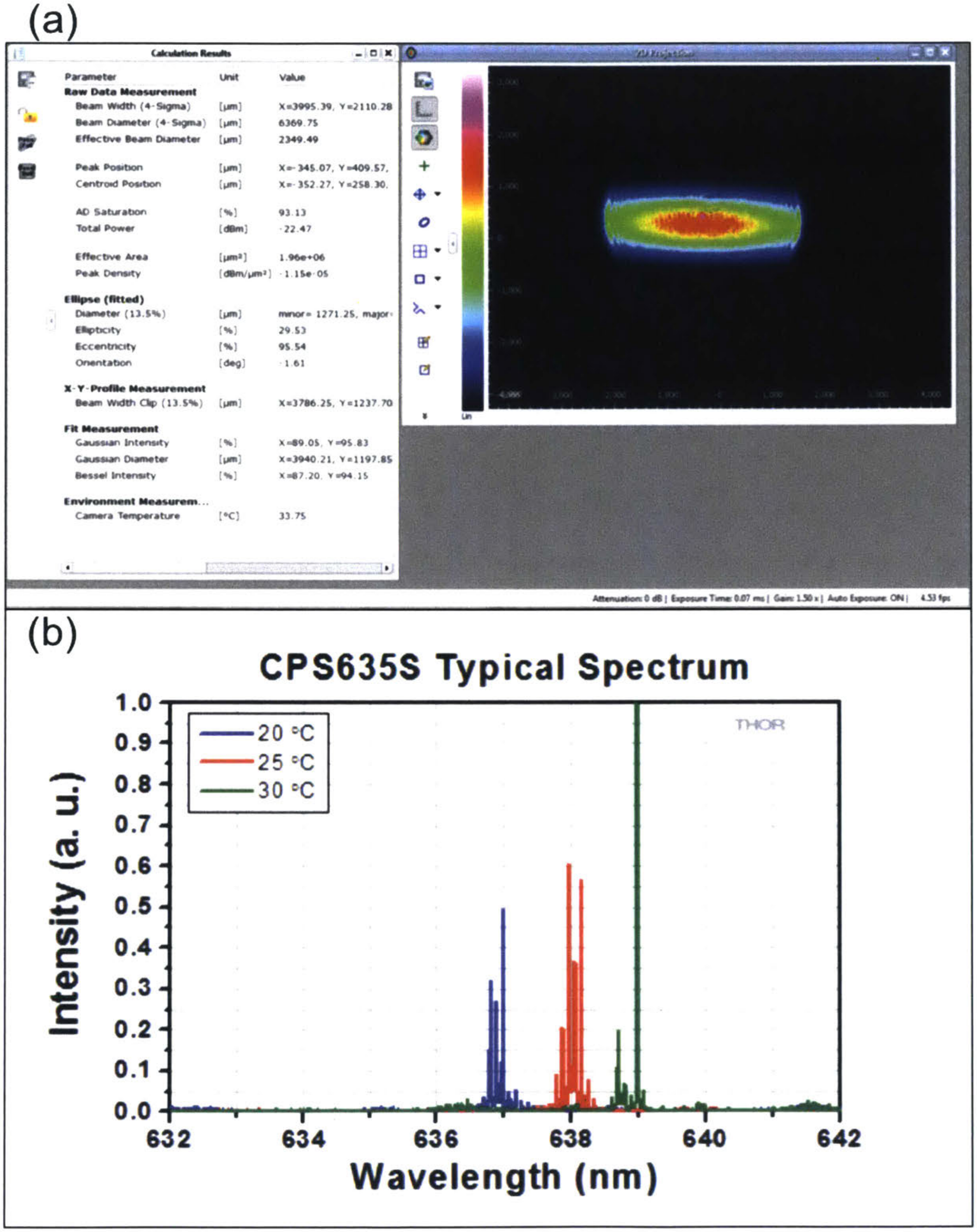

Parameter	Unit	Value
Raw Data Measurement		
Beam Width (4-Sigma)	[µm]	X=3995.39, Y=2110.28
Beam Diameter (4-Sigma)	[µm]	6369.75
Effective Beam Diameter	[µm]	2349.49
Peak Position	[µm]	X=-345.07, Y=409.57,
Centroid Position	[µm]	X=-352.27, Y=258.30,
AD Saturation	[%]	93.13
Total Power	[dBm]	-22.47
Effective Area	[µm²]	1.96e+06
Peak Density	[dBm/µm²]	-1.15e-05
Ellipse (fitted)		
Diameter (13.5%)	[µm]	minor= 1271.25, major=
Ellipticity	[%]	29.53
Eccentricity	[%]	95.54
Orientation	[deg]	-1.61
X-Y-Profile Measurement		
Beam Width Clip (13.5%)	[µm]	X=3786.25, Y=1237.70
Fit Measurement		
Gaussian Intensity	[%]	X=89.05, Y=95.83
Gaussian Diameter	[µm]	X=3940.21, Y=1197.85
Bessel Intensity	[%]	X=87.20, Y=94.15
Environment Measurem...		
Camera Temperature	[°C]	33.75

Attenuation: 0 dB | Exposure Time: 0.07 ms | Gain: 1.50 x | Auto Exposure: ON | 4.53 fps

Figure 4-8: Thorlabs CPS635S laser diode module showing (a) the elliptical beam profile and (b) a typical spectrum for several temperatures.

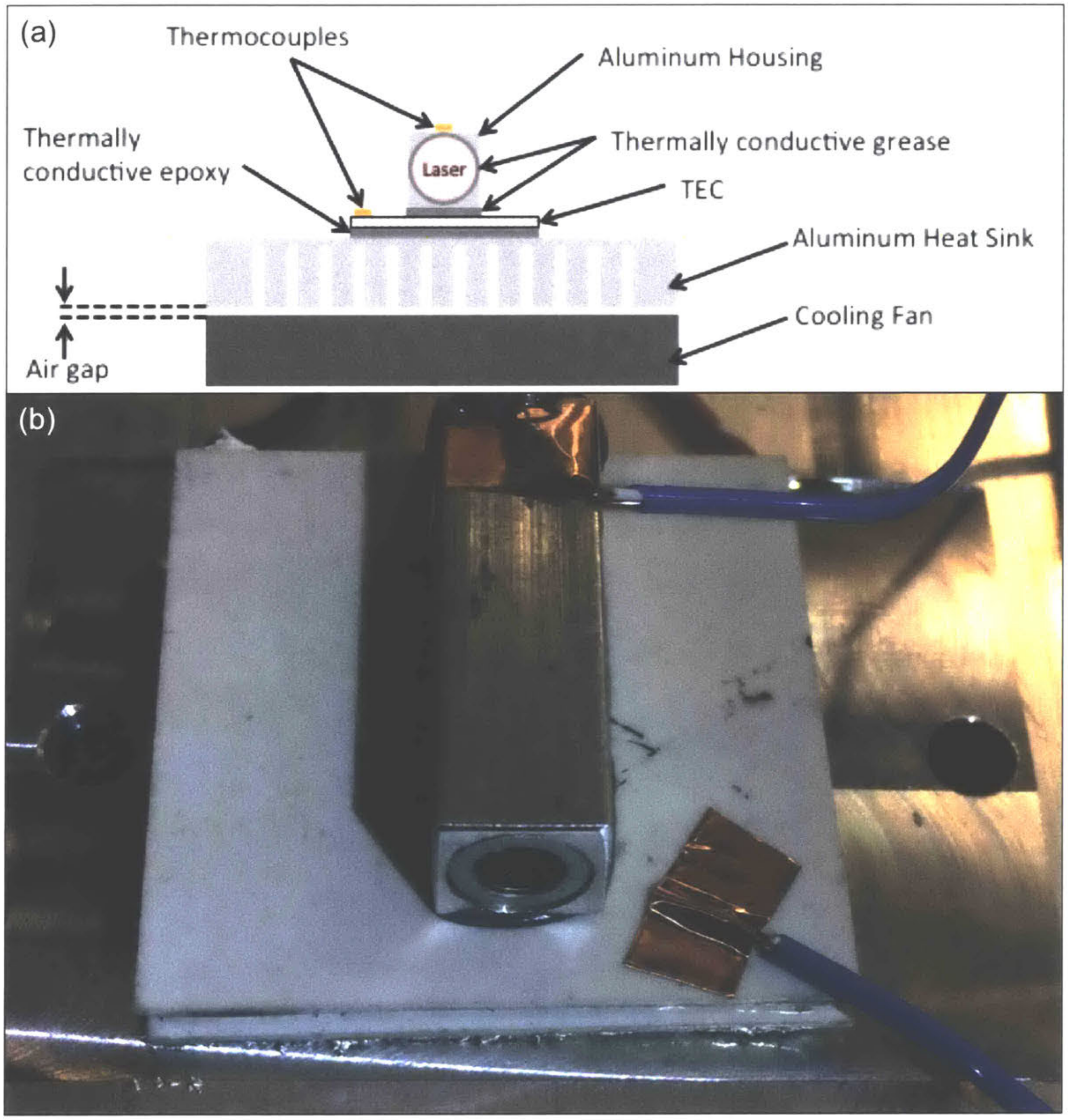

Figure 4-9: Custom system temperature controlled setup showing (a) schematic on the left and (b) diode mounted to the TEC device on the aluminum plate with thermocouples attached using copper tape.

simulated temperature gradient was 0.4 °C. This gradient was minimal when considering the wavelength sensitivity to temperature. Thermocouples were mounted on the TEC device and at the top of the aluminum housing to evaluate the temperature gradient on the actual system. The gradient remained close to the expected 0.4 °C (typically within +/-0.1 °C of this estimate) and was limited by the resolution of the detector at 0.1 °C.

Calibration was performed on the diode by measuring the aluminum housing temperature and comparing it to the output spectrum using the QE Pro spectrometer. The TEC was current-controlled using an Agilent E3632A power supply. The current was adjusted and the TEC temperature and aluminum housing temperature were recorded while the output wavelength spectrum was monitored. The results are shown in Figure 4-10. Wavelength stabilization was achieved after approximately 2 minutes, which was comparatively long, especially for spectroscopic applications. Modulation through the FBG can be done at significantly higher rates given the rapid stabilization from the high stiffness piezo-actuator.

It can be seen that the beam profile remained relatively constant with temperature from Figure 4-10(a). In addition, there was a linear change in output wavelength (measured based on the FWHM) as a function of housing temperature. The temperature sensitivity of the laser diode module was computed to be approximately 0.22 nm/°C. Based on the temperature stability, which was within 0.1 °C, relative to the detector resolution, the wavelength was stable to approximately 1/10th of pixel. Yet, the wavelength could also be adjusted over several nanometers given the TEC temperature range, which is more than sufficient for testing the FBG performance.

4.3.2 Alignment and Performance

The alignment process for this new setup was based on three steps as shown in Figure 4-11. The first step was a nominal alignment of the beam parallel to the optical table. This was completed using two mirrors since the laser position is fixed in this case. By adjusting the position of the mirrors, the beam was aligned through two irises placed at a minimum distance of 10cm apart as shown in Step 1 of Figure 4-11. The

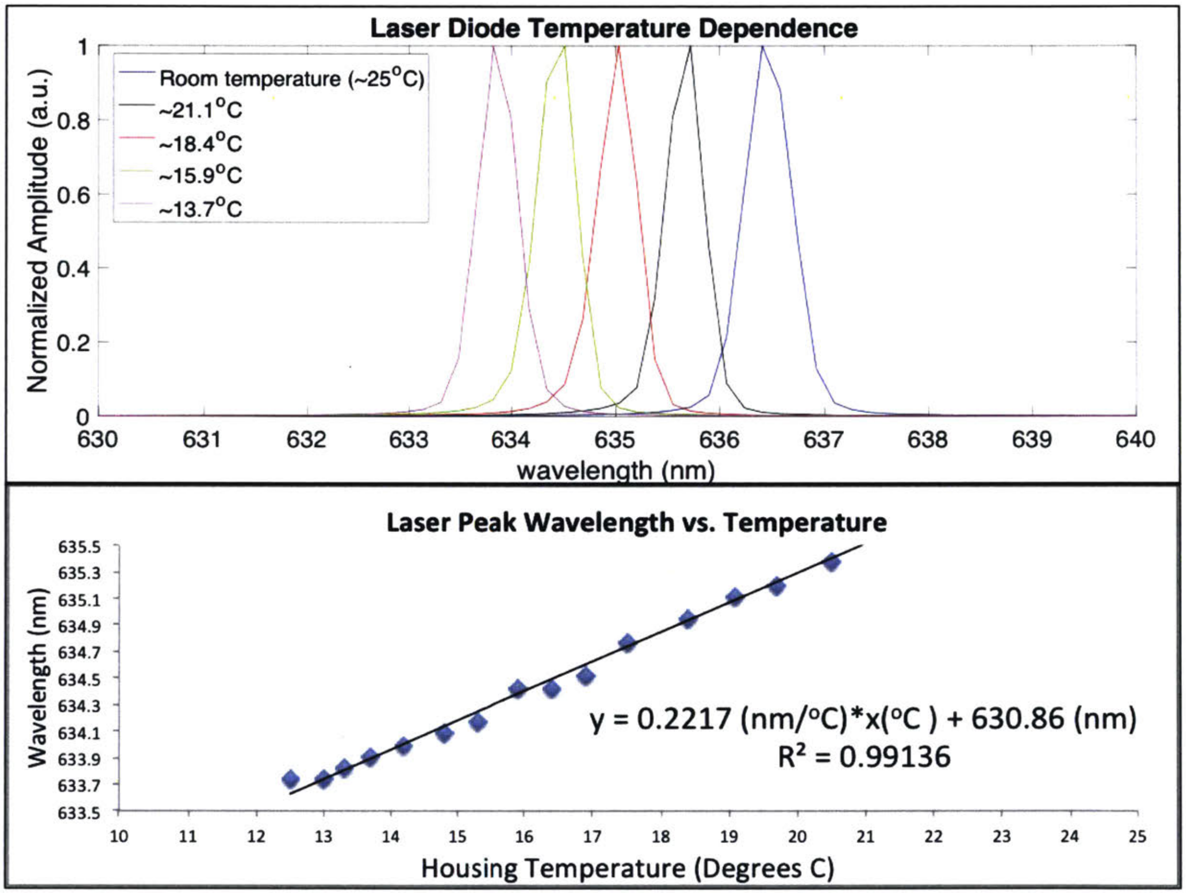

Figure 4-10: Laser diode module temperature sensitivity showing (top) the temperature dependence of the spectrum profile; and (bottom) the center wavelength of the beam versus the housing temperature.

aperture sizes were progressively decreased by closing them to a minimum aperture size of approximately 0.5 mm. At each step in the process, the mirrors were adjusted to maximize the measured power at the exit of the two irises.

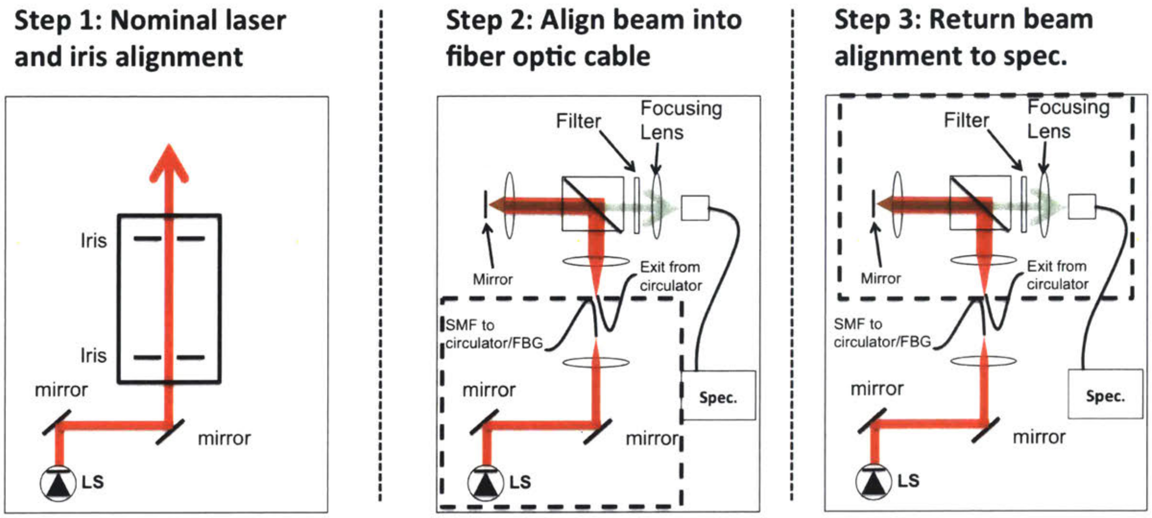

Figure 4-11: Breakdown of the alignment process with modified setup to test the FBG performance.

The second step was to align the beam into a single-mode fiber optic cable. To do this, the location of the two irises were replaced with an aspheric lens mounted onto a z-translation stage, which allowed for adjustment of the focal position of the lens. The aspheric lens focal length was chosen based on the mode field diameter (MFD) and numerical aperture (NA) of the fiber, which is approximately 3.6 to 5.3 μm at 633 nm and 0.10 to 0.14 (respectively) for the given fiber (Thorlabs model number: P3-630A-FC-1). Using Equation 4.1 and the major axis beam diameter, an aspheric lens with focal length of 15.29 mm (Thorlabs model number: C260TMD-B) produces a theoretical beam spot size of 3.2 μm and 0.12NA. The single-mode fiber itself was mounted onto an x-y translation stage for fine adjustment of the position of the fiber relative to the aspheric lens. Before attaching the single-mode fiber, a multimode fiber was used for a preliminary alignment of the x-y-z positions. Then, the multimode fiber was replaced by the single-mode fiber and fine adjustments were made to couple the light. Approximately 30% coupling efficiency was achieved. The coupled light passed through the optical circulator and into the FBG, then the light reflected back through the FBG exited through the circulator.

The third and final step in the alignment process was to align the output beam to the sample. Another aspheric lens was used to collimate the output beam to a diameter that matched the entrance diameter of the Mitutoyo infinity corrected objective lens. In addition, an x-y translation stage was used to adjust the position of the beam to align it to the sample. Back scattered light was collected, filtered, and sent into the spectrometer. The laser diode module provided an opportunity to test the ability of the FBG to filter out unwanted parts of the spectrum, while reflecting only the portion of interest. Figure 4-12 shows the manufacturer-supplied performance of the FBG using an optical interrogator.

There are several important optical characteristics to highlight with this configuration. First, the FBG should produce a narrow beam required for Raman scattering based on the performance data supplied by the manufacturer. The manufacturer was able to achieve a FWHM of approximately 26 picometers, which is well below the required value. Second, the single-mode fiber acts as a spatial filter to circularize the beam. A circular beam profile with a diameter close to the entrance diameter of the Mitutoyo lens at the sample location will produce the smallest laser spot size on the sample, which will increase the Raman scattering intensity. In addition, any portion of the beam profile that is not reflected by the FBG will be filtered out of the spectrum. Therefore, the laser diode module needed to be cooled to a temperature where the output spectrum overlaps the FBG reflected spectrum. The characterization data was critical to finding the overlapping temperature. Once the alignment was complete, Raman scattering data was collected on a diamond sample. The results are shown in Figure 4-13 with a strong Raman scattering signal at approximately 1332 cm^{-1} and some broadband fluorescence present in the spectrum.

Figure 4-13 shows that Raman scattering is attainable from the narrow reflected beam of the FBG. Thus, this result provides the first "**Proof of concept 1**" outlined earlier in this chapter. The next step was to show that a strain in the fiber causes a shift in the Raman scattering signal relative to the broadband fluorescence. Since the strain sensitivity of the FBG was unknown, a custom fiber stretcher was needed

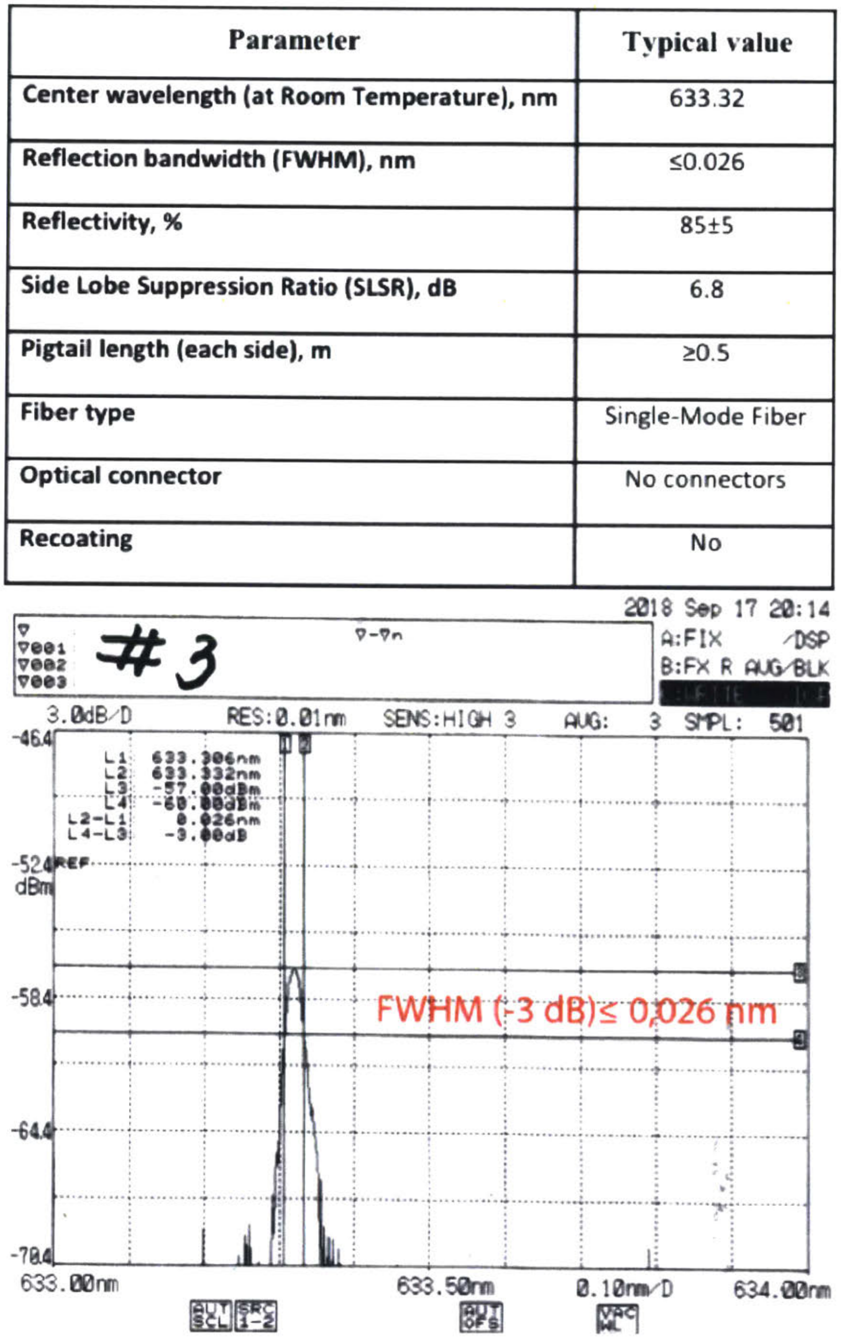

Parameter	Typical value
Center wavelength (at Room Temperature), nm	633.32
Reflection bandwidth (FWHM), nm	≤0.026
Reflectivity, %	85±5
Side Lobe Suppression Ratio (SLSR), dB	6.8
Pigtail length (each side), m	≥0.5
Fiber type	Single-Mode Fiber
Optical connector	No connectors
Recoating	No

Figure 4-12: Performance characteristics of the FBG as supplied by the manufacturer *Novae Laser*.

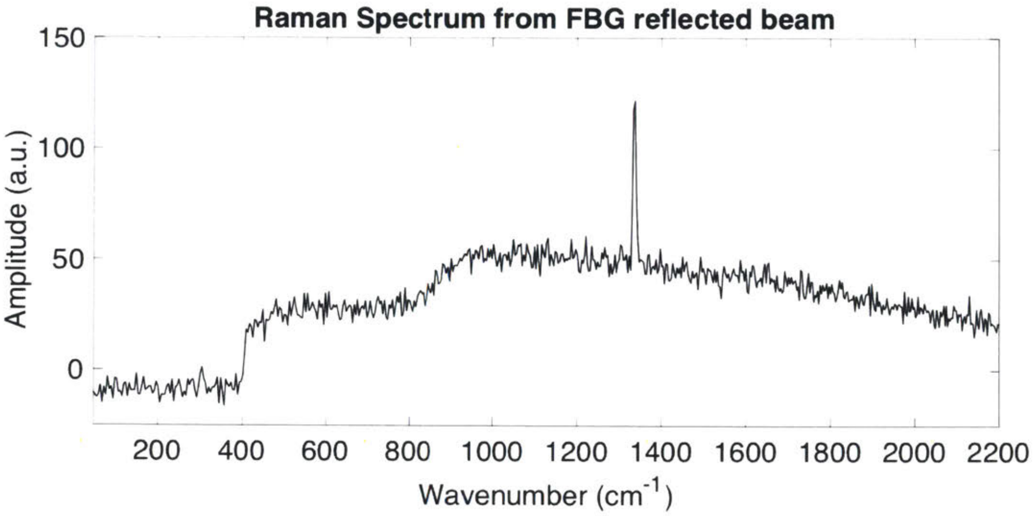

Figure 4-13: Raman spectrum of CVD diamond obtained using the reflected beam from the FBG.

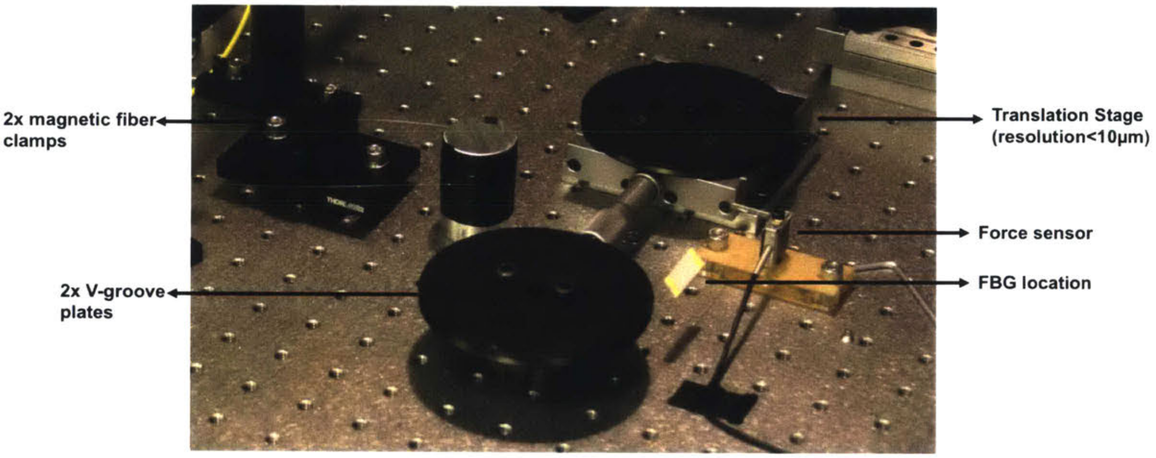

Figure 4-14: Custom fiber stretcher setup.

prior to bonding the FBG to a linear piezo-actuator. The design of the fiber stretcher is shown in Figure 4-14. Two v-groove plates hold the fiber roughly parallel to the optical table. One of the v-groove plates was held fixed and the other was attached to a translational stage with a resolution of less than $10\,\mu m$. The free ends of the fiber were then wrapped multiple times around a cylinder with a 1 cm radius and secured to two magnetic fiber clamps. Frictional forces held the fiber in position around the cylinder.

A force sensor was then placed under the fiber near the location of the FBG to bias the fiber in the vertical direction relative to its position in the v-groove.

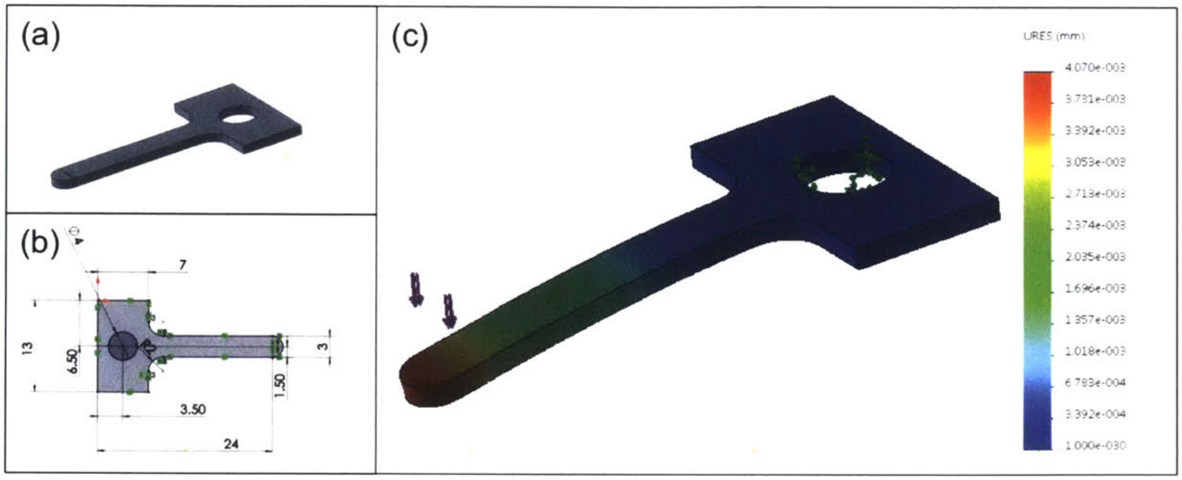

Figure 4-15: Force sensor cantilever showing: (a) the design; (b) the dimensions of the cantilever given in millimeters with a thickness of 1 mm; and (c) a simulation showing the displacement with 1 mN of force applied.

Attached to the force sensor was a cantilever beam as shown in Figure 4-15. This biasing provided a measurable force on the cantilever beam that was recognized as a change in voltage through the sensor. A cantilever beam was utilized rather than directly measuring the force on the sensor because the beam provided the ability to estimate vertical displacement of the fiber. Depending on the tension in the fiber, the relative force applied to the cantilever beam would change resulting in a corresponding displacement. Figure 4-15 shows the design of the cantilever, which was laser cut from ABS plastic. Solidworks simulations were performed to estimate the stiffness of the cantilever.

Without the use of the cantilever and force sensor, estimations of the strain would be inaccurate because it would be difficult to estimate compliance in the fiber during straining. To achieve accurate measurements of the displacement of the cantilever beam, the force sensor required calibration. Weights were placed on the end of the cantilever and the corresponding voltage was measured through an oscilloscope. The graph shown in Figure 4-16 shows the force versusversus voltage calibration curve, which is approximately linear.

An analytical model was generated that supported the experimental data and estimated a strain sensitivity in the FBG. This basic setup schematic of the system

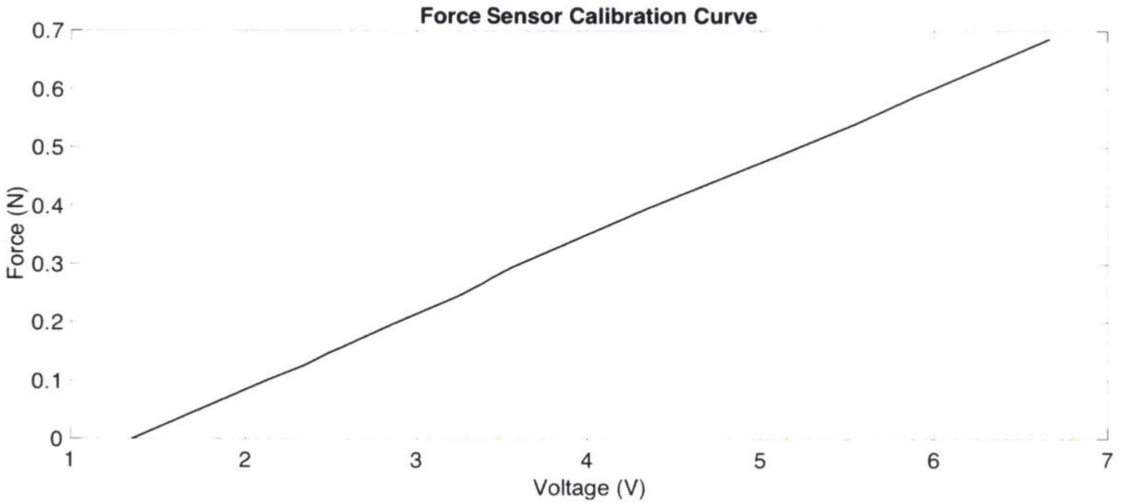

Figure 4-16: Force sensor calibration curve.

is shown in Figure 4-17. One end of the fiber optic cable was fixed and the other end was able to move horizontally through the micrometer stage by an amount, δ_h. As the tension in the fiber increased, the force on the cantilever also increased, which caused the cantilever to displace by an amount, δ_v. The most important values are the relative change in position of the fiber. Measurements were recorded at three positions: (1) the voltage on the oscilloscope that corresponds to the force sensor, (2) the position of the micrometer, and (3) the peak position of the reflected spectrum as measured by the spectrometer.

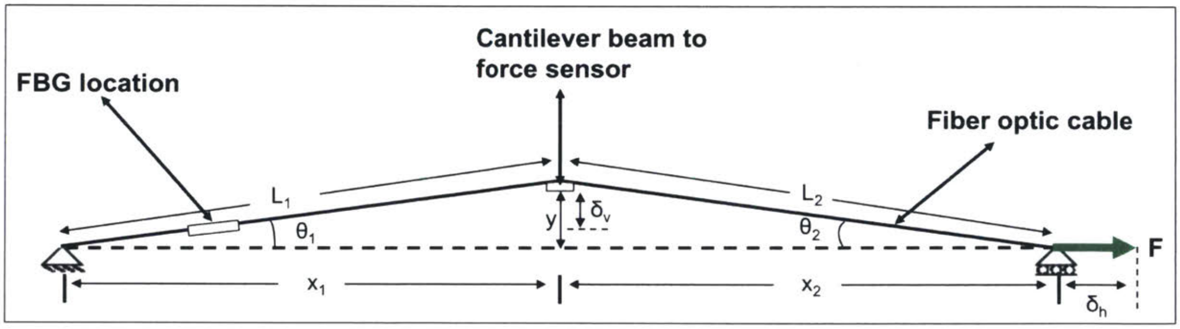

Figure 4-17: Schematic showing the configuration of the custom fiber stretcher along with the designated nomenclature used in computing the strain sensitivity of the FBG.

The strain was computed by calculating the initial and final lengths of the fiber at two positions. The change in length divided by the initial length defines the strain as given by,

$$\epsilon = \frac{\Delta L}{L} = \frac{L_{final} - L_{initial}}{L_{initial}}. \tag{4.2}$$

Furthermore, the initial and final lengths of the fiber were broken into two segments. The first segment, L_1, spans the fixed end of the v-groove plate to the force sensor cantilever location. The second segment, L_2, spans the force sensor cantilever location to the moveable v-groove plate attached to the micrometer translation stage. Each of these have initial and final states, given by a subscript i and f, respectively, as:

$$L_{initial} = L_{1i} + L_{2i}; \qquad L_{final} = L_{1f} + L_{2f}. \tag{4.3}$$

There is an assumption that the fixed and moveable ends are nearly level and collinear, such that they share a common side of the triangle given by the vertical offset from the force sensor cantilever where $y_1 = y_2 = y$. It can be seen that the length of each segment in the initial positions can be calculated from the geometry as given by,

$$\theta_{1i} = atan(\frac{y}{x_1}); \qquad \theta_{2i} = atan(\frac{y}{x_2}), \tag{4.4a}$$

$$L_{1i} = \frac{x_1}{cos(\theta_{1i})}; \qquad L_{2i} = \frac{x_2}{cos(\theta_{2i})}. \tag{4.4b}$$

In the same way, the final lengths of the fiber were computed by taking into account the measured vertical and horizontal displacements of the beam measured by the force sensor cantilever and micrometer, respectively. Again, these equations are based on the change in geometry and shown in,

$$\theta_{1f} = atan(\frac{y - \delta_v}{x_1}); \qquad \theta_{2f} = atan(\frac{y - \delta_v}{x_2 + \delta_h}), \tag{4.5a}$$

$$L_{1f} = \frac{x_1}{cos(\theta_{1f})}; \qquad L_{2f} = \frac{x_2 + \delta_h}{cos(\theta_{2f})}. \tag{4.5b}$$

The horizontal displacement was measured directly using the micrometer, but the deflection of the cantilever had to be computed based on the geometry and the applied load. The geometry was shown previously in Figure 4-15 and the modulus of elasticity for ABS plastic was approximated at 2 GPa. Again, the force was estimated from the calibration curve given the output voltage of the sensor. These values were substituted into,

$$\delta_v = \frac{FL^3}{3EI}. \tag{4.6}$$

The complete analytical solution for the strain can be computed through the substitutions of the above equations into the original strain formula, Equation 4.2. In addition, the following identity can be used: $cos(atan(x)) = (\sqrt{1+x^2})^{-1}$. The complete analytical solution for the strain in the FBG is:

$$\epsilon = \frac{\left[x_1\sqrt{1+(\frac{y-\delta_v}{x_1})^2} + (x_2+\delta_h)\sqrt{1+(\frac{y-\delta_v}{x_2+\delta_h})^2}\right] - \left[x_1\sqrt{1+(\frac{y}{x_1})^2} + x_2\sqrt{1+(\frac{y}{x_2})^2}\right]}{\left[x_1\sqrt{1+(\frac{y}{x_1})^2} + x_2\sqrt{1+(\frac{y}{x_2})^2}\right]}. \tag{4.7}$$

In the final step, the corresponding wavelength as measured by the spectrometer was subtracted to determine the shift in wavelength (based on the FWHM) corresponding to the strain. The strain sensitivity is approximately 2.5 picometers per microstrain in the fiber,

$$\boxed{\textbf{Strain Sensitivity} \approx \frac{2.5pm}{\mu\epsilon}}. \tag{4.8}$$

The sensitivity above was important to calculate because it determined whether attaching to a piezo-actuator would produce enough strain to meet the project requirements. A linear piezo-actuator from Physik Instrumente (PI) produces approximately

$1000\,\mu\epsilon$, which was enough to shift the Bragg wavelength by approximately 2.5 nm. This means that only small changes at a relatively low voltage of the piezo-actuator were needed to achieve the goal of 0.25 nm wavelength shift; thus, the actual power requirements for this application are significantly lower than that required to drive the piezo-actuator through its full dynamic range.

The difference spectrum obtained by shifting the FBG is shown in Figure 4-18 as a result of subtracting the two data sets. The profile corresponds to the shift in Raman scattering of the diamond sample at 1332 cm^{-1} and resembles a derivative profile of the Raman peak resulting from the small shift in wavelength. Figure 4-18 verifies "**Proof of concept 2**" and "**Proof of concept 3**" outlined earlier in the chapter, showing that the derivative spectrum could be obtained from the FBG without a significant change in the fluorescence spectrum profile at this wavelength (i.e. Kasha's rule). This fluorescence profile that was shown as the broadband offset starting at approximately 400 cm^{-1} in Figure 4-18 has now been eliminated, as it remained constant during the straining of the FBG and the corresponding change in input wavelength.

Once verified experimentally, the FBG could then be permanently bonded to a linear piezo-actuator. The stiffness of the epoxy was critical as it affects the strain transfer, since shear deformation reduces the effective transferred strain between the piezo-actuator and the fiber [60]. This is reflected in the value of the hardness. Moreover, the adhesive needed to have low shrinkage during curing and the curing process must be completed at room temperature. Any areas of localized high stress could result in a different portion of the spectrum being reflected relative to the other parts of the FBG. The result would be a broadening effect on the reflected beam and thus the Raman spectrum. In the worst case, the Raman spectrum would no longer be attainable. Based on these requirements and the general requirement of compatibility between the piezo material and the silica glass with acrylate coating, the following three adhesive candidates were selected:

Samples were made using each adhesive with bare fiber and a comparison was made. Based on the surface area of the bond and the applied strain from the FBG,

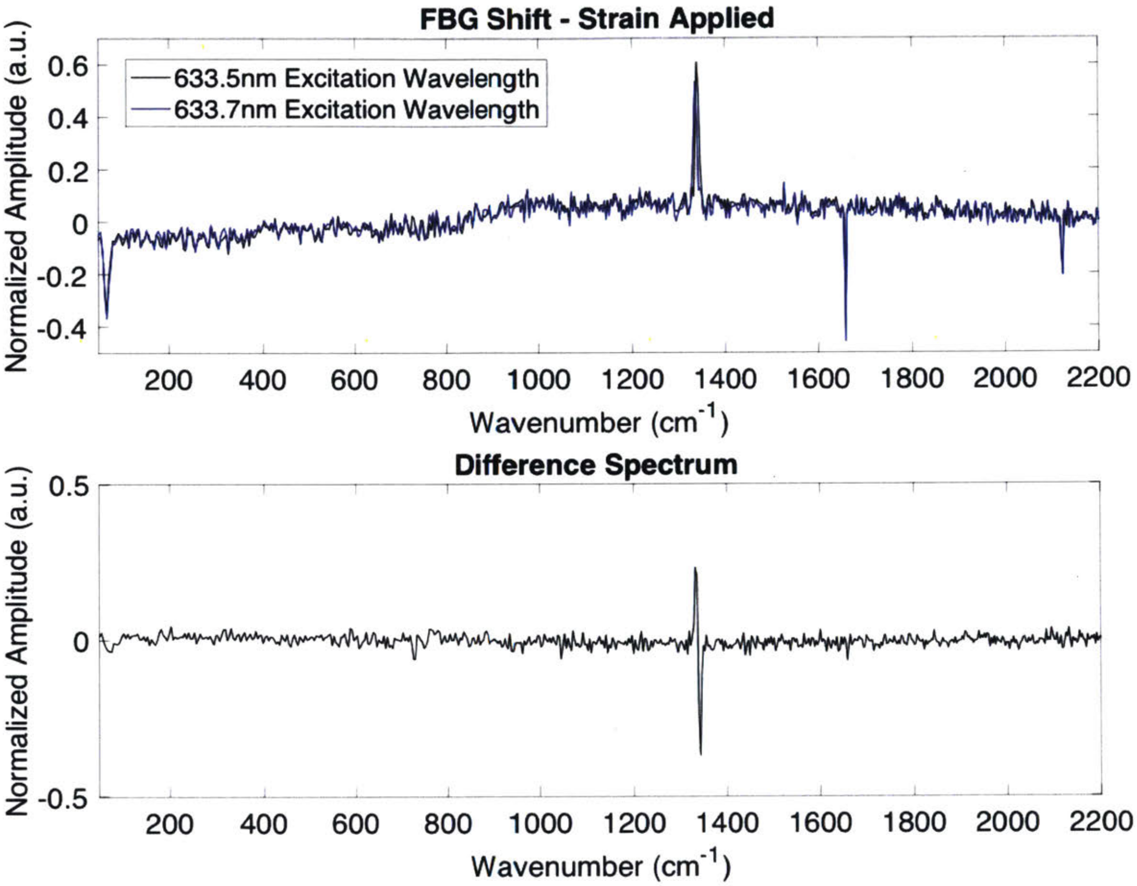

Figure 4-18: Difference spectrum obtained by straining the FBG and subtracting the dataset from the data obtained for the unstrained FBG.

Table 4.1: Adhesive Selection

Parameter	Epo-Tek 301-2	Masterbond EP30LTE-2	Eccobond F112
Viscosity	0.3 Pa·s	850 Pa·s	1.8 Pa·s
Hardness (Shore D)	80	90	86
Cure Schedule	80 °C 3 hours or Room temp 2 days	Room temp 3 days	Room temp 1 day
Lap Shear Strength	13.8 MPa	13.1 MPa	17.2 MPa
CTE	61 m/m°C	12 m/m°C	62 m/m°C

the maximum shear stress was estimated to be on the order of 1 MPa. Therefore, all adhesives had sufficient strength. However, in practice there was a significant difference in behavior. The low viscosity of the Epo-Tek adhesive was found to provide poor coverage and, therefore, it was expected that this would result in poor strain transfer. Alternatively, the Masterbond adhesive had a high viscosity and resulted in air entrapment. The major concern with air entrapment was unequal strain transfer from the piezo to the FBG. The Eccobond proved to be the most promising in terms of controllability, maximum shear strength, and cure properties. Therefore, it was used to bond the FBG.

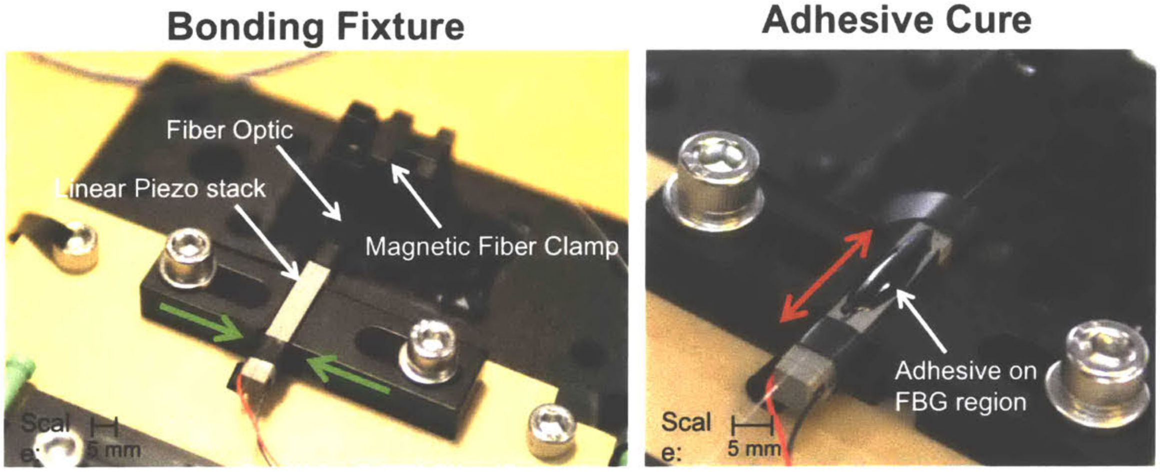
Bonding Fixture

Adhesive Cure

Figure 4-19: FBG bonding fixture with the FBG position along the piezo before bonding (left) and after bonding (right).

Alignment of the FBG to the piezo-actuator was critical to maximize the strain transfer. In order to achieve this, the piezo-actuator was clamped into a fixed position and two magnetic fiber clamps were used to hold the FBG in axial alignment. The FBG was then pressed parallel against the piezo surface. The fixture is shown in the Figure 4-19 (left) with the fiber across the top of the piezo-actuator along with the final bond shown in Figure 4-19 (right). Once the cure was complete, the performance of the FBG was evaluated by applying a voltage to the piezo-actuator and measuring the shift in the reflected spectrum. One noteworthy point is that the piezo-actuator acts as a capacitor. Therefore, to discharge it rapidly, a resistor was added in parallel. A power supply was used to apply a voltage of up to 100 V and the spectrum was recorded every 5 V. The reflected spectrum is shown in Figure 4-20.

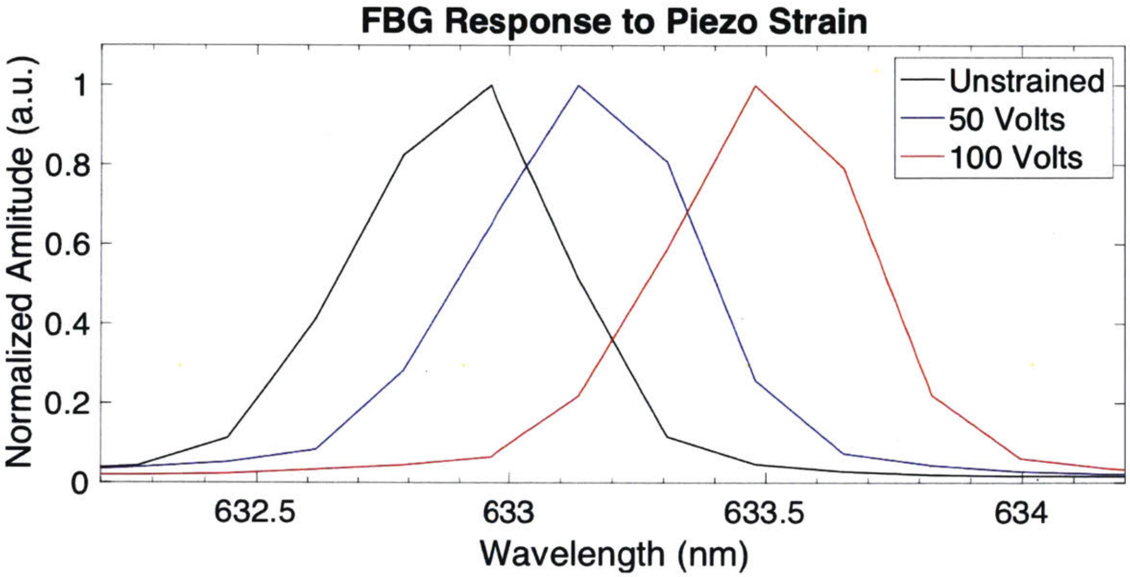

Figure 4-20: Reflected spectrum from the FBG as a function of applied voltage.

Figure 4-20 shows that the spectrometer did not have the resolution to accurately determine the center wavelength of the FBG. Therefore, it is unclear if there was any "broadening" of the FWHM of the beam that resulted from the bonding. Despite this, the center wavelength was estimated to find the transferred strain sensitivity of the FBG. In order to do this, the voltage from the piezo-actuator was converted to a strain value given the calibration curve from the piezo-actuator manufacturer. Figure 4-21 shows that the transferred strain sensitivity is on the order of $0.7\,\mathrm{nm}/\mu\epsilon$. This is less than 30% of the computed strain sensitivity with the manual fiber stretcher. Yet, this can be accounted for by the fact that there is compliance from the adhesive that results in a lower relative strain seen by the FBG. In addition, if there is any offset from the surface of the piezo-actuator then this would also account for the discrepancy. The portion of the FBG with the grating was bare, but the remainder of the fiber had a thicker acrylate coating. It was this acrylate coating that was pressed against the surface of the piezo, which left a minimum offset of approximately $60\,\mu m$.

Another important aspect of bonding the fiber to the piezo-actuator was the creep from a constant stress applied to the polymer based adhesive. However, given the cycle times, which are on the order of seconds, and relatively low applied stress, this

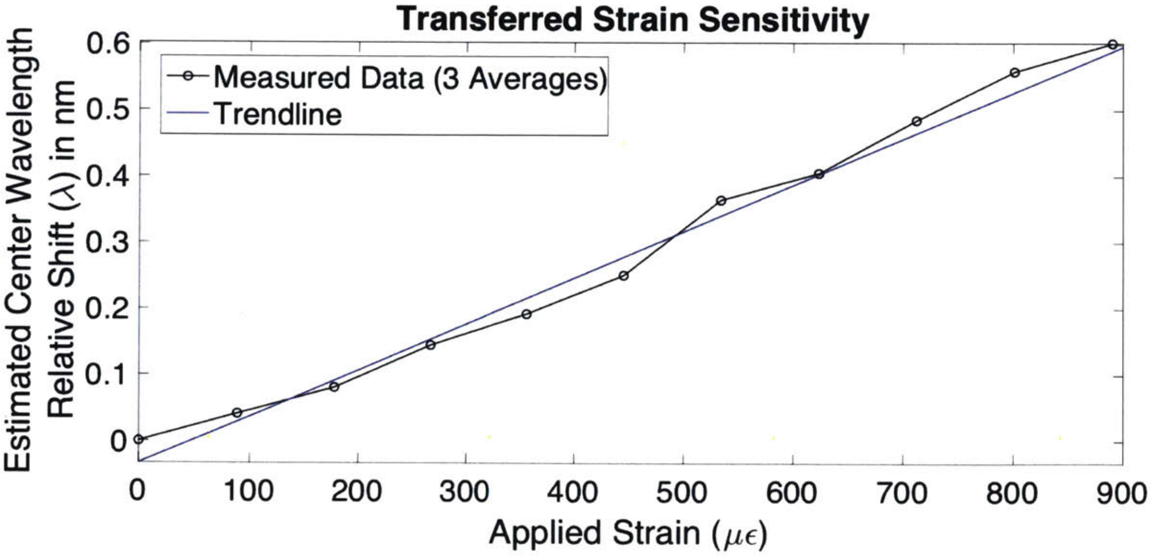

Figure 4-21: Relative shift in reflected spectrum from the FBG as a function of strain.

effect was not noticeable. In addition, small changes in the strain of the FBG were not noticeable given the resolution of the detector and the narrow FWHM of the reflected beam from the FBG. It was anticipated that the largest source of error would be the repeatability of the piezo, which was on the order of 5% of the nominal value.

4.4 Superluminescent Diode Integration

To verify the final proof of concept (i.e. "**Proof of concept 4**"), the SLED had to be integrated into the setup to replace the laser diode module. The SLED was supplied by a company located in Switzerland called Exalos (http://www.exalos.com). The company offers two options at 635 nm center wavelength: (1) a 14-pin butterfly package with internal cooling and (2) a TO-56 can package with no cooling. Both options did not come with a internal monitor photodiode (MPD) for power stabilization at that time. As will be seen, the greatest source of power fluctuation was alignment jitter. Contrary to the laser diode module used in the previous setup, temperature changes in the single-mode device only effect the output power with little impact on the spectral profile.

Selection of the SLED packaging type was based on the maximum power output.

The 14-pin butterfly package was simpliest to integrate, but provided only about 20% of the power as compared to the TO-56 can package at about 5 times the cost. Considering the narrow reflected spectrum of the FBG, obtaining the most power was critical. Therefore, the TO-56 can was selected and mounted to a heat sink for temperature stability. The most challenging aspect of this portion of the design was coupling this light into a single-mode fiber since the FWHM vertical and horizontal divergence angles from the TO-56 can were 40° and 12°, respectively.

Figure 4-22 shows the modified setup with the SLED integrated. The mechanics of the setup remain consistent with Figure 4-7, but the SLED setup is magnified for more detail. Given the large divergence angles, collimating the light at the exit of the diode was critical to maximize the coupling efficiency. A 0.75 high numerical aperture objective lens with a short working distance of 0.66 mm was used to collimate the light source. Given the short working distance, accurate positioning of the lens was critical, so it was mounted onto an x-y translation stage for adjustment. In this case, the x-axis represented the optical axis, or the change in focal position of the lens. The SLED was mounted onto a tip-tilt stage, which ensured that the face of the SLED was parallel to the face of the objective lens. Collimation was completed by projecting the beam over approximately 4 m. In addition, any misalignment at this distance would be more pronounced such that fine adjustments could be made to improve the beam quality, as shown in Figure 4-23.

Theoretical calculations estimate that a majority of the power could be coupled into the single-mode fiber given the numerical aperture, collimated beam size, and focusing lens characteristics. Yet, it became evident that the collimated beam quality determined how much light could be coupled into the single-mode fiber. A higher quality beam produced the smallest spot size and improved the coupling efficiency to a greater extent as compared to small changes in focal length of the focusing lens into the single-mode fiber.

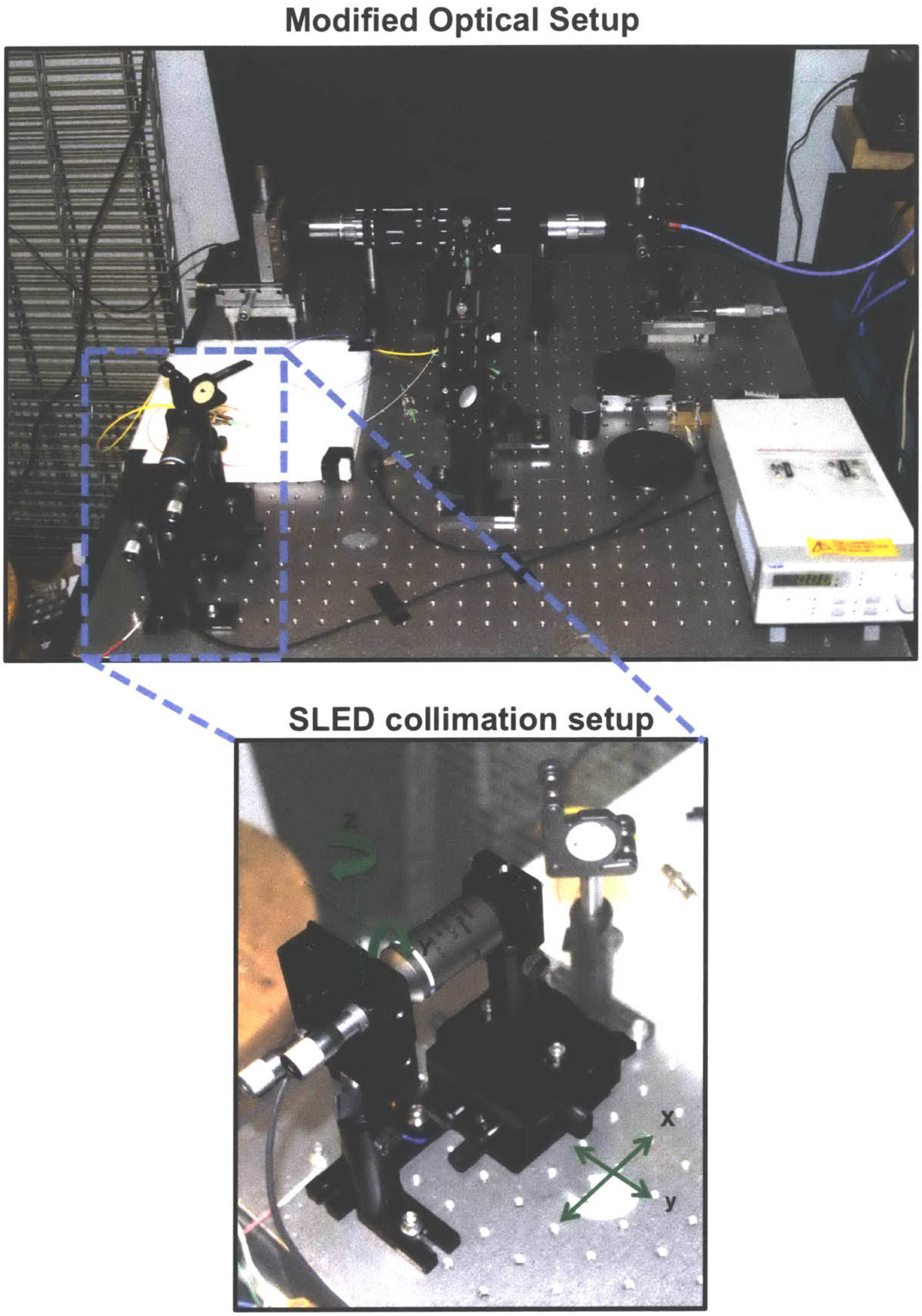
Modified Optical Setup

SLED collimation setup

Figure 4-22: Modified optical setup with integrated SLED.

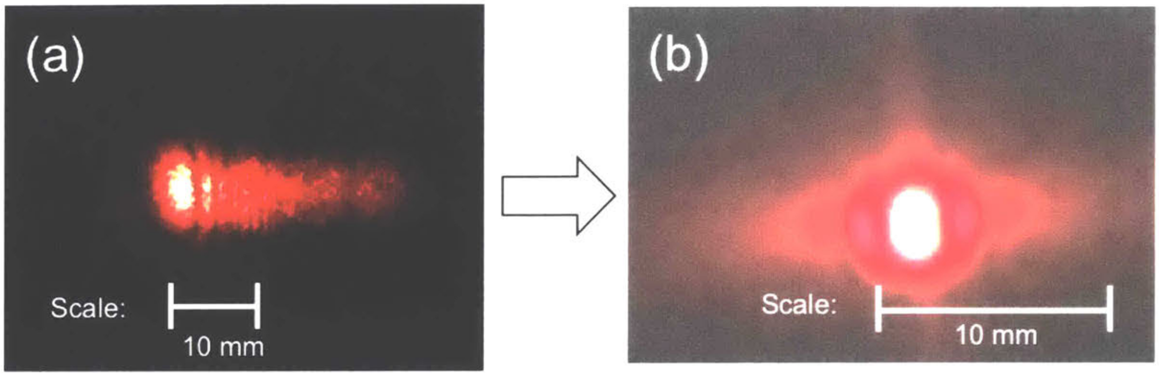

Figure 4-23: Collimated beam from the SLED measured at about 4 meters from the source showing (a) diffraction due to transverse misalignment of the beam; and (b) improved beam quality from better alignment.

4.4.1 Superluminescent Diode Characterization

The SLED device was operated using a current controller. Therefore, the output power versus current curves had to be characterized on the collimated beam. The power was specified at 10 mW with an operating current at 55 mA and maximum current of 65 mA. As can be seen from the characterization curve shown in Figure 4-24, the 10 mW power was achievable at 60 mA, indicating that a majority of the light was being collimated through the objective lens.

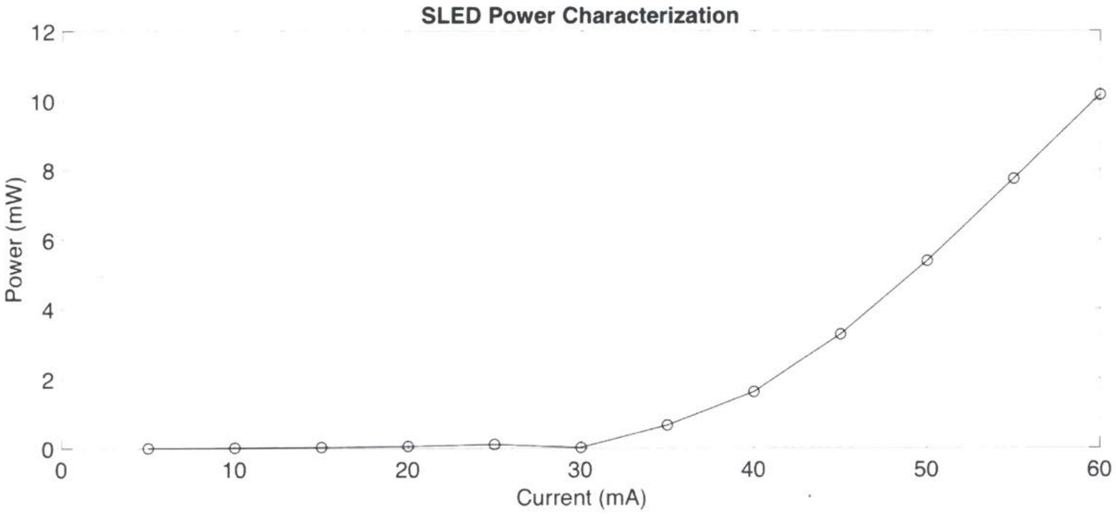

Figure 4-24: Characterization of the power as a function of current.

The next step was to characterize the profile of the SLED spectrum. Exalos specifies a relatively wide range for their center wavelength and a large deviation from

633 nm would make the FBG incompatible. Small deviations could be compensated by biasing the FBG through compression or extension. Again, the QE pro spectrometer from Ocean Optics was used to measure this spectrum and the profile is shown in Figure 4-25.

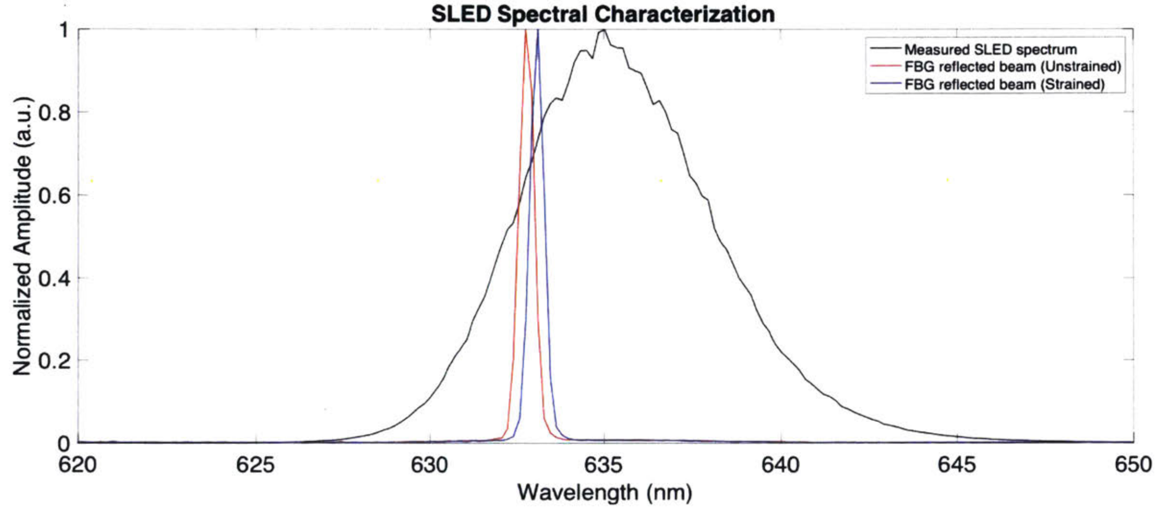

Figure 4-25: SLED spectral profile (black line) along with the narrow filtered portion of the spectrum after FBG filtering in an unstrained (red line) and strained (blue line) position.

The spectral profile of the SLED is centered around 635 nm with a FWHM consistent with the manufacturer's specifications. The red and blue lines shown in Figure 4-25 show the reflected profile from the SLED in the unstrained and strained configurations, respectively. The FBG could be centered by biasing the fiber to compensate for this offset. In addition, other parts of this spectrum can be utilized through the integration of more FBGs in series.

4.4.2 Alignment and Performance

The alignment process was completed in the same manner described in Section 4.3.2, where two mirrors are used to align the beam into a single-mode fiber. The same mechanics of the single-mode fiber remained unchanged. The maximum power coupled into the fiber was approximately 35%. However, there was a significant challenge in maintaining this coupled power level as vibrations caused small drifts in the power levels. This can be seen from the graph in Figure 4-26 showing the coupled power at about 35 mA. The single-mode fiber is directly connected to the power meter to make this measurement.

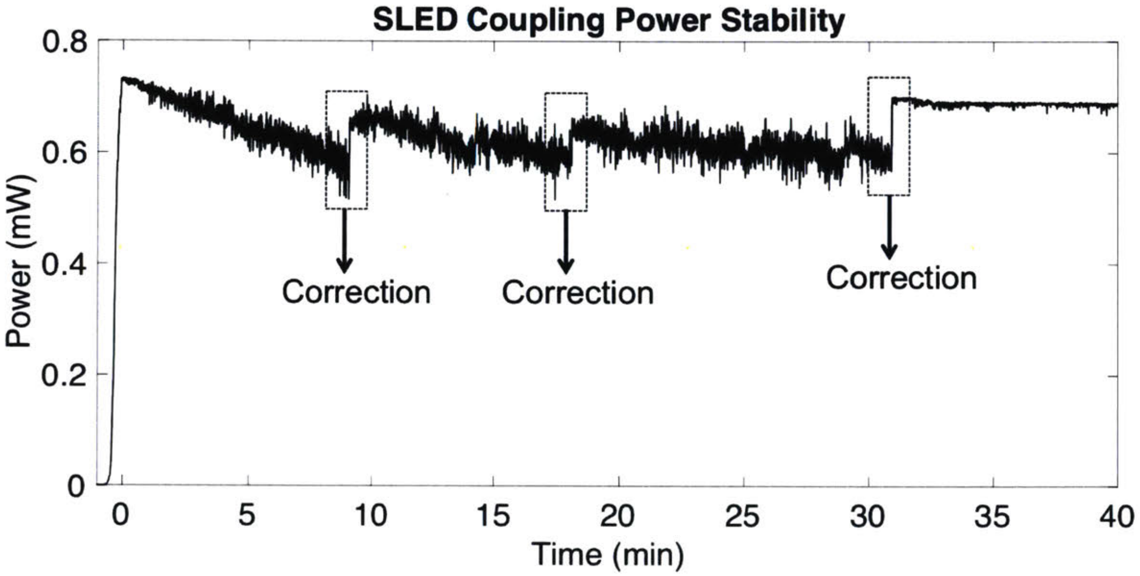

Figure 4-26: SLED power stabilization showing fluctuations, drift, and areas of manual correction in alignment.

Figure 4-26 shows that power fluctuates significantly. Corrections were made manually in the locations indicated on the graph. It was discovered that the root cause of this was the diode mount with tip/tilt adjustments. The springs were stiffened on the tip/tilt plate, which lead to a significant reduction in vibration as shown after the third correction in the graph.

The system schematic outlined in Figure 3-2 has now been fully developed and characterized. Figure 4-27 shows the schematic and the developed system. With all the elements integrated together, "**Proof of concept 4**" could be proven out to show that these components work together to obtain a Raman difference spectrum.

The same diamond sample, as discussed in Section 4.2.2, was used to make Raman measurements and the difference spectrum was obtained. These results are shown in the Figure 4-28. The top graph shows the raw data in the strained and unstrained condition with spectral features at lower wavenumbers corresponding to non-Raman features. The bottom graph corresponds to the difference spectrum. Given the rela-

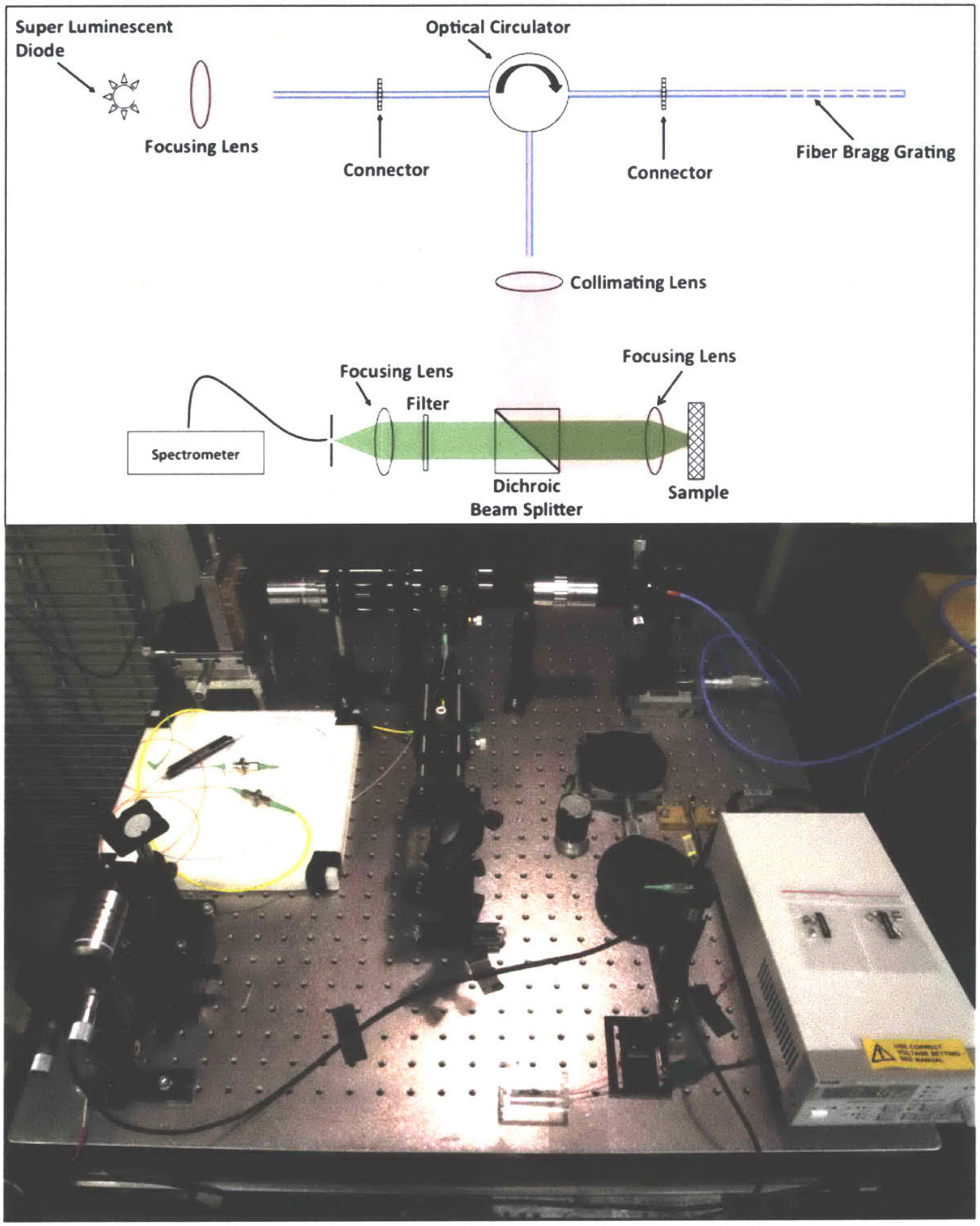

Figure 4-27: System schematic (Top) and the developed system (Bottom).

tively weak signal from the FBG, the corresponding Raman scattering signal is weak. Importantly, however, this proves out the key functional aspects of the system, which are the combination of the FBG and SLED for use in a shifted excitation Raman system to differentiate between Raman scattering and non-Raman scattering spectral features.

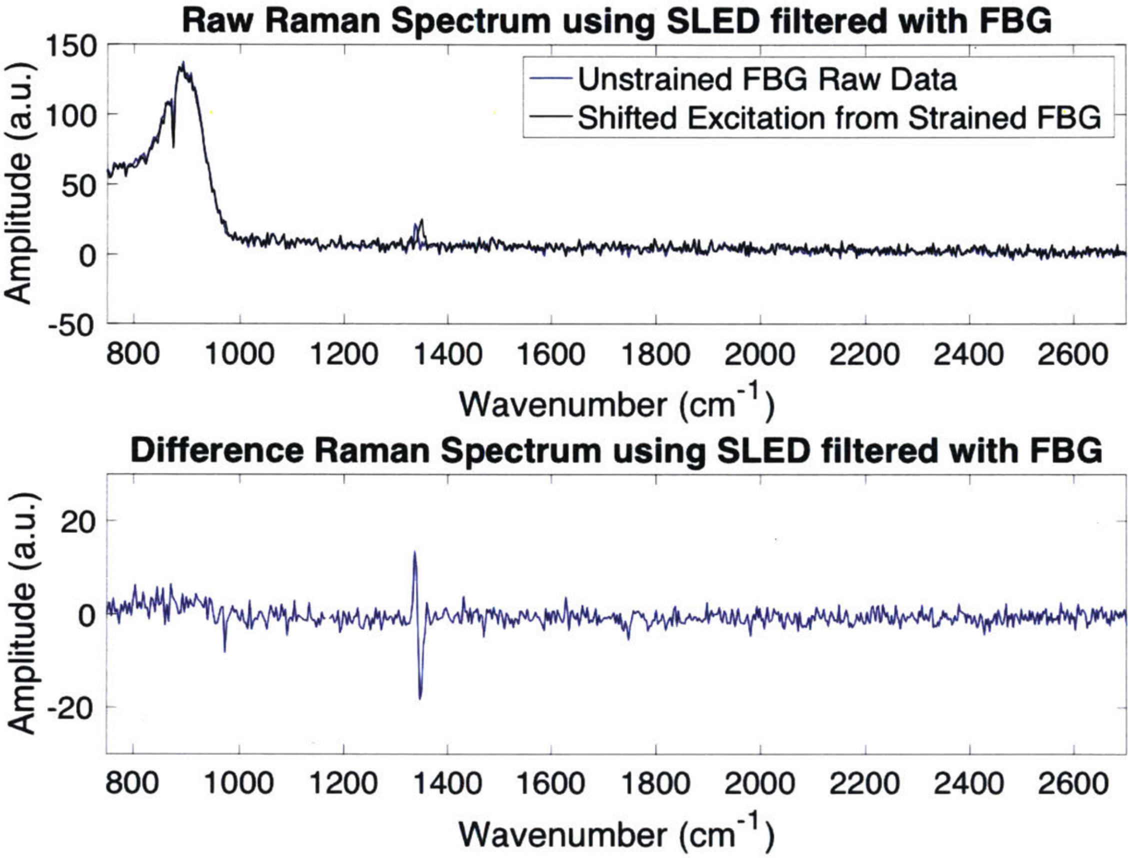

Figure 4-28: Raw Raman spectrum of diamond (top) under two different excitations and the difference spectrum obtain from subtracting the two spectra (bottom).

To summarize, a novel hardware approach to rapidly modulate between laser excitation wavelengths was outlined and the progression through the design and development phase has been presented. The remaining chapters will discuss a novel signal processing approach that requires precise synchronization of all elements of the system. The approach to this will be discussed as well as the application of shifted excitation techniques to Surface Enhanced Raman Spectroscopy.

THIS PAGE INTENTIONALLY LEFT BLANK

Chapter 5

Signal Processing

The following section will outline the traditional signal processing approach as well as the novel methods implemented in this project. A comparison of the techniques will be conducted and the advantages and disadvantages will be outlined. The focus of this discussion will be based on the dispersive-element multichannel spectrometer, specifically the Ocean Optics QE Pro, which was used in the system development setup. The design of this spectrometer is shown in Figure 5-1.

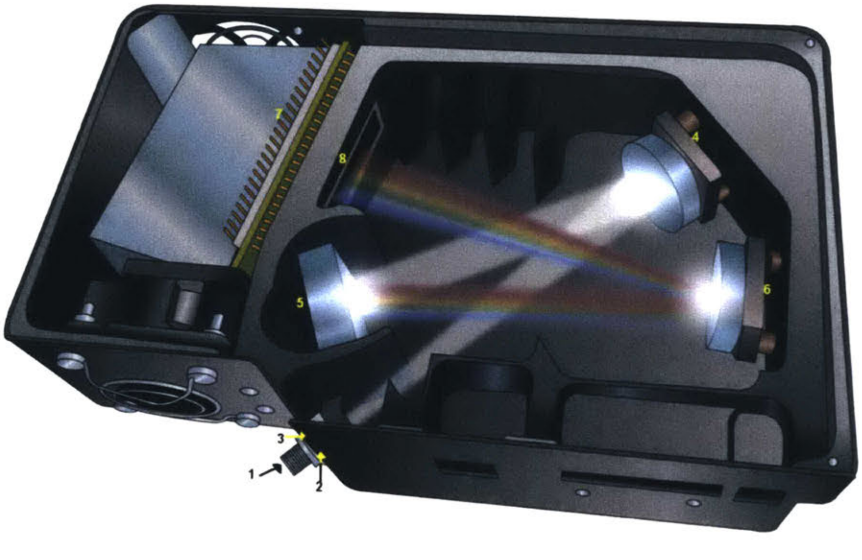

Figure 5-1: Ocean Optics QE Pro spectrometer showing the internal components for device operation (taken from [16]).

Light enters the Ocean Optics QE Pro spectrometer through a narrow entrance slit (item 2 in Figure 5-1). A diffraction grating (item 5) is used to separate the light by wavelength, which is then projected onto a back-thinned CCD (item 8). The entrance slit width, the groove density, and the pixel size define the resolution of the spectrometer. As the groove density increases and the entrance slit width decreases the resolution increases. In terms of device operation, each pixel on the CCD will correspond to a small range of wavelengths that is defined by the resolution.

The device allows the user to change several parameters, including the integration time, number of averages, and detector temperature. In terms of performance, Figure 5-2 shows how the dark current is reduced with decreasing temperature. This becomes important in cases where the fluorescent noise may be low and dark current contributes to the noise in the data. Reducing the temperature of the detector can dramatically decrease both the DC offset and the variance in a given pixel associated with the dark current. The sharp peak around 675 nm corresponds to a high dark count pixel.

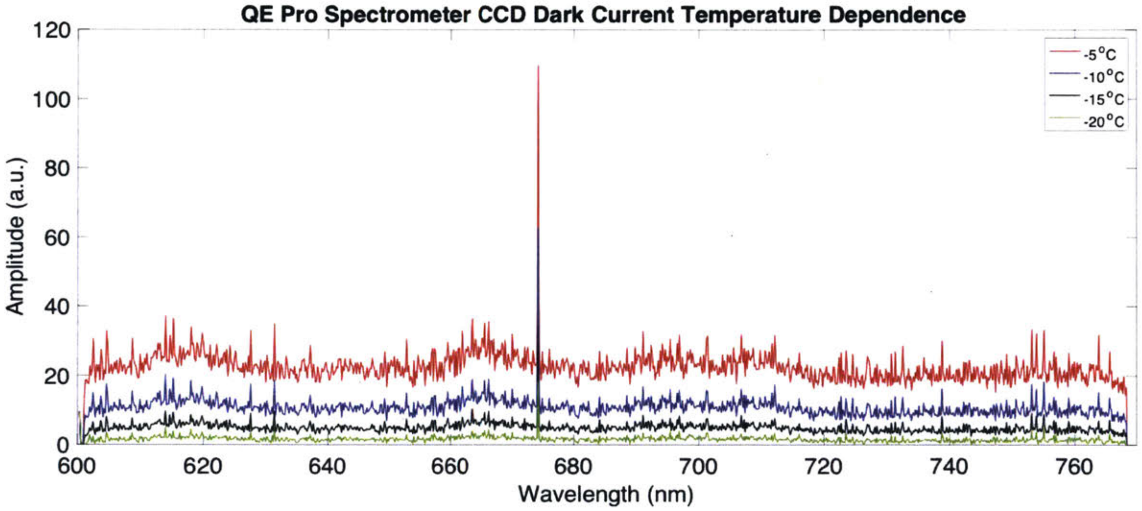

Figure 5-2: Dark current as a function of the detector temperature.

In addition to the functionality described above, this spectrometer can support a number of triggering configurations, which allows syncing to external subsystems in the setup. This includes synchronization with an external power meter to track laser power and synchronization with the strain condition on the fiber. This versatility allows for significant flexibility in testing different modulation methods as described in the proceeding sections.

5.1 Conventional Raman Data Processing Method

In regards to Raman Spectroscopy, the conventional approach to data processing has been the subtraction of data sets. One measurement can be considered a "dark spectrum", which is subtracted from the measurements containing the Raman scatter from the sample. High-pass filters can also be applied to the data to remove low frequency components in the spectrum, while maintaining the characteristic high frequency Raman scattering features. Yet, any artifacts that may be present due to environmental contamination (i.e. stray light) or fluorescence will still be present. This can be seen by looking at the equation for the total signal in a given spectrum,

$$S_T(\lambda_i) = [S_R(\lambda_i) + S_F(\lambda_i)]f(\lambda_i) + S_B, \tag{5.1}$$

where S_T is a vector containing the amplitude of the total signal across the spectrum as function of wavelength for a given input excitation (λ_i). The intensity of the Raman signal (S_R) and the fluorescence signal (S_F) are a function of the wavelength. These are multiplied by the geometric parameters defining the optical response of the system and the sample characteristics as defined in Chapter 3, which are represented by the term f. The background signal, S_B is independent of the input excitation, but may vary with wavelength depending on the environmental conditions (i.e. stray light). Subtracting the "dark spectrum" removes the S_B term in Equation 5.1, but leaves the fluorescence spectrum (S_F) term unaffected. This assumes that the background is relatively constant between measurements, which is typically the case for a stable system. The shifted excitation approach has two distinctly different input excitations as,

$$S_T(\lambda_1) = [S_R(\lambda_1) + S_F(\lambda_1)]f(\lambda_1) + S_B, \tag{5.2a}$$

and

$$S_T(\lambda_2) = [S_R(\lambda_2) + S_F(\lambda_2)]f(\lambda_2) + S_B. \tag{5.2b}$$

For small shifts in the input excitation, we can assume that $S_F(\lambda_1) \approx S_F(\lambda_2)$ and $f(\lambda_1) \approx f(\lambda_2)$. This implies that the fluorescence spectrum and the response of the optical system are roughly constant for a small change in wavelength. Subtraction of Equation 5.2a from Equation 5.2b results in

$$\Delta S_T = [S_R(\lambda_1) - S_R(\lambda_2)]f(\lambda_1) \approx \frac{\partial S_T}{\partial S_R}. \tag{5.3}$$

Therefore, the final spectrum contains only information regarding the Raman scatter signal. For small shifts in excitation this signal resembles the partial derivative of the signal with respect to the Raman signal. This is the origin of the term "derivative feature" in regards to the Raman scatter when the difference between two spectra are taken at different input excitations. In order to reconstruct the original signal, the derivative spectrum can be integrated:

$$S_T = \int \frac{\partial S_T}{\partial S_R} + C. \tag{5.4}$$

Reconstructing the original signal is a critical step in order to categorize the chemical components. There are significant collections of data that break down the Raman spectrum of different bonds, chemicals, and biological samples. The quality of the reconstructed spectrum is highly dependent upon the quality of the derivative spectrum. Therefore, methods that improve the quality of the derivative feature help to better detect and benchmark collected data.

5.1.1 Approaches to Increase Signal-to-Noise Ratio

The most common approach to improve signal-to-noise ratio (SNR) has been to modify experimental parameters. As shown in Equation 3.7, the SNR scales by the square root of the integration time and laser power. Therefore, it is traditional to adjust these parameters to improve the Raman scattering signal. If fluorescence dominates, then transitioning to NIR excitation wavelengths can reduce these effects relative to Raman scattering. From a hardware standpoint, Raman scattering intensity is enhanced by reducing the spot size of the laser on the sample, i.e. condensing the incident laser power in a smaller sample surface area. Thermal considerations (i.e. sample heating) may have to be considered depending on the spot size and type of sample. For example, biological samples or SERS samples may be damaged by too much local heating. Other system components, such as filters and detectors, or even the layout itself can effect the relative intensity of the Raman signature. Signal processing methods for improving the SNR are limited to averaging multiple data sets. This functionality is easily implemented in most systems and scales the SNR by the square root of the number of averages taken.

5.2 Cross-Correlation Method

An alternative approach to the standard processing method described above is through the use of the cross-correlation to obtain the difference spectrum. The cross-correlation is a measure of similarity between two signals. In this mathematical operation, one signal is "swept" across the other to measure the similarity in the signals as a function of relative delay between the two signals. Such methods are commonly used in radar systems to determine the distance and velocity of an object based on the cross-correlation of a pulse sequence and the response reflected from a distant object. Other applications include uses in pattern recognition and surface topography evaluation, among many other examples [61, 62].

A novel implementation of the cross-correlation can be applied to Raman Spectroscopy. As discussed earlier, the Raman response is nearly instantaneous and, therefore, the Raman scattering signature shifts proportionally to the input excitation. The physical meaning of this is a change in amplitude of an individual pixel as the spectrum shifts. A high level example of this is given in Figure 5-3, where the second input, λ_2 is shifted a small amount from the first input, λ_1.

Given that $\lambda_2 > \lambda_1$, there will be a positive correlation when an increase in wave-

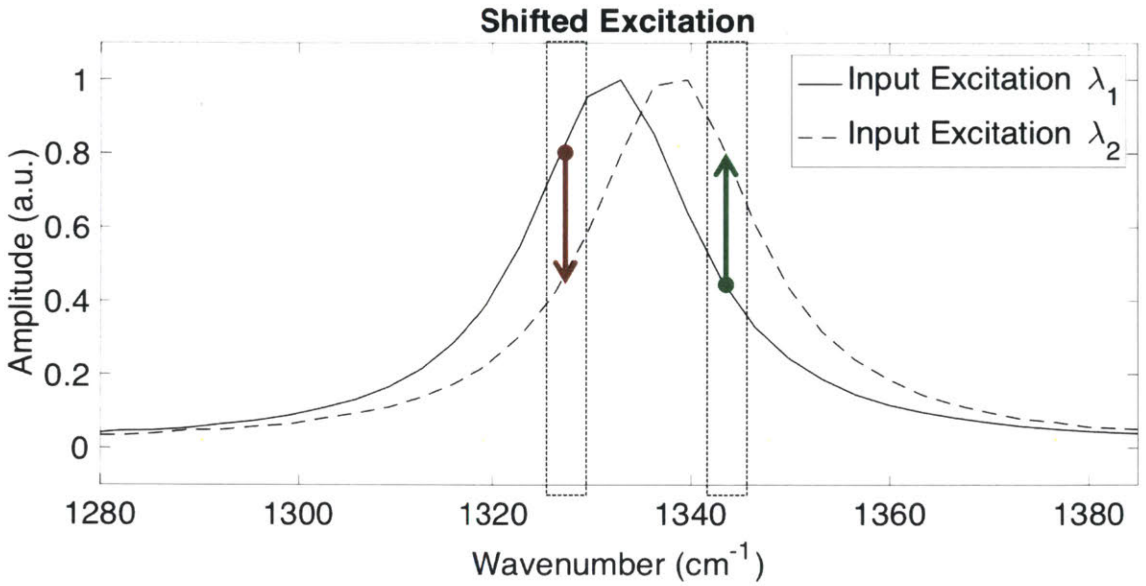

Figure 5-3: Change in pixel amplitude. Positive correlation with the input is shown by the green arrows and negative correlation shown by the red arrows.

length is associated with an increase in amplitude. Correspondingly, there will be a negative correlation when an increase in wavelength is associated with a decrease in amplitude. The positive correlation is shown by a green arrow and the negative correlation is shown in red in Figure 5-3. This assumes that all other aspects of the spectrum remain either constant or uncorrelated to the change in excitation wavelength (i.e. fluorescence and background). A key takeaway from the data is that this result is true for any arbitrary excitation input sequence (sinusoidal, stochastic, etc.). In addition, it will be shown later that the difference spectrum can be obtained by looking at the correlation when there are more than two input excitations. The optical design detailed in Chapter 4 enables rapid changes in input excitation, which allows for more versatility in input excitation waveforms and modulation rates.

The process of obtaining a difference spectrum through the use of cross-correlation can be understood step by step. We can first define a given excitation input sequence, where I is now defined as the input number in the sequence:

$$\lambda_i \equiv I_{\lambda_i} = [I_{\lambda_1} \quad I_{\lambda_2} \quad \dots \quad I_{\lambda_n}]. \tag{5.5}$$

The given input sequence can correspond to any number of waveforms, but the focus

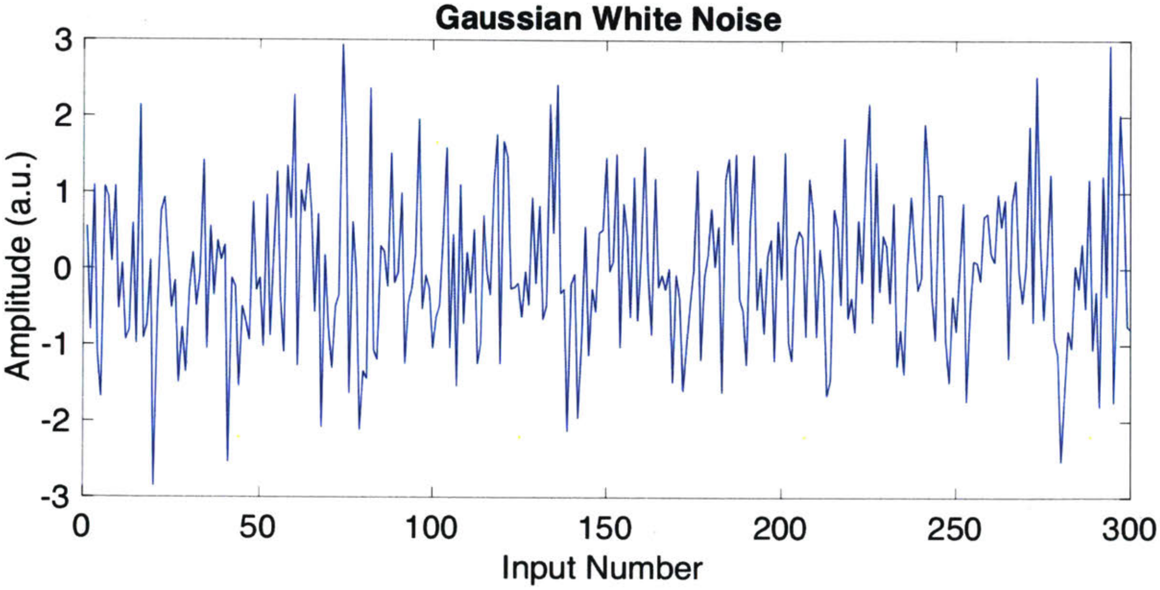

Figure 5-4: Gaussian white noise generated in MatLab.

here is on a binary stochastic input. Modulating stochastically offers several benefits as compared to other implementations. First, the power spectrum of a stochastic input is ideally flat, which means that there is no dominant input frequency, which could be coupled with an external frequency [63]. Second, the stochastic input is ideal for multiplexing FBGs and extracting the corresponding data. To obtain a stochastic input sequence, the Matlab function *randn* was used to generate a random vector with a normal distribution. An example of this is shown in Figure 5-4.

This was then convolved with a first order low pass filter. The filter acts as an attenuator for the high frequency components while maintaining the low frequency components. A threshold was then applied that assigned a value of +1 or -1 based on whether the value of the random number was above or below zero (see Figure 5-5). The choice of 300 "number of inputs" in Figure 5-5 is arbitrary as this number will vary depending on the sample signal and measurement time. More samples will lead to a higher SNR; this will be discussed further in the proceeding section. The value of +1 and -1 will each be assigned an input excitation wavelength. Given the parameters of the FBG and the SLED, this will be centered around 633 nm with a minimum difference of approximately 0.25 nm up to the maximum of 0.6 nm given the limitations of the piezo-actuator between the two assigned values. Each input

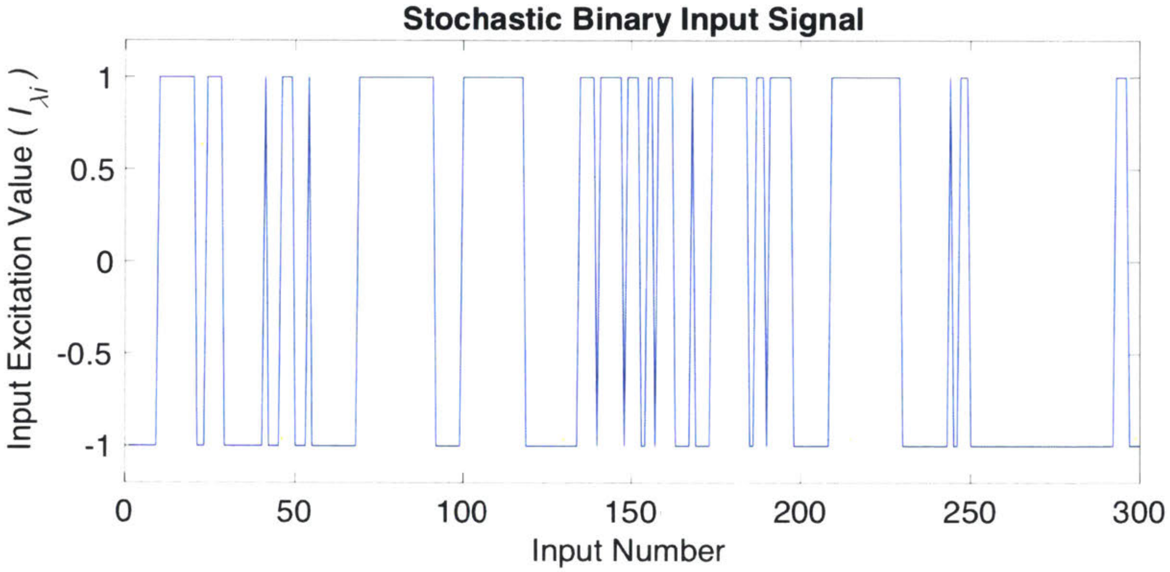

Figure 5-5: Binary stochastic signal produced by convolving Gaussian white noise with a first order low pass filter, where +1 is assigned one Input Excitation Value (I_{λ_1}) and -1 is assigned a shifted Input Excitation Value (I_{λ_2}).

excitation corresponds to an entire spectrum (i.e. detector response). As an example, I_{λ_1} would correspond to a vector containing the spectral response from the CCD. This relationship is shown in Figure 5-6.

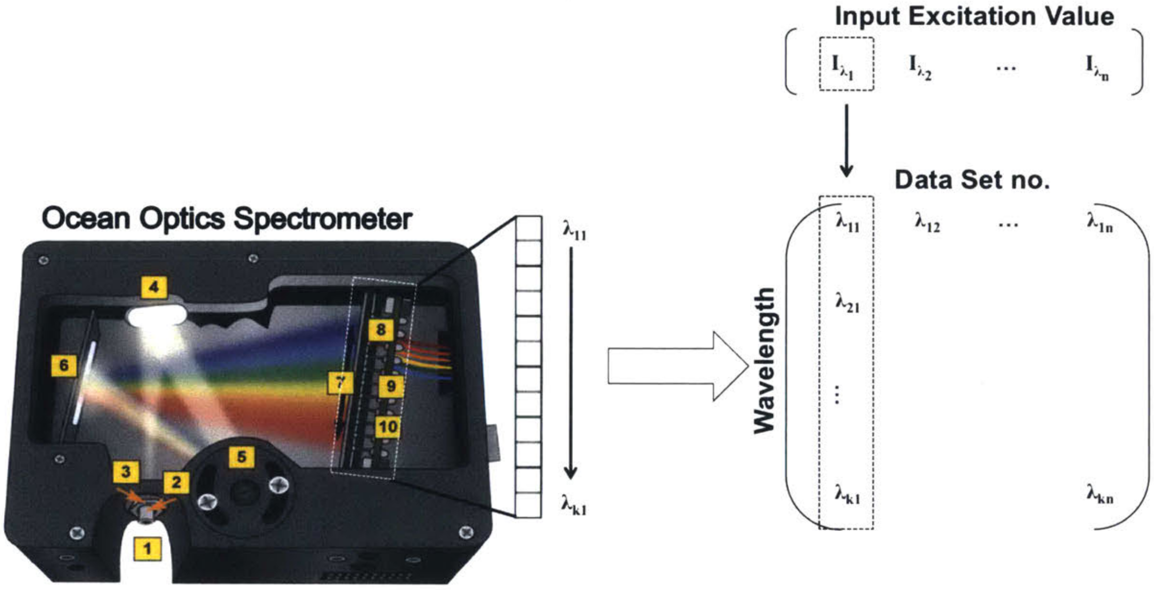

Figure 5-6: A given input excitation I_{λ_i} corresponds to a vector containing the response of each pixel at a particular wavelength.

If a given CCD pixel contains information about the Raman scattering, then the modulation will correlate with the stochastic input. Conversely, if the CCD pixel contains non-Raman scattered photons (i.e. fluorescence, background, etc.), then there will be little to no correlation to the stochastic input for small shifts. As we start to accumulate a large number of data sets we can start to visualize this relationship. The graph in Figure 5-7(a) shows a 3D plot of the data sets as they start to accumulate. The response of an individual pixel to a change in excitation depends on whether the pixel has captured Raman scattered photons as well as the input excitation. In this case, there is a Raman feature located around 1300 cm^{-1}, while the remainder of the peaks are associated with other spectral artifacts. The single Raman feature is shifted when the input excitation shifts. When both spectra are plotted relative to the initial excitation, this shift is visible.

The 300 data sets in this example can be stacked together to form an image as shown in Figure 5-7 (b). The higher amplitudes corresponding to peaks are shown in yellow, while lower amplitudes are blue. In addition, it becomes clear from this image that there is modulation occurring. Relative to the input excitation, we see there is a positive correlation and a negative correlation as shown Figure 5-7(c) and (d).

To quantify this relationship, we can take the cross-correlation between the stochastic input and the response of the pixel. This cross-correlation is given by the equation below for the general case of a continuous function and will be analyzed further in the proceeding section:

$$\phi_k(\tau) = \frac{1}{N-\tau}\int_0^N \lambda_k(n) I_{\lambda_k}(n-\tau)dn, \tag{5.6}$$

where τ represents the "lag" between the input and output. In this case, the lag term corresponds to a shift relative to the previous sample. The cross-correlation output is a matrix whose rows represent a CCD pixel (i.e. wavelength) and whose columns represent the cross-correlation at different lags. N is the total number of measurements, while n represents the measurements number. This process is shown in Figure 5-8, where a new cross-correlation matrix is formed.

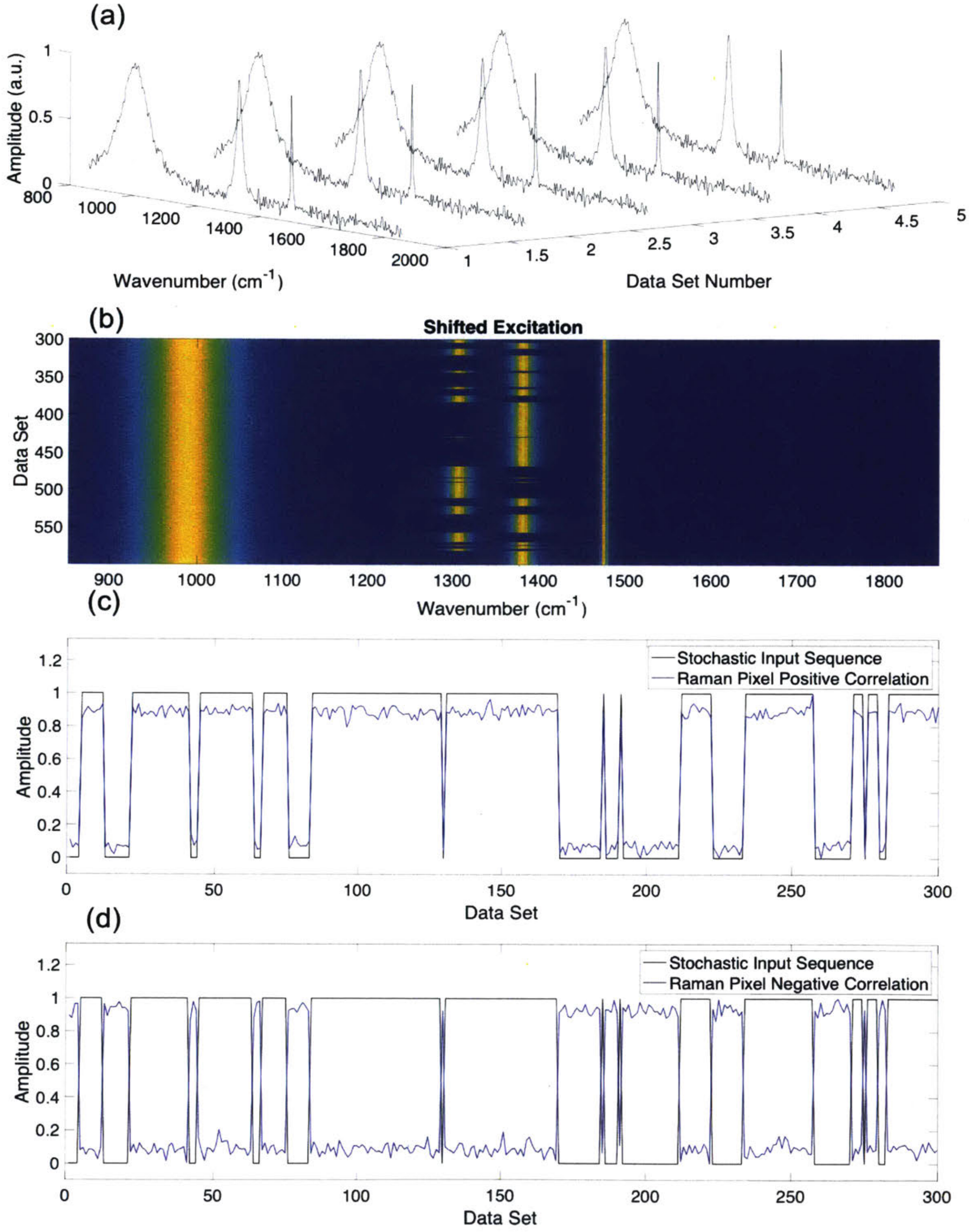

Figure 5-7: Accumulation of data sets with a stochastic input. (a) shows a number of spectra collected using a 3D plot for visualization. (b) shows an "image" of all 300 data sets. (c) and (d) show the positive and negative correlation relative to the input stochastic sequence.

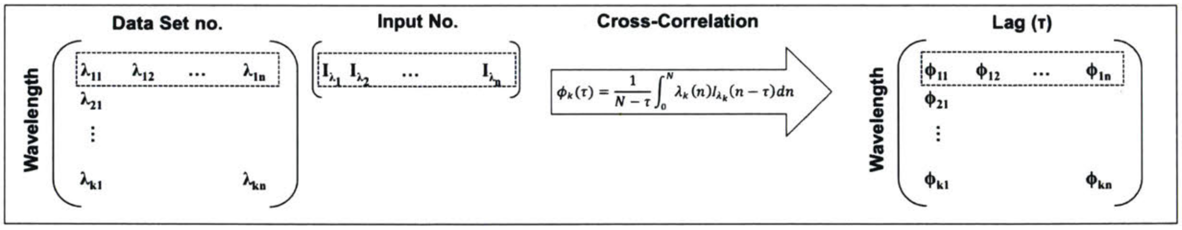

Figure 5-8: Cross-correlation between the input sequence and pixel response is taken to form a new matrix.

We can plot the cross-correlation as a function of lag between two pixels. One of these pixels contains Raman scattering, while the other does not. The results of this are shown in Figure 5-9.

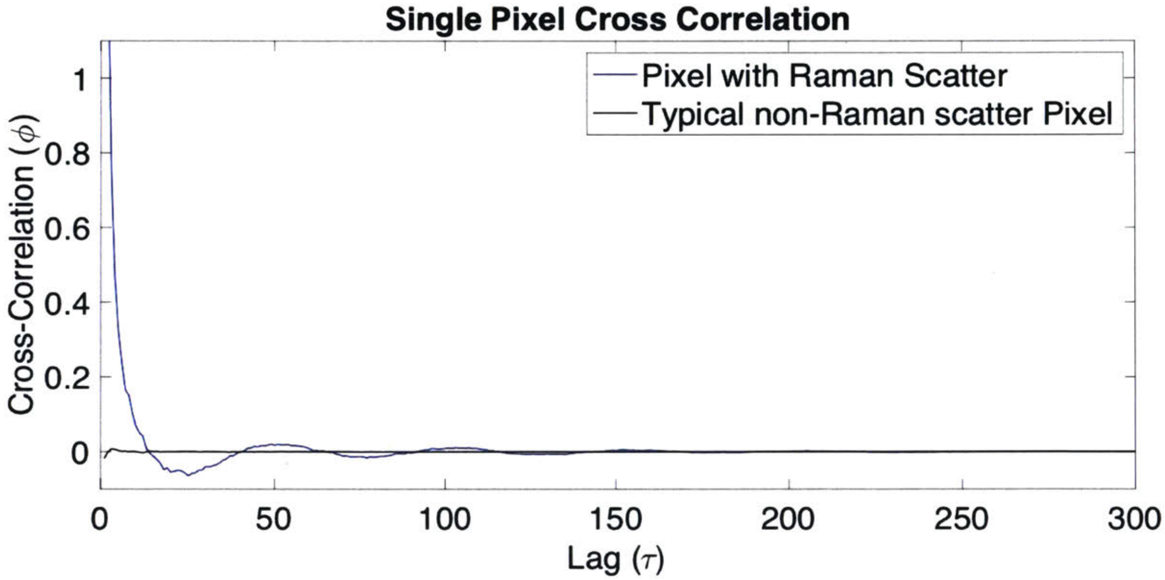

Figure 5-9: Typical cross-correlation of two pixels: one containing a Raman scattering signal (shown in blue) and the other with no Raman scattering (shown in black).

What can be seen is nearly zero correlation for a non-Raman pixel. Yet, there is a high level of correlation in the zero-lag position for a Raman pixel, which corresponds to the nearly instantaneous Raman response. In addition to this, we see some correlation at lag values beyond zero. Despite the fact that the signal is stochastic, there is some redundancy because of its finite length. This effect becomes less noticeable as the input stochastic signal gets longer, but leads to an important result. The variance of the cross-correlated signal across all lags is higher for a Raman pixel as compared to a non-Raman pixel. Therefore, from the cross-correlation matrix, we can deduce two important features. First is the difference spectrum, which is contained in the first column of the matrix (i.e. $\tau = 0$) and second is the variance across each row from $\tau = 2$ until the end of the vector. Figure 5-10 shows the result of this process.

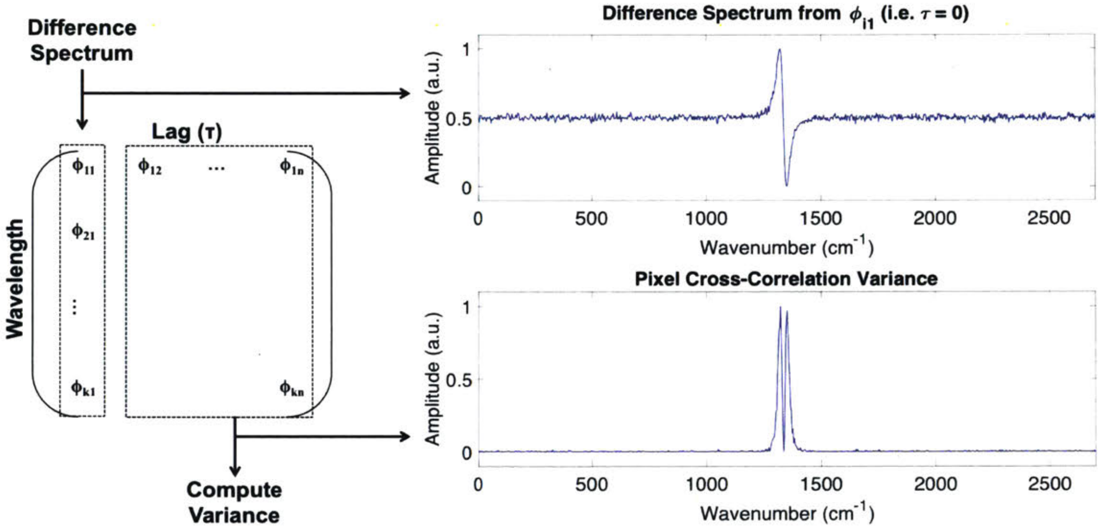

Figure 5-10: Difference spectrum computed from the cross-correlation and the relative variance associated with each pixel.

Importantly, the peak variance coincides with the max and min of the difference spectrum. By multiplying the difference spectrum by the variance the value of non-Raman pixels is driven to near zero, while the derivative feature is enhanced. The result of this operation is shown in Figure 5-11. Scaling of the difference spectrum produces a higher SNR than purely averaging the data sets. Computing the cross-correlation was paramount because it provided this additional useful information.

If scaling was done with the variance of a single pixel prior to cross-correlating, the results would have been significantly different and inaccurately reflective of the derivative feature. The following section will focus on the performance of this technique in relation to the existing method.

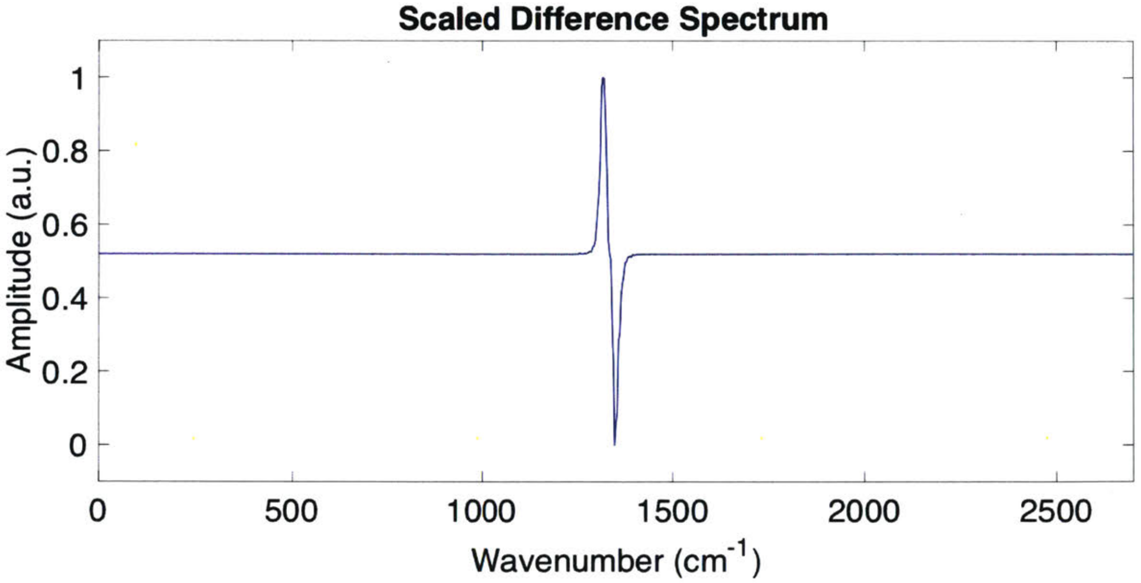

Figure 5-11: Scaled difference spectrum.

5.3 Performance Simulations

5.3.1 Approach

To evaluate and compare the performance of the modulation technique outlined in the previous section to the standard subtraction approach, an artificial Raman spectrum was generated in Matlab. Raman scattering was modeled using a Lorentzian function as shown in Equation 5.7, which can accurately describe the shape of the band given the grating parameters in the spectrometer as described by Mosier-Boss et. al. [64],

$$L(x) = \frac{0.5\pi\Gamma}{(x - x_o)^2 + (0.5\Gamma)^2}, \tag{5.7}$$

where Γ is the width of the function and x_o is the center position on the axis. Gaussian white noise was added to the spectrum and, in some cases, broadband fluorescence was modeled using a polynomial function that was added to the data set. The simulation was set up to test varying cases that included situations, where the fluorescence spectrum was changing, but decayed at a certain rate. The same diamond sample with a characteristic shift at 1332 cm^{-1} was simulated as shown in Figure 5-12.

Notably, the simulated resolution matched that of the QE Pro spectrometer used

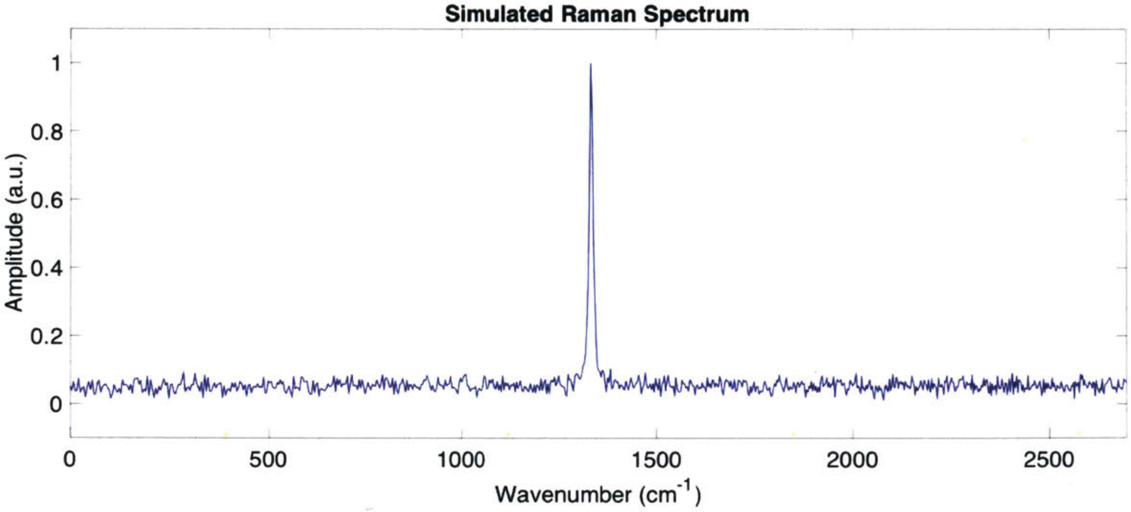

Figure 5-12: Simulated Raman spectrum.

in the existing setup. This ensured relevant and accurate simulations relative to the existing system. Results are shown in proceeding sections where the conventional method is compared to the methods developed in this thesis work.

5.3.2 Comparison to Conventional Methods

In order to understand the advantages of this new signal processing approach for Raman Spectroscopy, it is important to review the key assumptions made in shifted excitation techniques. As mentioned earlier, the conventional approach to data processing has been subtraction of data sets. One measurement is conducted at one excitation, which contains a combination of Raman scattering, fluorescence, and background artifacts. A second measurement is taken at another excitation source. Subtraction of the two data sets leaves only features that resemble the derivative of the Raman signal. The two key assumptions for this method are described below:

1. Kasha's rules applies: This means that small shifts in excitation leave the fluorescence spectrum unchanged.

2. The input excitation shift is reliable and can be accurately predicted: Any deviation from the two-excitation states in the traditional method will degrade the quality of the output once the spectrum is subtracted. This may be a small

problem when working in a controlled environment, but for a compact system in the field subject to harsh conditions it may be more complicated.

Signal-to-Noise Ratio

Assuming that the conditions described above are met, then any variations in the pixel response are governed by Poisson statics. As an approximation, this is modeled as Gaussian white noise in MatLab. The variance (σ^2) between adjacent pixels was used as a metric to define the noise. Since reconstruction of the original signal from the difference spectrum was required, the relationship between adjacent pixels becomes significant; this was the motivation for defining the noise using this method. An increasing number of data sets was averaged, and the relationship between the variance and number of data sets is shown in Figure 5-13.

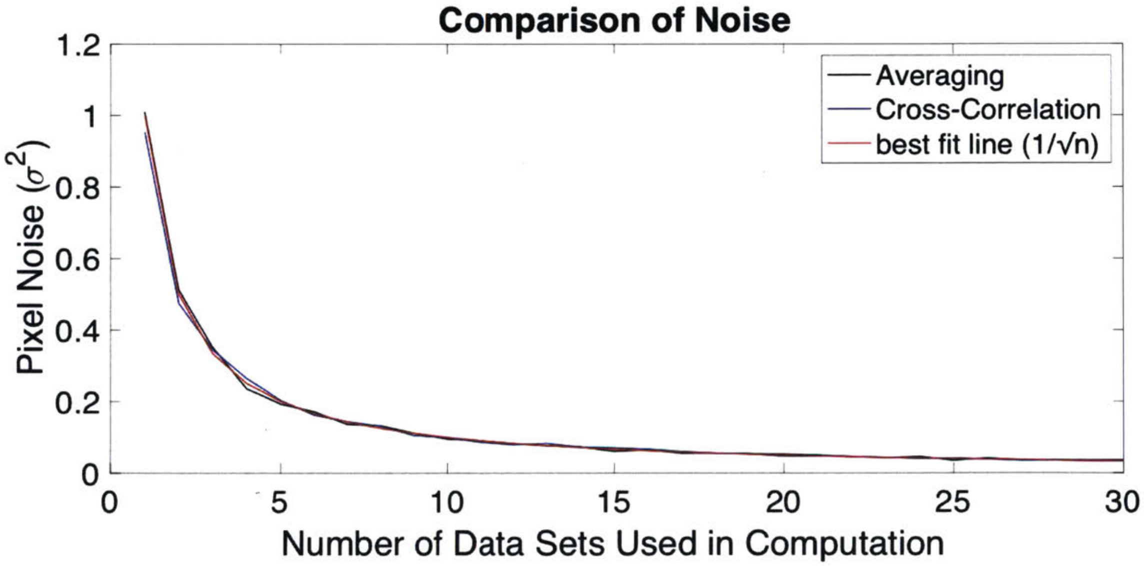

Figure 5-13: Comparison showing pixel noise as a function of samples using averaging and the cross-correlation ϕ_{i1} at $\tau = 0$.

As expected, the noise is decreasing by a factor of $\frac{1}{\sqrt{N}}$, where N is the number of data sets used in the computation. Assuming that the signal stays constant, then the SNR will increase by a factor of $\sqrt{N}$. This method was then compared to the difference spectrum obtained by the cross-correlation at $\tau = 0$ (without scaling). The result of this is also shown in Figure 5-13 and also scales by $\frac{1}{\sqrt{N}}$. Therefore, SNR is equivalent in both methods before scaling is applied. In fact, this is the expected relationship if we look more closely at the cross correlation for $\tau = 0$:

$$\phi_k(\tau = 0) = \frac{1}{N} \int_0^N \lambda_k(n) I_{\lambda_k}(n) dn. \tag{5.8}$$

Since the signal we are obtaining is discrete, we can replace the integral function with a summation, which is,

$$\phi_k(\tau = 0) = \frac{1}{N} \sum_{n=1}^{N} \lambda_k(n) I_{\lambda_k}(n). \tag{5.9}$$

The $I_{\lambda_k}(n)$ term is binary stochastic between -1 and +1. We can assume that there is an equal number of both conditions, which is a reasonable approximation as the input signal grows in length. The terms can now be grouped based on their sign, resulting in,

$$\phi_k(\tau = 0) = \frac{1}{N/2} \sum_{n=1}^{N/2} \lambda_k(n) I_{\lambda_k}(n) - \frac{1}{N/2} \sum_{m=1}^{N/2} \lambda_k(m) I_{\lambda_k}(m), \tag{5.10}$$

where n is associated with input values ($I_{\lambda_k}(n)$) of +1 and m is associated with input values of -1. The result obtained above is, in fact, the same equation as independently averaging values from one wavelength and subtracting it from the average of a shifted wavelength. Although this turns out to be computationally equivalent for two inputs, this technique can be used for more than two input excitations. Going further, the cross-correlation matrix contains additional information that can be utilized. This information is used to scale the difference spectrum. Simulating the variance across each pixel for scaling can be complicated since it varies depending on the binary input sequence, which is stochastic. Yet, as an order of magnitude estimate, the SNR improvement factor once the spectrum is scaled is shown in Figure 5-14. For example, if the initial SNR is estimated to be 10, then scaling will increase this relative SNR by 2 orders of magnitude compared to traditional methods. The limit to this effect is that the SNR for a single pixel that contains Raman scatter needs to be above the noise threshold (i.e. SNR>1), otherwise there will not be a significant correlation. It

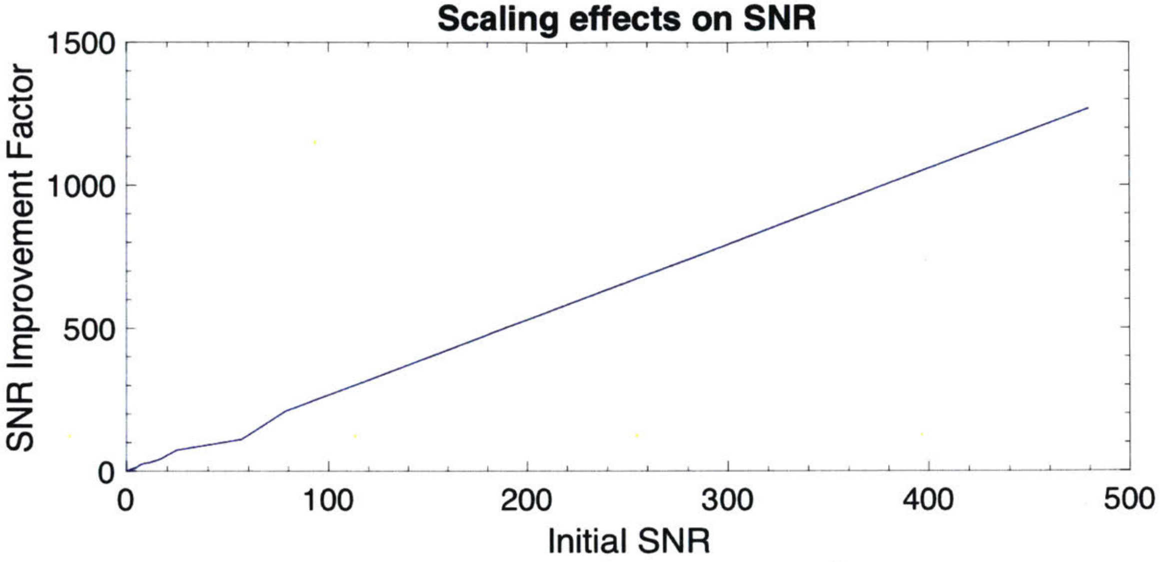

Figure 5-14: Scaling effects on the signal-to-noise ratio.

is important to note here that the SNR of a single pixel is fundamentally different than the relative SNR across all pixels (i.e. the spectrum); the latter becomes important for reconstructing the original spectrum.

Robustness

In the traditional approach, any deviation in excitation wavelength or environmental effects that may slightly shift the excitation wavelength will disrupt the measurement. This data is either removed as an outlier or simply averaged into the existing data set, leading to more noise in the spectrum and potentially a false detection. The system developed as part of this research allows for indirect continuous monitoring of the spectrum through the filtered portion of the spectrum that passes through the FBG. This is significant because correlation methods can be used to compute the difference spectrum as long as the input excitation is known. In fact, the difference spectrum can be obtained from any arbitrary number of shifts as long as the shift is less than the width of the Raman features. Rather than cross-correlating the pixel with a binary stochastic input, the cross-correlation can be done with a ternary stochastic input or quaternary stochastic input for 3 or 4 input excitations, respectively. An example of a ternary stochastic input is shown in Figure 5-15.

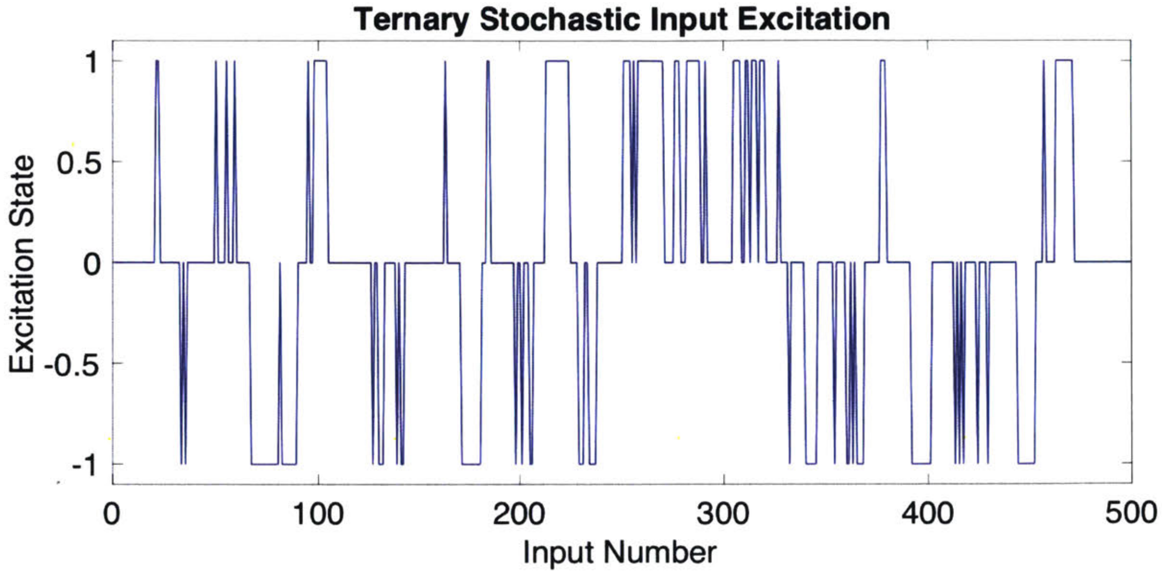

Figure 5-15: Ternary stochastic input.

Figure 5-16 shows the result of using the cross-correlation method to compute the difference spectrum for 2, 3, and 4 input excitations. The relative shift between each excitation input remained constant in this example, but that does not have to be the case. Therefore, it is reasonable to assume that monitoring the input excitation would result in improved statistics compared to conventional methods (i.e. a more robust method of computing the difference spectrum). The three difference spectra shown in Figure 5-16 are now overlaid in Figure 5-17, which shows the nearly identical spectrum.

Time-Dependent Features

Variable excitation techniques have traditionally been applied in the NIR, where small changes in excitations have little effect on the fluorescence spectrum. Yet, there is motivation to reduce the input excitation wavelength as the Raman scattering scales by λ^{-4}. These shorter wavelengths will have a greater impact on the fluorescence spectrum for a given shift, thus violating "Kasha's rule" as applied to shifted excitation techniques in Raman spectroscopy. The data processing method outlined in this work has the added benefit that it can essentially mask out any effects that are delayed in time, such as changes in fluorescence. If the modulation occurs at a frequency faster

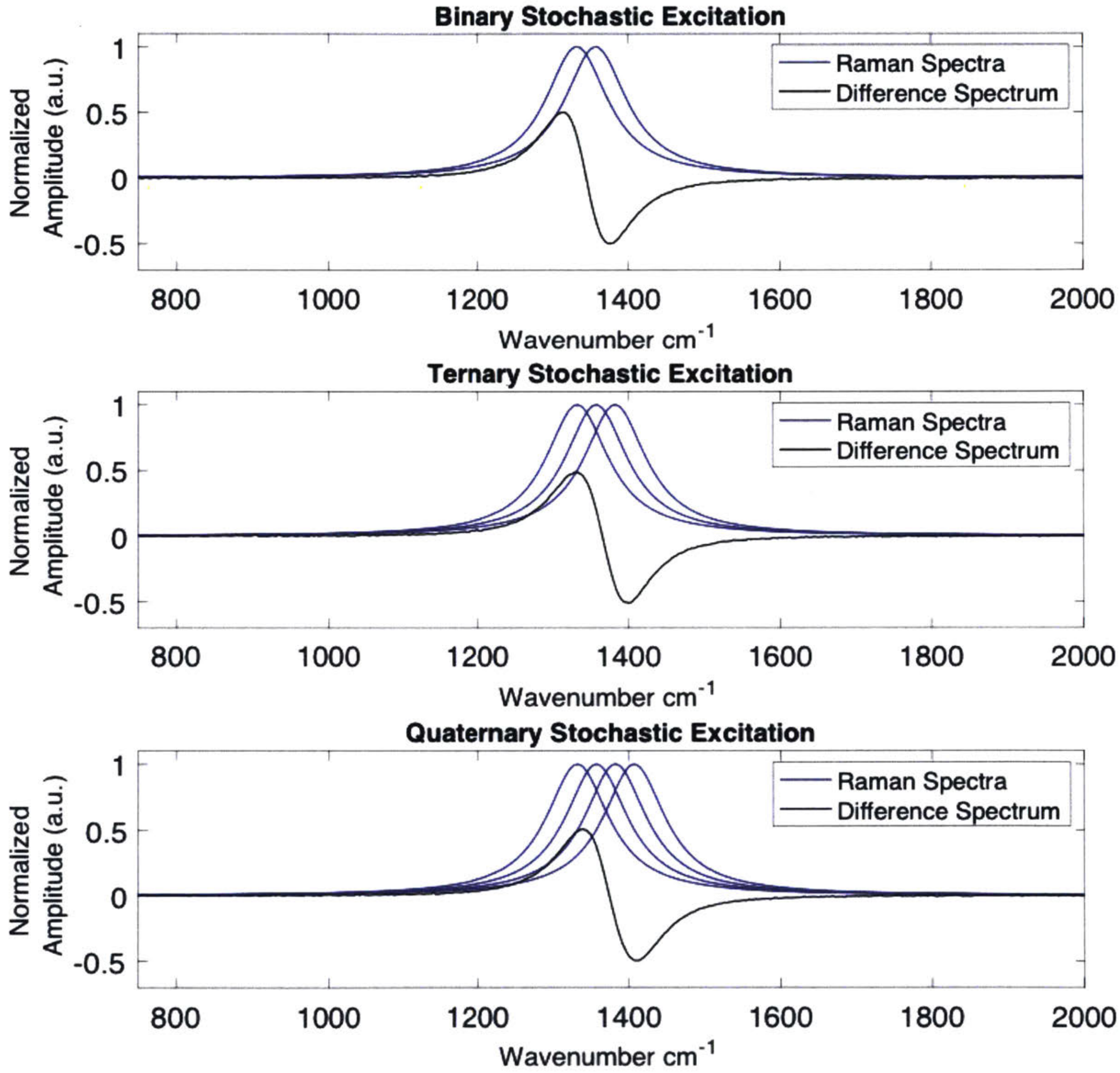

Figure 5-16: Derivative spectrum obtained through 2, 3, and 4 excitations that were correspondingly cross-correlated with the input excitation sequence.

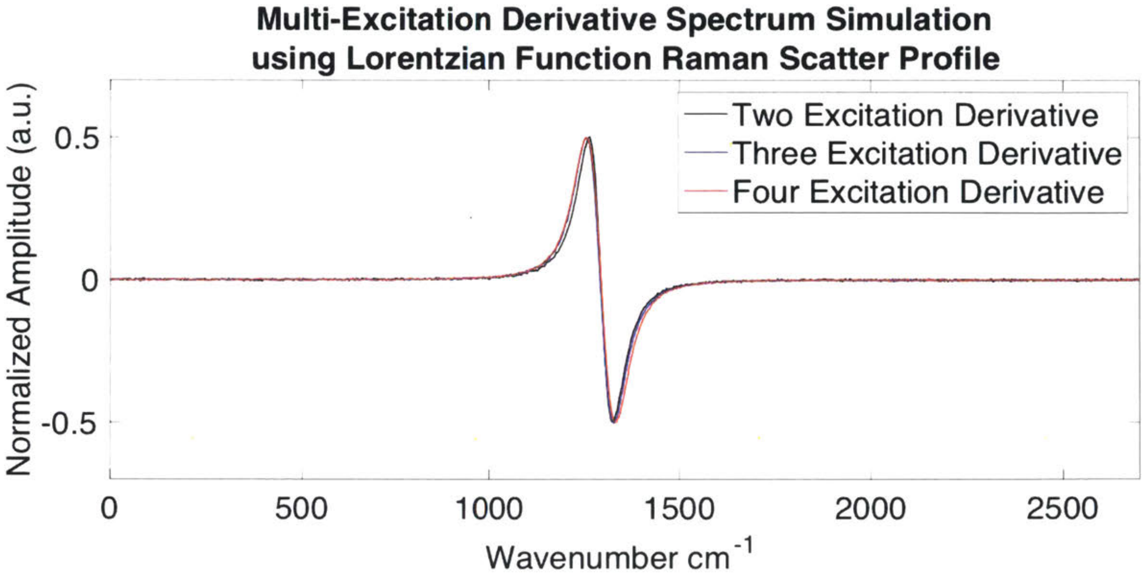

Figure 5-17: Overlay of the difference spectrum computed from 2, 3, and 4, input excitations.

than the fluorescence excitation or decay then there will be little correlation, which will effectively mask its effects. For relatively high laser powers at short wavelengths (i.e. <600 nm), it may be possible to modulate faster than fluorescence lifetimes that are on the order of hundreds of milliseconds or longer. Longer effects such as phosphorescence could also be decoupled.

As an example, Figure 5-18 shows a binary stochastic input where the input sequence changes faster than the fluorescence decay time. The dark line in the top graph of Figure 5-18 represents the stochastic input, while the blue line represents the time-dependent changing fluorescence with a characteristic decay. Although it is not shown, the Raman spectrum would respond proportionally to the input sequence. In the traditional approach, the system is required to stabilize at each input excitation wavelength independently before measurements are made. This forces the data set to maintain any changes in fluorescence and makes it impractical for applications in shorter wavelength (higher energy) variable excitation Raman systems. The middle graph in Figure 5-18 shows how the spectrum is completely saturated by the fluorescence. Applying the cross-correlation and scaling the data by the variance as discussed in the previous sections shows the sharp derivative feature associated with the Raman scattering signal.

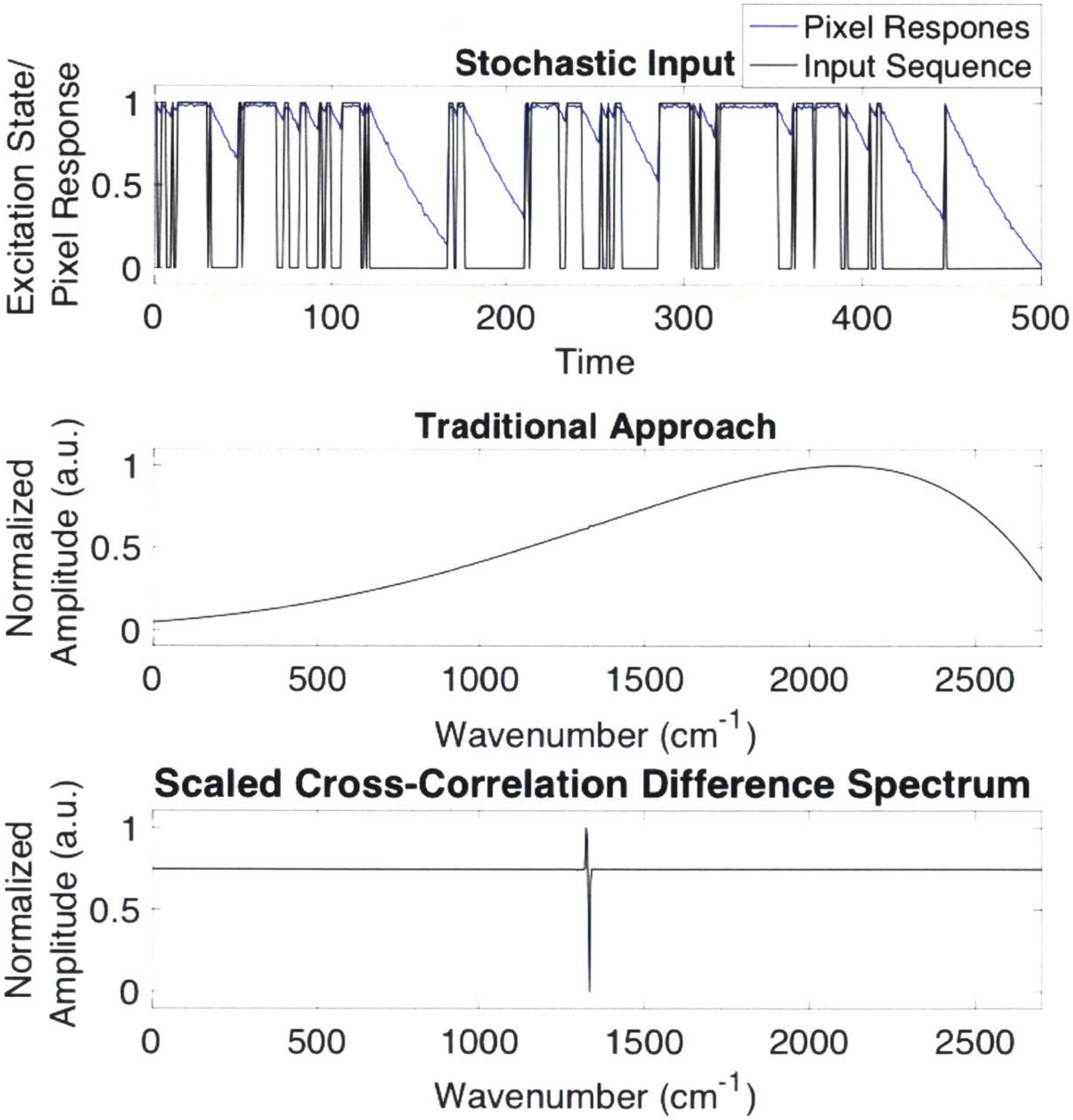

Figure 5-18: Comparison of techniques for obtaining a derivative spectrum when the fluorescence spectrum varies with the input excitation.

In summary, this new approach to modulating and applying the data offers several major advantages over traditional techniques. These advantages range from improved SNR to more versatility. Ultimately, this method will help to reduce the false detection rate, which is one of the main goals of this research.

5.4 Experimental Implementation

The theoretical framework described above needed to be tested experimentally. In order to do this, the temperature-controlled laser diode described in Section 4.3 was used prior to implementing the fully functioning system. The system was modulated by approximately 0.25 nm stochastically. Prior to each measurement, it was ensured that the laser diode was stabilized to minimize any fluctuations in the laser excitation wavelength. The sample used was again diamond with a strong characteristic peak located at 1332 cm^{-1}. Two sets of tests were run: The first was with a relatively high SNR with a strong Raman scattering peak and the second test was a lower SNR signal under noisier conditions. For demonstration purposes, the low SNR test data is shown below, since it represents the worst case with the highest chance of false detection. Figure 5-19 shows the raw spectrum with a number of different features.

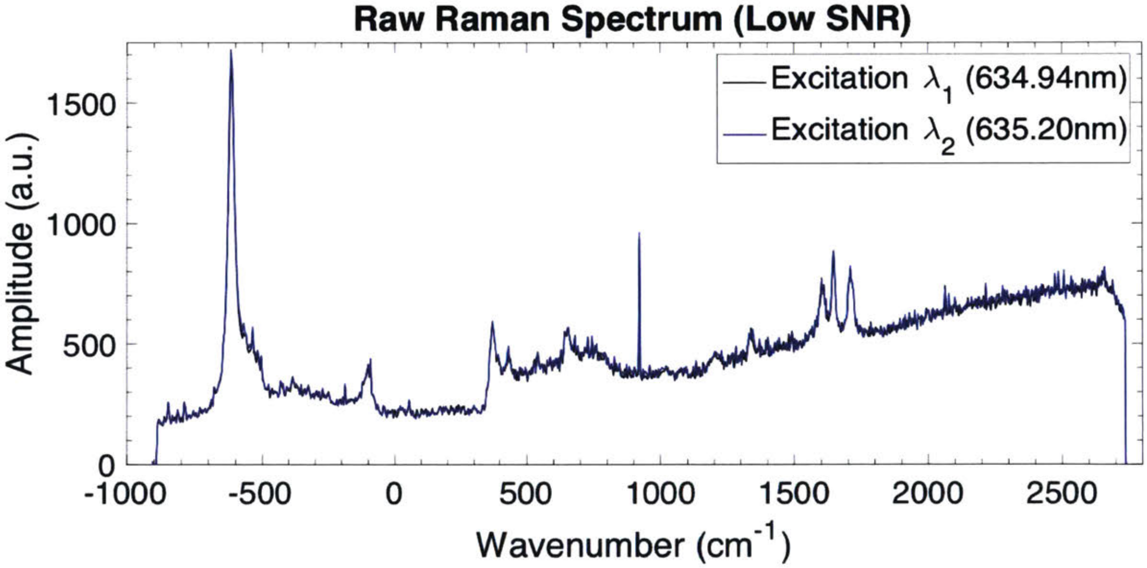

Figure 5-19: Raw spectrum showing a number of different features with the Raman scattering associated with diamond embedded in the signal.

Conventionally, the peaks in Figure 5-19 would lead to false detections since they resemble Raman spectra. Yet, they are unrelated to Raman scattering. The large peaks below 0 cm^{-1}, which is the relative laser excitation input, are associated with background light from the room. The same is true for the triple peak around 1650 cm^{-1}. A sharp cutoff can be seen around 350 cm^{-1}, which is associated with the long-pass filter used to block laser light. Finally, the tall sharp feature around 900 cm^{-1} is due to a pixel with high dark noise. Low frequency broadband fluorescence can be seen along with electronic noise contributing to a DC offset. Figure 5-20(top) shows a comparison of the signal processed using the traditional method of obtaining a difference spectrum and Figure 5-20 (bottom) shows the scaled cross-correlation difference spectrum.

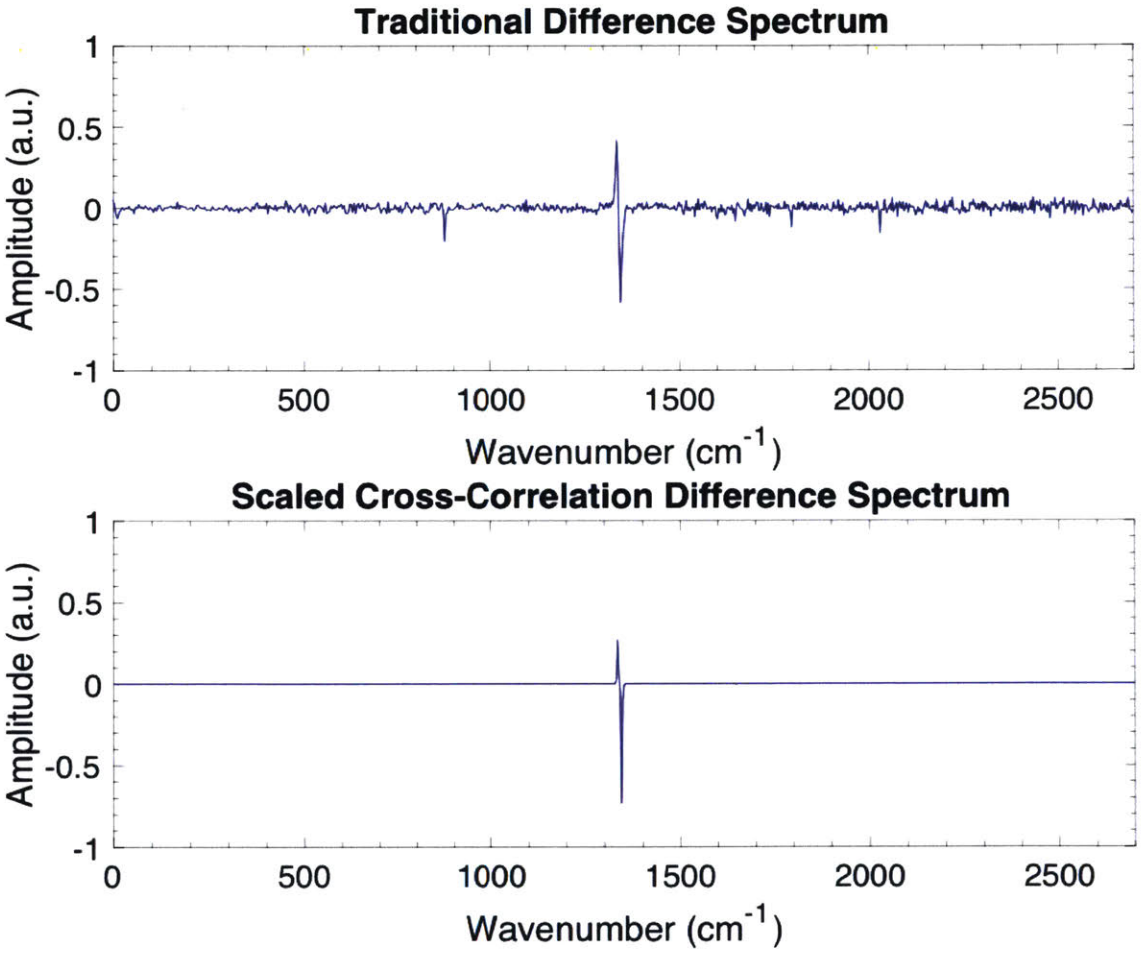

Figure 5-20: Difference spectrum computed using the conventional technique (top) and scaled cross-correlation (bottom).

It's clear that the small spectral features apparent in the traditional technique, which could lead to a false detection, are no longer visible in the scaled cross-correlation. In fact, the result closely resembles the simulations from the Section 5.3. Therefore, this technique was able to successful isolate Raman scattering signal, while driving the features not associated with Raman scattering to zero. Proving this out experimentally verifies both the technique and the assumptions of the simulation.

The final step is to recover the original spectrum. In order to achieve this, the integral of the difference spectrum is taken. This is also done for both the traditional method and the scaled cross-correlation method for comparison. As previously mentioned, the higher quality difference spectrum results in a higher quality reconstructed spectrum. Figure 5-21 shows the reconstructed spectrum for each method.

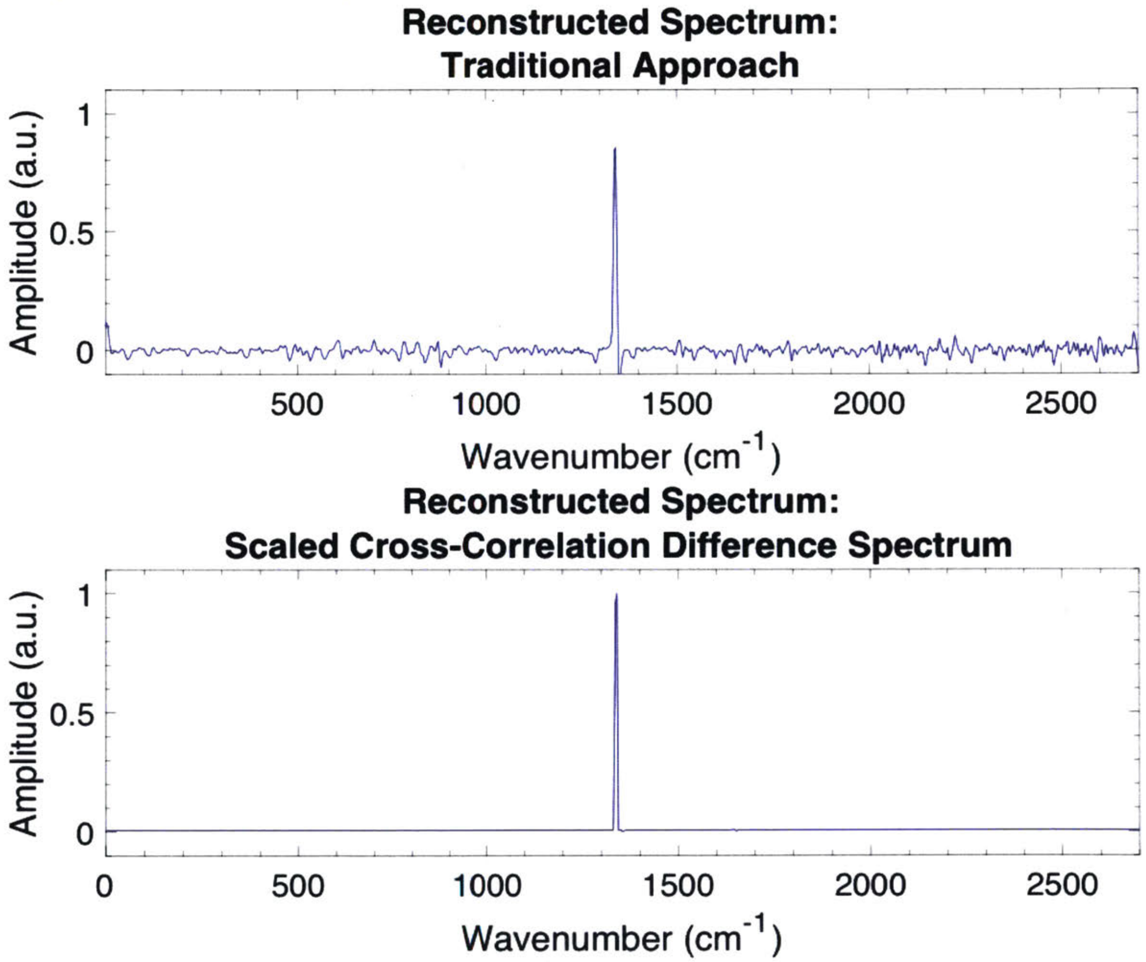

Figure 5-21: Reconstructed spectrum computed using the conventional technique (top) and scaled cross-correlation (bottom).

With the signal processing approach evaluated computationally and verified experimentally, the next step is to combine the functionality of the novel system outlined in the previous chapters with the signal collection and processing outlined here.

Chapter 6 will discuss the testing and evaluation of the entire system as well as its implementation in SERS systems.

THIS PAGE INTENTIONALLY LEFT BLANK

Chapter 6

Testing and Evaluation

The developments in both hardware and signal processing outlined in the previous chapters will be tested and evaluated in the proceeding section. It will start with a discussion on integrating and synchronizing all the system components. Then it will discuss the application of shifted excitation techniques in SERS and show preliminary results indicating its feasibility.

6.1 System Integration

The final hardware system setup is shown in Figure 6-1 with all the components integrated. The SLED was collimated using an objective lens and a combination of tip/tilt stages. The collimated light source was aligned into a single-mode fiber using two mirrors. Then, the single-mode fiber was connected to the input port of the optical circulator. The circulator output (i.e. the second port) was connected to the FBG. The FBG reflects a narrow portion of the beam, which reenters the optical circulator through the second port, and exits through a third port. The third port of the optical circulator was connected to a collimating lens, which collimates the narrow reflected beam to a diameter of approximately 2.8 mm. The beam was reflected off the dichroic beam splitter into an objective lens that has a matching entrance diameter. A sample placed at the working distance of 6 mm from the lens was illuminated and backscattered light was collected. The backscattered light contained both Rayleigh

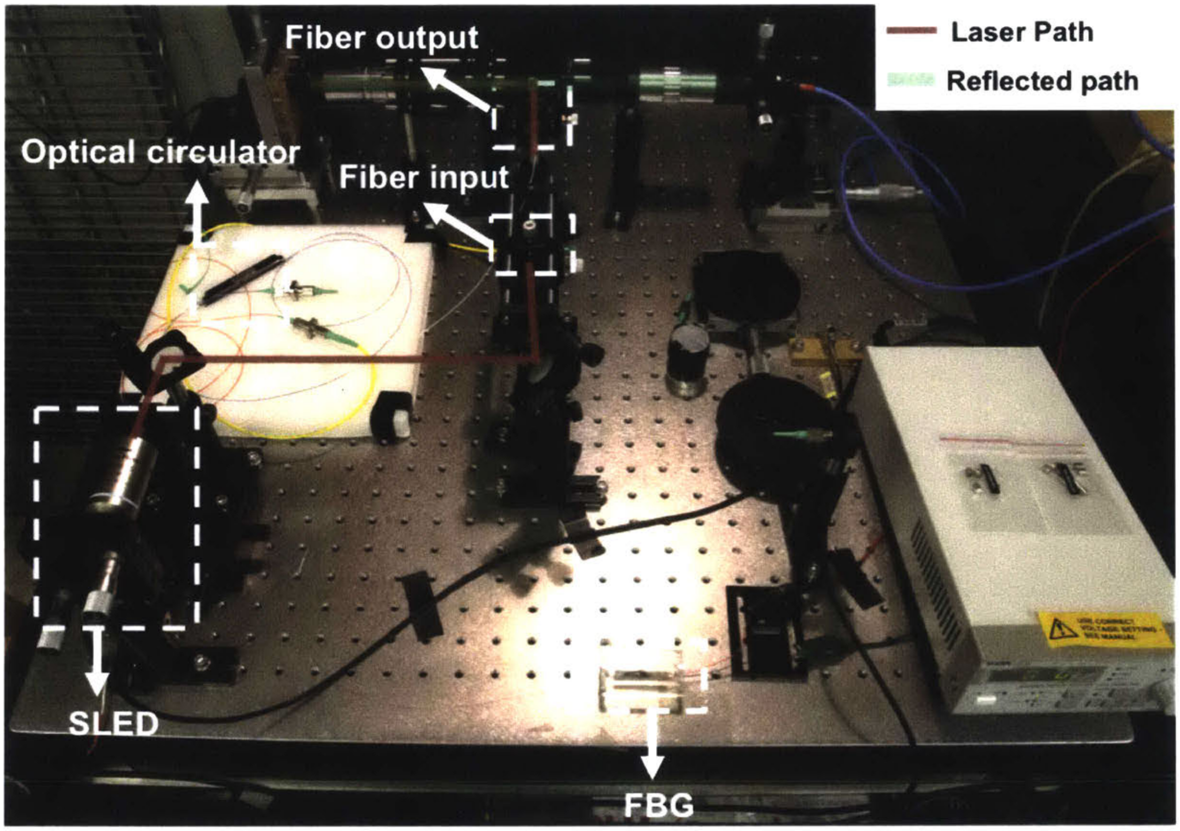

Figure 6-1: Final hardware configuration with all novel elements integrated.

and Raman scattered photons. A small portion of the Rayleigh scattered photons were filtered through the dichroic and the remainder were filtered through the long-pass filter following the dichroic. Conversely, the wavelength-shifted Raman scattered light passed through the dichroic and the long-pass filter and was focused onto a multimode fiber core of about $50\,\mu m$. The fiber was connected to the spectrometer for analysis.

Some additional features of the testbed are important to note. First, the mechanical fiber stretcher is still intact in Figure 6-1. Second, the output of the FBG was connected to a power meter. This can be better seen in Figure 6-2, where the system was operational and the light loss through the fibers is visible. The portion of the beam that is not reflected, but rather filtered through the FBG was constantly monitored. This provided an opportunity to ensure the following: (1) The SLED was stable, meaning that the fluctuations in power were minimal and (2) that the alignment was maintained by observing any large dips or drift in the power over time.

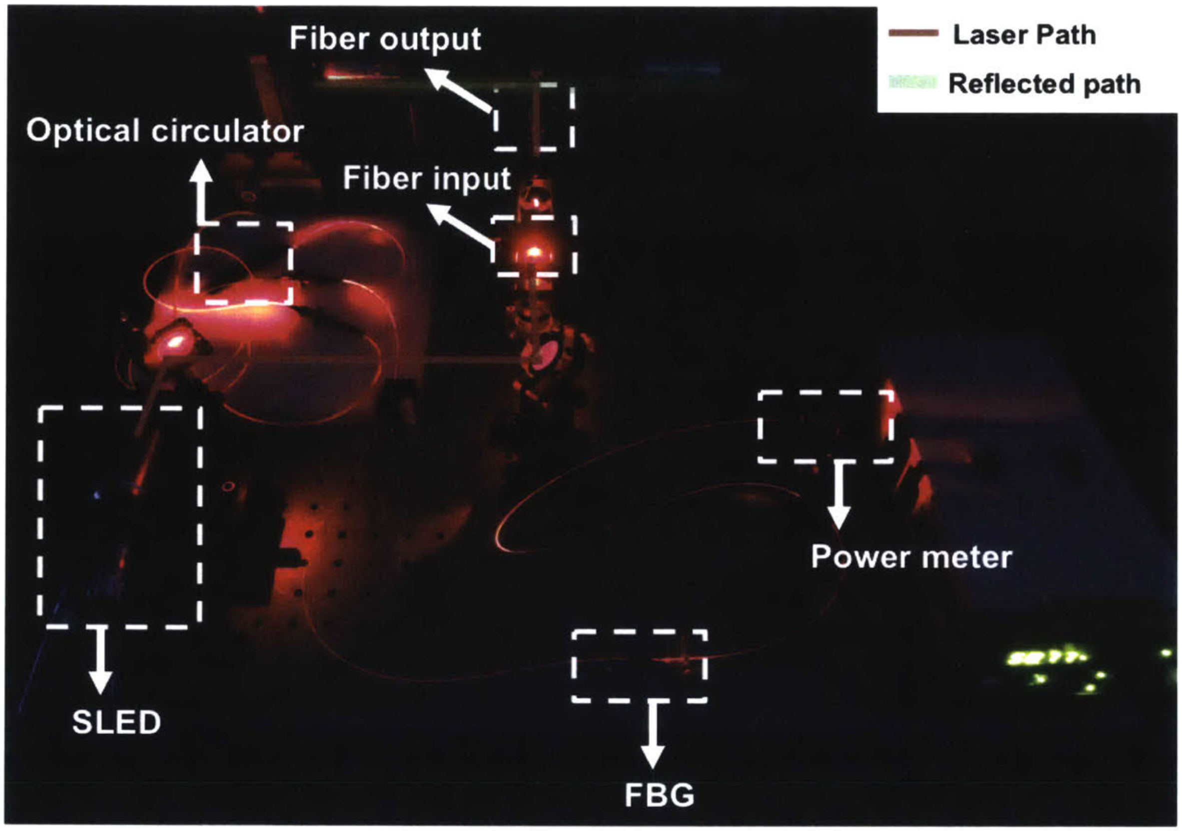

Figure 6-2: Final hardware configuration image taken under low light conditions to visualize the fiber optic paths.

The system was stabilized prior to each test.

Although the light loss appears significant through the fibers in Figure 6-2, this was minimal compared to the losses through low coupling efficiency. To reiterate, the achieved coupling efficiency was approximately 35%. As a result, the main limitation in this current setup is the total amount of power delivered to the sample, which was on the order of a fraction of a mW. Yet, this is particularly well suited for experiments using SERS devices as shown in the following sections.

6.2 Testing Synchronization

A key component of the signal processing methodology outlined previously is the accurate synchronization of all components. In order to achieve this, a combination of a waveform generator, multi-channel power supply, and triggering functionality in

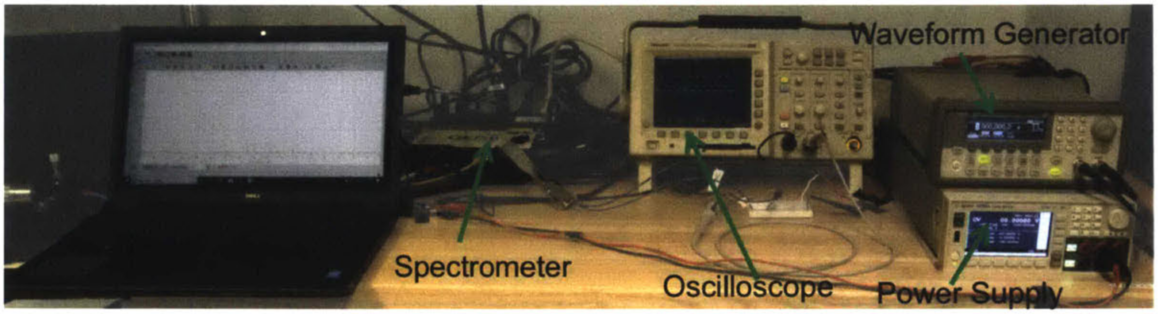

Figure 6-3: Components used to synchronization all elements of the system.

the spectrometer were utilized. These components of the system are shown in Figure 6-3.

The waveform generator was programmed with an arbitrary waveform. This arbitrary waveform represents the stochastic input that was generated in MatLab using methods described previously. The integration time could be adjusted and the points on the waveform are redistributed accordingly, which makes the setup versatile to the sample requirements. The output from the waveform generator was connected to several I/O ports of the D-Sub connector on the back of the power supply. This enabled external triggering on the power supply. One channel from the power supply was connected to the piezo and output either 100 V or 0 V depending on the state of the waveform generator. Conversely, the second channel output a 3.3 V continuously synchronized pulse to the spectrometer I/O port. The spectrometer functionality was somewhat limited in terms of the response to an external pulse. Once it received a trigger pulse, the spectrometer would start an integration process that lasted a duration set by the software. As long as the 3.3 V was supplied, the data acquisition was continuous. A block diagram shown in Figure 6-4 outlines this process, where the integrated elements are shown from left to right. An oscilloscope was used to monitor each channel.

The pulse sequence is shown in more detail in Figure 6-5. At the start of the process, a synchronized 5 V pulse was sent from the waveform generator to the power supply. The initial impulse sent 100 V to the piezo-actuator through channel 1 of the power supply. The duration of the pulse was set by the power supply to match the

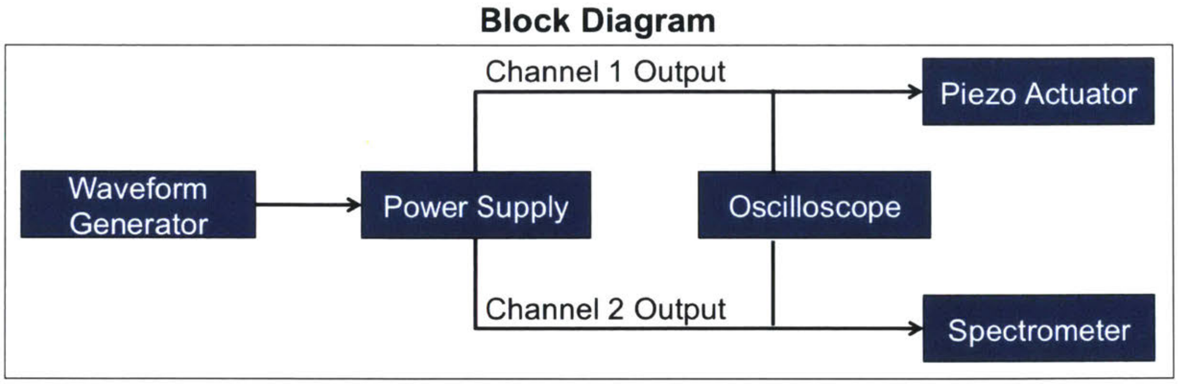

Figure 6-4: Block diagram showing how all the elements are integrated.

integration time of the spectrometer. At the same time, channel 2 outputs a continuous 3.3 V to the spectrometer for continuous data acquisition at a given integration time. The total duration of the 3.3 V pulse was set to be the entire length of the testing sequence (i.e. total number of samples multiplied by the integration time).

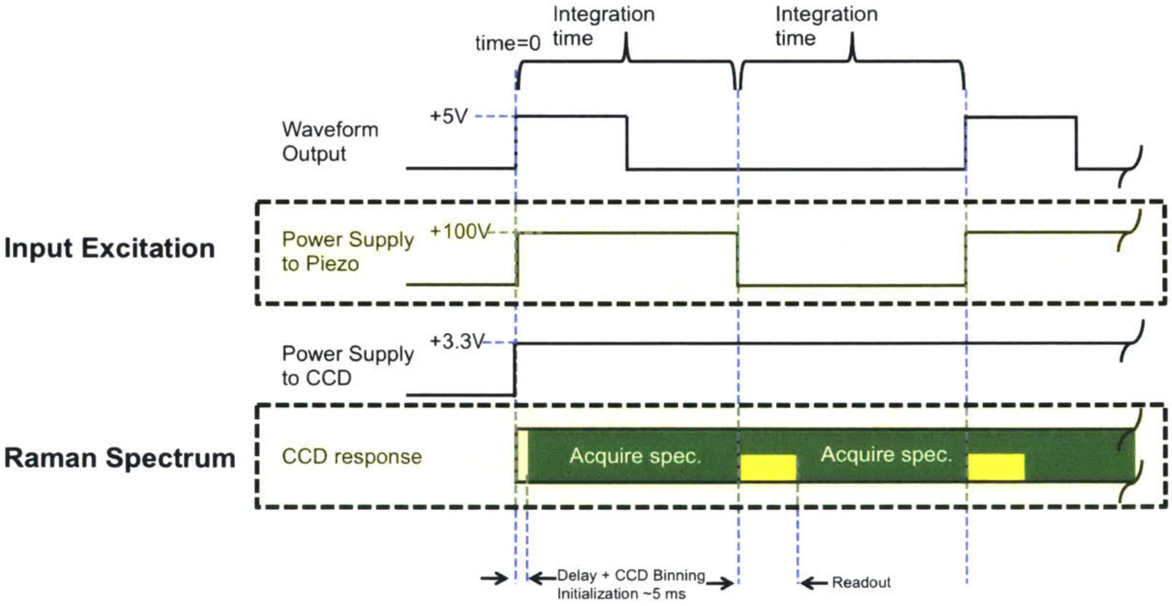

Figure 6-5: Timing/Synchronization of each element in the system.

The response of the spectrometer CCD, when a pulse was received, was slightly more complicated. There was a delay in detector response due to a "binning initialization" that accumulated to about 5ms. Relative to the length of a single acquisition, which ranges from 2 to 3 orders of magnitude longer than this, the delay in synchronization was nearly negligible and was overlooked rather than compensated for in the power supply response. The readout time occurred during the start of the following acquisition. The total readout time for this particular detector was less than 5 ms. Therefore, there was some overlap that caused the readout to contain information from the newly acquired spectrum. However, after review of the relative readout time compared to the total length of the acquired signal, this again becomes negligible.

With all elements of the system integrated and synchronized, it was now possible to test the functionality. In the current configuration, the laser power at the sample is limited by the SLED device and the FWHM of the reflected beam from the FBG. To obtain a stronger Raman signal, the system was applied to a sample absorbed on a SERS substrate. This provided an opportunity to test both the functionality of the existing system and the opportunity to show that shifted excitation techniques can be used on SERS substrates.

6.3 Application to Surface Enhanced Raman Spectroscopy (SERS)

The fundamental concepts of SERS devices are described in Section 2.3. Enhancements in Raman scattering can occur when an analyte is absorbed onto a metal nanostructure. Importantly, shifted excitation techniques can address several existing challenges associated with SERS substrates, which are outlined below:

1. Fluorescence: In both SERS and standard Raman systems, the fluorescence spectrum is an issue. In SERS, the fluorescence spectrum can be enhanced along with the Raman scatter. This is seen in the experimental data collected in the following section.

2. Background: The common sources of background in standard Raman systems are ambient environmental light leakage or pixel dark noise from the detector.

Yet, with SERS devices, there is a "background matrix" or "continuum" from the substrate itself that adds to signal.

3. Signal Fluctuations: In the case of standard Raman systems, these fluctuations are caused by the sensitivity of the system to contamination and the relatively weak scatter compared to other phenomenology. SERS devices have fluctuations caused by complex coupling of surface plasmons to create local hotspots, which can lead to potential fluctuations in the Raman signal.

Applying shifted excitation techniques has the potential to address these issues. Yet, there is some uncertainty that the shifted excitation techniques are directly applicable to SERS. This is because the surface plasmons are wavelength-dependent. Therefore, it is possible that the changes in spectral features will be too significant to be applicable with shifted excitation. Despite this, a number of SERS substrates were procured and the developed system was evaluated for use with these substrates.

6.3.1 SERS Samples

The available literature on the performance of SERS samples varies widely. Therefore, to gain a better understanding of their performance, three samples were tested from three different SERS manufacturers. These manufacturers are the same as described in Section 2.3 and the basic mechanics of how each of them works can be seen there. Given the uncertainty in the literature, the objective was to find a reliable substrate that provided an enhancement and ideally select the one with the strongest enhancement to test with the developed system. The preparation of each of these devices varied greatly and this is described in more detail below:

- **SERSitive [65] Preparation:** 24 hour soak in the analyte followed by a rinse of in DI water or ethanol, then air dry at room temperature.

- **Silmeco [66] Preparation:** Drop the analyte onto the surface of the substrate and let it air dry at room temperature.

- **Enspectr [67] Preparation:** 1 minute soak in the analyte followed by a 1 min rinse in ethanol, then air dry at room temperature.

6.3.2 SERS Measurements

The analyte used for the SERS measurements was Rhodamine 6G (R6G). This substance is typically used as a fluorescent dye in many applications and has a complex Raman spectrum with many features. The strong fluorescence spectrum provides a representative example of many molecules in practical applications. In addition to this, the R6G has a strong affinity to the metal surface based on the HSAB theory as described in Section 2.3. Therefore, it is likely that there will be a significant number of "hotspots" where enhancements can occur. Analytical grade R6G was purchased from Sigma-Aldrich (product #56226). This was mixed with ethanol to achieve a concentration of approximately 0.4 mM or about 200 parts per million (ppm). The sample preparation procedure detailed above was followed for each substrate and they were then mounted onto a fixture for testing in the system. The raw spectrum of each of the samples is shown in Figure 6-6.

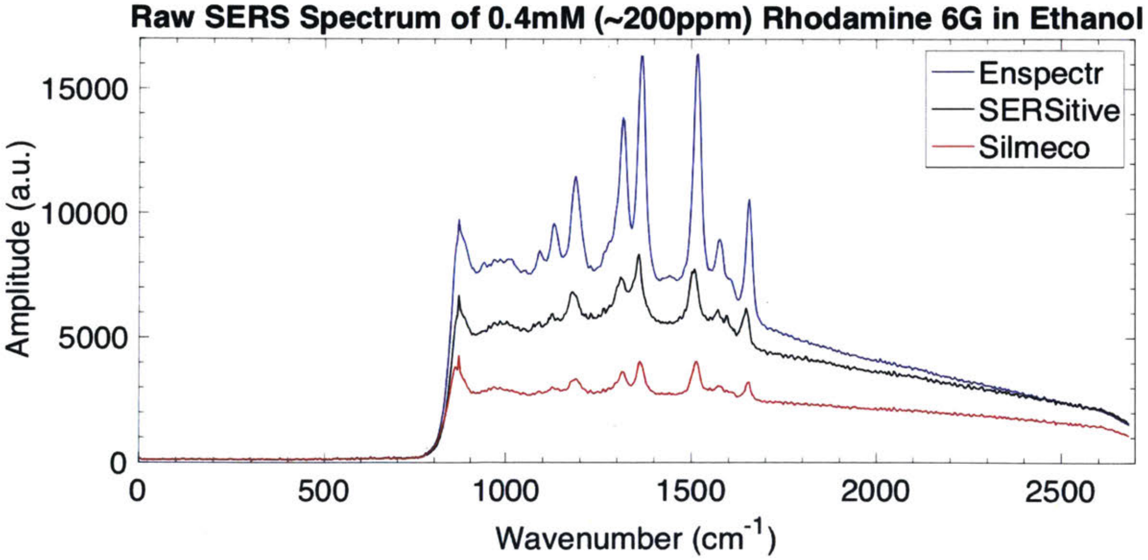

Figure 6-6: Comparison of the SERS devices for 0.4 mM of R6G in ethanol.

As shown in the graph, the strongest enhancement was from the Enspectr device. This could be attributed to the fact that the Enspectr device only contained silver nanoparticles as compared to gold and silver, which were present in the other devices. It is typical for silver to provide a stronger enhancement due to its dielectric properties. Yet, silver substrates have a shorter shelf life, as they tend to corrode, which makes them unusable. Consequently, many companies will provide a gold/silver hybrid or purely gold substrates to significantly increase the shelf life at the expense of a relatively weaker Raman enhancement. After about 10 days, it was noticed that the Enspectr enhancement began to weaken significantly, so timely preparation and measurement is important.

There are other notable aspects that can be pulled from Figure 6-6 as well. The ratio of the Raman scattering intensity to the background/fluorescence signal is not uniform among all the substrates. The Enspectr substrate has a higher ratio of Raman to fluorescence than the other two substrates. This is interesting because it appears as though the surface chemistry can play a role in this relationship. Moreover, the stronger signal from the Enspectr substrates could originate from more scatterers "clinging" to the surface rather than a stronger enhancement in the areas of "hotspots." Ultimately, all of the data acquired from the three SERS devices was promising, but the Enspectr was chosen to test the variable excitation technique with the developed system.

The enhancement factor was computed by estimating the difference in number of molecules involved in the scattering process. Based on this calculation, it was estimated that the minimum enhancement was 10^4. The Raman scatter features of Rhodamine 6G are highlighted for convenience in Figure 6-7. The features vary in both width and height (i.e. signal strength), which makes an ideal sample for testing. In addition, the large sloping background and fluorescence spectrum makes it an ideal test case for using shifted excitation techniques on SERS.

A filter cutoff was placed at approximately 800 cm^{-1}, which masked two additional Raman features located below this value. Two gray boxes in Figure 6-7 highlight the location of these peaks, which will become apparent once the filter is replaced with a lower cutoff. Once it was verified that the SERS spectrum could be obtained and that R6G provided a sufficient sample, the stochastic methods were applied. The

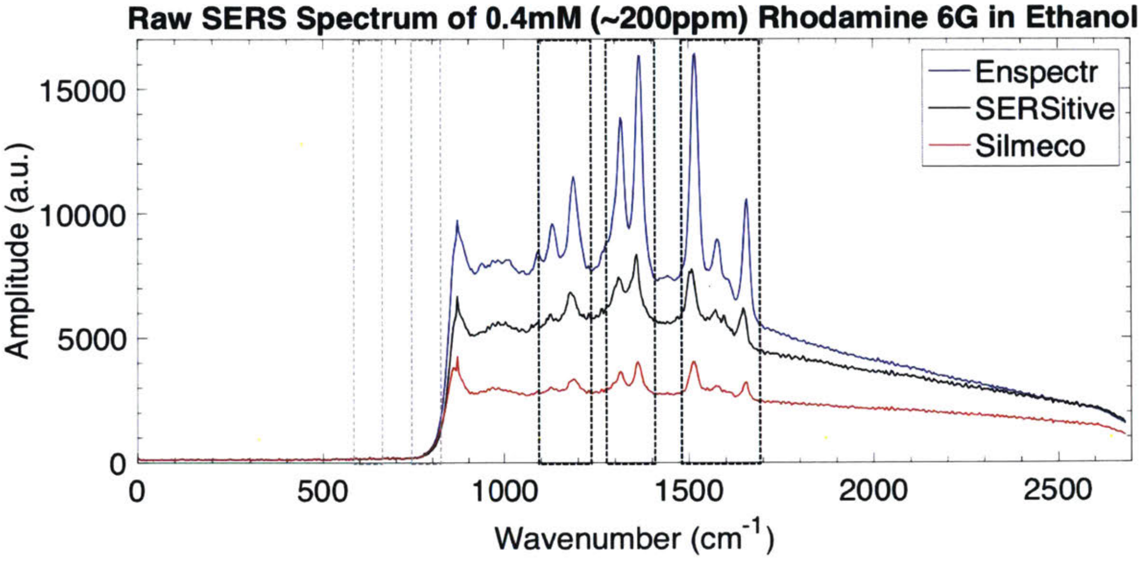

Figure 6-7: Comparison of the SERS devices for 0.4 mM of R6G in ethanol with Raman scatter peaks isolated.

stochastic input vector is shown in Figure 6-8.

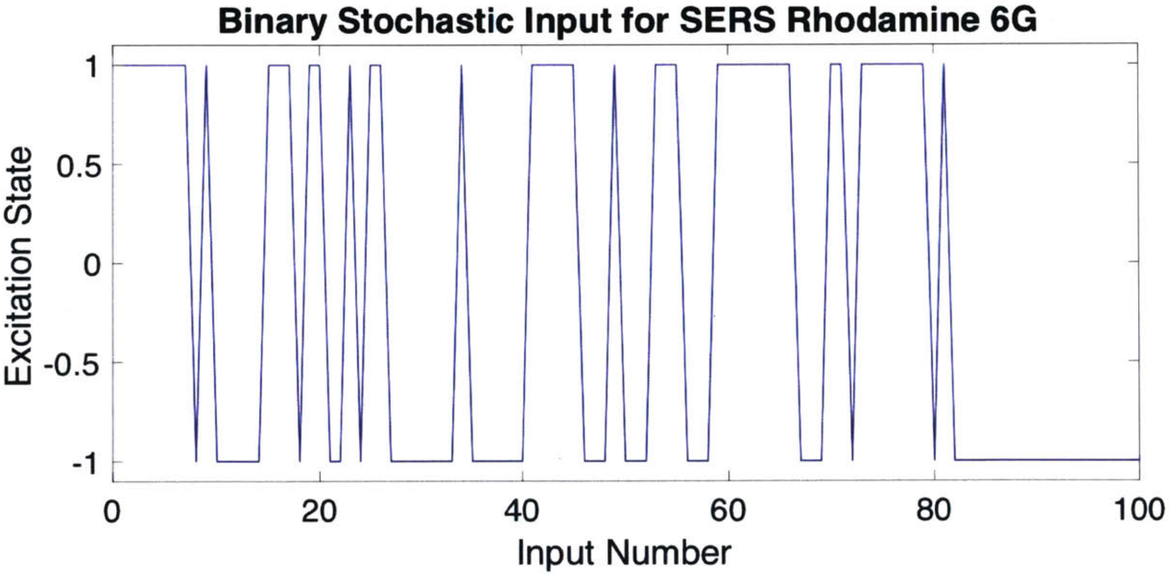

Figure 6-8: Binary stochastic input used for SERS R6G measurement.

The long-pass filter was replaced with one that had a shorter cutoff wavelength so that the additional Raman features would be apparent. In addition, the integration time was reduced such that the Raman features were nearly invisible and the spectrum showed a majority of fluorescence. Figure 6-9 presents two acquired spectra, one with the FBG in the unstrained position and the other with the FBG strained to approximately 850 $\mu\epsilon$, which corresponds to a shift in wavelength of approximately 0.6 nm. The sharp peak located near 900 cm^{-1} is due to a high dark noise pixel and would be a source of a false detection.

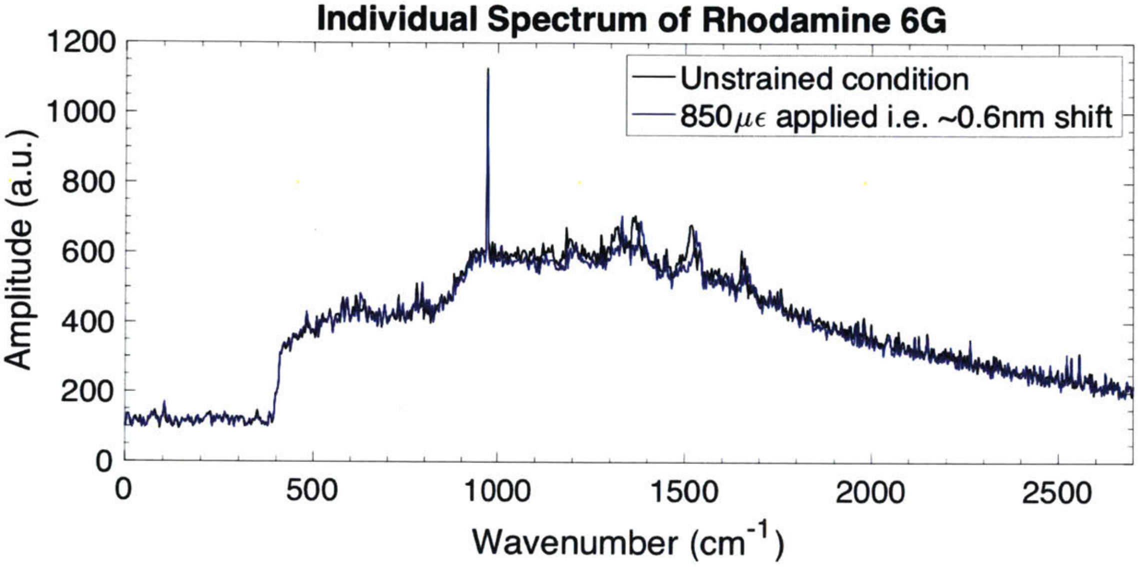

Figure 6-9: Two raw spectrum showing a measurement taken with the FBG unstrained and strained.

The motivation for using the fairly large shift was because the Raman peaks were relatively broad in the R6G sample compared to the sharp Raman feature that was seen in the Diamond sample. Therefore, the larger shift would result in a more significant variation of the pixel amplitude in the locations with Raman scattering. This also tests the limits of the system from multiple aspects. First, the repeatability of the piezo-actuator is indirectly measured as the signal processing method is reliant on repeatable shifts between two excitation states. Second, larger shifts in excitation make the spectral response more likely to change - i.e. this is testing the limits of "Kasha's rule" on the SERS substrate with R6G. Results are shown in Figure 6-10, where the difference spectrum is obtained using the scaled cross-correlation method. A thin dotted line at zero amplitude is shown as reference here as well.

Figure 6-11 shows an overlay of where the Raman peaks were highlighted in the original Raman spectrum from Figure 6-7. From the spectral plot, it is apparent that

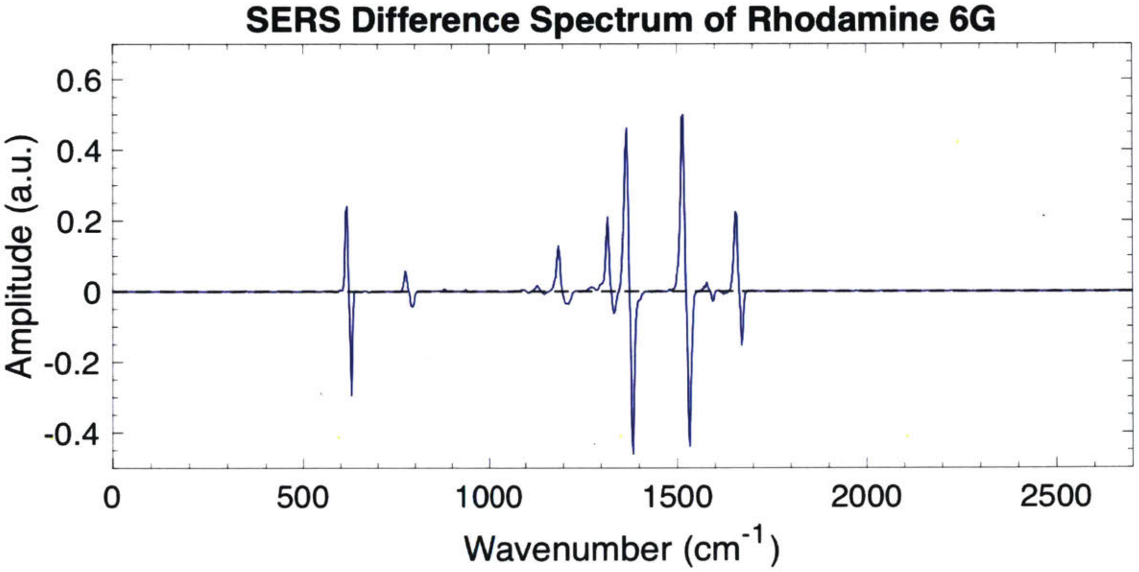

Figure 6-10: Difference spectrum obtained using the scaled cross-correlation of R6G on SERS.

the locations of the peaks are correctly identified. In addition, the relatively high SNR indicates that even with a low quality original spectrum, the derivative features of the Raman spectrum can be obtained.

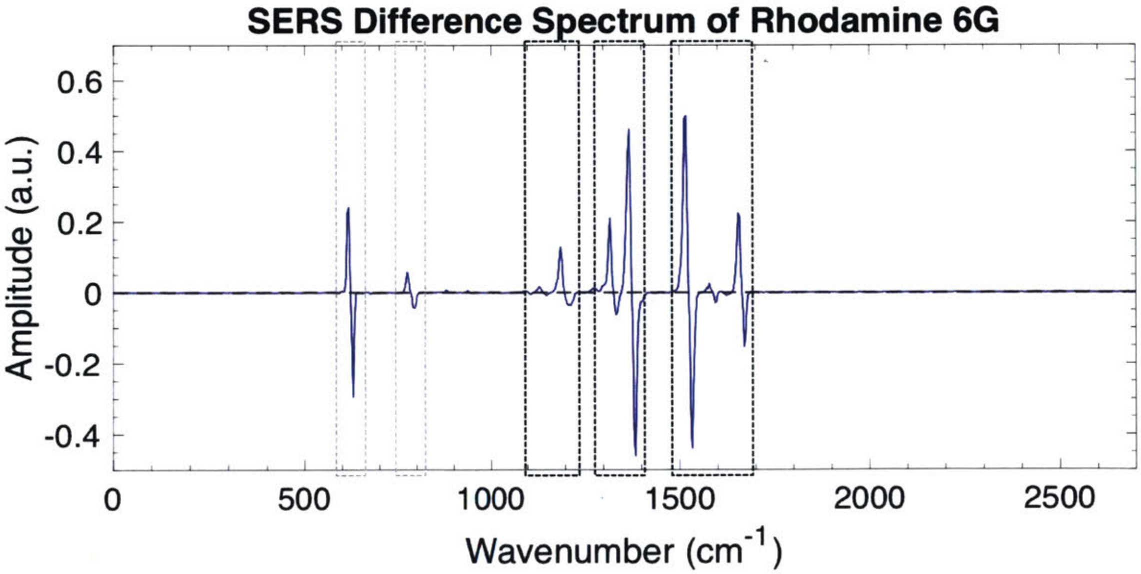

Figure 6-11: Difference spectrum obtained using the scaled cross-correlation of R6G on SERS with Raman scatter peaks isolated.

The features shown in the difference spectrum for the R6G have a similar level of complexity as the original Raman spectrum. Yet, the results prove the use of variable excitation techniques in SERS. Additionally, it shows that this technique can be used to directly address the issues associated with SERS outlined earlier. Finally, this test demonstrates that all elements of the system have been successfully integrated and synchronized, proving out the key functionality of the system. Although the limits of the system were not measured, it was able to detect a strong signal from a concentration of 200 ppm of R6G and it is expected that the system can perform at significantly lower limits of detection given a longer integration time. The final chapter will discuss the potential next steps in this process.

THIS PAGE INTENTIONALLY LEFT BLANK

Chapter 7

Conclusions and Future Work

The following section will summarize the conclusions and outline a path forward for an updated version of the system based on lessons learned through this development process.

7.1 Conclusions

A system was developed that addresses the two main limitations associated with current Raman Spectrometers. These limitations are (1) the relatively low sensitivity and (2) the high false detection rate. There are three main contributions that have resulted from this work:

1. A novel system architecture was developed for a variable excitation Raman Spectrometer. The use of an FBG to modulate the input excitation is a new approach that offers rapid changes in input excitation and more uniformity and control over the input spectrum.

2. New signal processing techniques have been applied in the form of a binary stochastic input with the use of cross-correlation to obtain the difference spectrum. These techniques offer a higher SNR and are more robust than standard methods.

3. The application of shifted excitation techniques to SERS substrates was demonstrated to addresses several of the existing challenges associated with their practical implementation. This enables lower limits of detection and improved sensitivity for a wider range of applications.

Ultimately, this work shows how stochastic excitation techniques can be used to reduce the false detection rate and, when combined with SERS devices, address the low sensitivity problem. Altogether, this work enhances the capabilities in the field of Raman Spectroscopy and opens up new opportunities for device development and testing in a broad range of fields. In addition, this work brings the technology closer towards a compact, miniaturized design through the combined use of the FBG and SLED for variable excitation.

7.1.1 Lessons Learned

The next version of the system could benefit from lessons learned from the existing system. The main opportunity for improvement in the existing system is the amount of power available in the SLED. Development into this is being conducted by a number of companies who manufacture SLED devices in the visible wavelength range. An alternative approach would be to use multiple SLED devices to achieve a higher power at the sample. More power would enable more advanced testing with a wider variety of samples. In addition, this would reduce the integration time and number of samples required to obtain a measurement.

Another consideration to explore for a next generation version of the system would be the relationship between the FBG requirements and detector resolution. There is a balance between the pixel size (i.e. detector resolution) and the FWHM of the reflected beam from the FBG. This relationship could be optimized to maximize the sample power without significantly impacting the spectral resolution. In conclusion, this work proves out the main aspect of the novel design and sets the groundwork for an advanced commercial system that could meet the many needs of users in a broad range of fields.

7.2 Future Work

In general, future work includes the continued improvement of the system through testing of different materials and continued evaluation of the signal processing approach under varied environmental conditions. Along the same lines, the response of the FBG to different environmental factors is important to understand. Altogether there are two main areas for future development: (1) device miniaturization for use in the field and (2) building a more advanced system that is capable of high throughput analysis. The details are described below.

7.2.1 Device Miniaturization

Transitioning from a table top system to a miniaturized device will require the integration of all the individual elements tested throughout this thesis. Mechanical design of the system could be made compact by directly abutting the single-mode fiber with the SLED device. In addition, the length of fiber between the elements would be significantly shorted to miniaturize the path lengths between the circulator and FBG. Combined with smaller optical elements, this would lead to a significantly more compact design.

7.2.2 Multiplexed System for High Throughput Analysis

One of the main benefits of FBGs that has not yet been highlighted is their multiplexing ability, where several FBGs can be connected in series to measure multiple samples at the same time. Figure 7-1 illustrates how a narrow portion of the beam from different parts of the SLED spectrum can be isolated. This multiplexed system could be used to measure multiple samples simultaneously with the use of a single detector. The Raman spectrum could then be decoupled through the use of the cross-correlation methods outlined in the thesis. A conceptual design of this stochastically modulated multiplexed Raman Spectrometer for high throughput chemical analysis is shown in Figure 7-2.

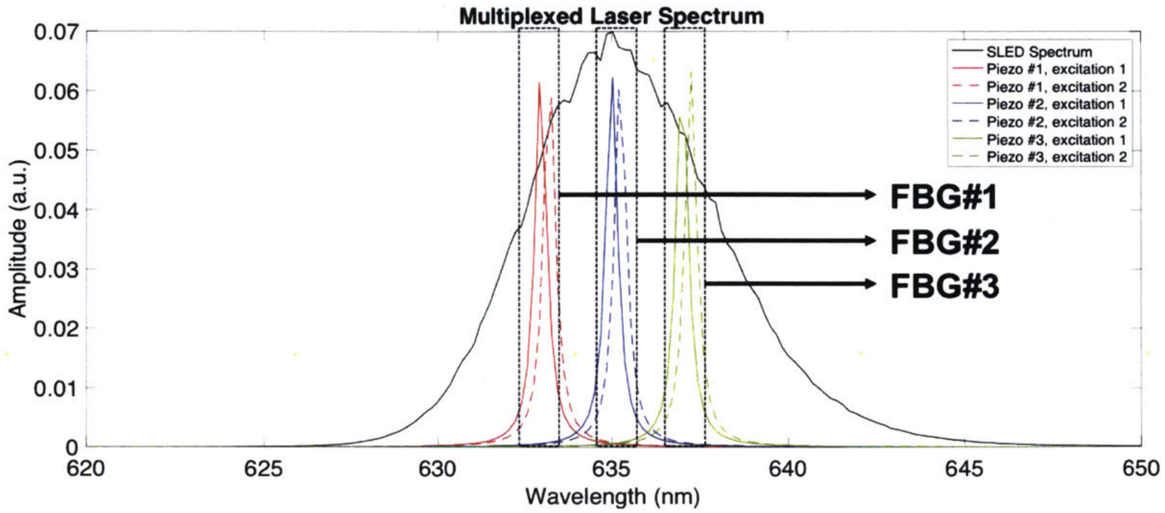

Figure 7-1: Isolated portions of the SLED spectrum using three different FBGs.

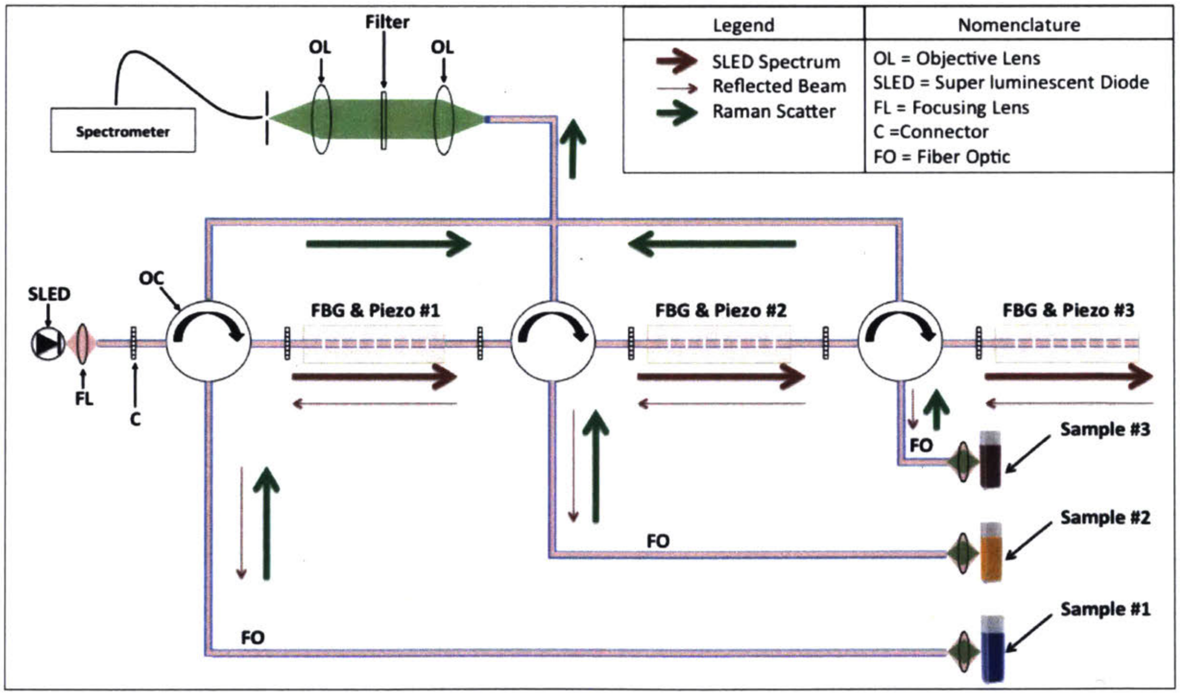

Figure 7-2: Conceptual optical design of a stochastically modulated multiplexed Raman Spectrometer for high throughput chemical analysis.

Existing devices are not able to perform Raman measurements on multiple samples with a single detector. Therefore, this system would be a fundamentally novel type of device that drives down the cost of implementing a high throughput Raman detection system. The advantage is that many samples can be recorded and analyzed simultaneously as compared to the point measurement or localized 2D systems. This opens up significant opportunities in chemical detection, where rapid iterations are required.

THIS PAGE INTENTIONALLY LEFT BLANK

Bibliography

[1] S. J. Ling, J. Sanny, and W. Moebs, *University Physics*. 2016.

[2] R. V. Chimenti, "Excitation source parameters dictate raman spectroscopy outcomes," *Laser Focus World*, vol. 53, no. 1, pp. 76–79, 2017.

[3] R. Larsson, M. Wedborg, and D. Turner, "Correction of inner-filter effect in fluorescence excitation-emission matrix spectrometry using raman scatter," *Anal. Chim. Acta*, vol. 583, no. 2, pp. 357–363, 2007.

[4] `https://oceanoptics.com`.

[5] `https://www.rigaku.com/en/handhelds`.

[6] `http://bwtek.com`.

[7] D. W. Shipp, F. Sinjab, and I. Notingher, "Raman spectroscopy: techniques and applications in the life sciences," *Adv. Opt. Photonics*, vol. 9, no. 2, pp. 315–428, 2017.

[8] R. Shi, X. Liu, , and Y. Ying, "Facing challenges in real-life application of surface-enhanced raman scattering: Design and nanofabrication of surface-enhanced raman scattering substrates for rapid field test of food contaminants," *J. Agric. Food Chem.*, vol. 66, pp. 6525–6543, 2018.

[9] M. S. Schmidt, J. Hubner, and A. Boisen, "Large area fabrication of leaning silicon nanopillars for surface enhanced raman spectroscopy," *Adv. Opt. Mater.*, vol. 24, 2012.

[10] Sersitive, "Sersitive." `https://www.sersitive.eu/wp-content/uploads/2018/08/Product-Sheet.pdf`. Accessed: 2019-01-16.

[11] Y. V. Grishina, V. I. Kukushkin, V. V. Solovyev, and I. V. Kukushkin, "Slow plasmon-polaritons in a bilayer metallic structure revealed by the lower-energy resonances of surface-enhanced raman scattering," *Opt. Express*, vol. 26, no. 17, 2018.

[12] B. O. Inc., "Product overview: Infrared and raman spectrometers." `http://fn-iq.com/wp-content/uploads/2014/04/Bruker-Optic.pdf`. Accessed: 2019-01-11.

[13] M. Maiwald, A. Muller, B. Sumpf, and G. Trankle, "A portable shifted excitation raman difference spectroscopy system: device and field demonstration," *J. Raman Spectrosc*, vol. 47, no. 10, pp. 1765–1775, 2016.

[14] Exalos, "Exalos: High-performance broadband sleds, swept sources and subsystems." `http://www.exalos.com`. Accessed: 2019-01-11.

[15] F. T. GMBH, "Fiber bragg grating (fbg) sensor principle." `https://www.fbgs.com/technology/fbg-principle/`. Accessed: 2019-01-16.

[16] O. Optics, "Qe pro scientific-grade spectrometer installation and operation manual." `https://oceanoptics.com/wp-content/uploads/QEPro.pdf`. Accessed: 2019-01-16.

[17] M. Hajjou, Y. Qin, S. Bradby, D. Bempong, and P. Lukulay, "Assessment of the performance of a handheld raman device for potential use as a screening tool in evaluating medicines quality," *J. Pharm. Biomed. Anal.*, vol. 74, pp. 47–55, Feb. 2013.

[18] S. Elbasuney and A. F. El-Sherif, "Instant detection and identification of concealed explosive-related compounds: Induced stokes raman versus infrared," *Forensic Sci. Int.*, vol. 270, pp. 83–90, Jan. 2017.

[19] M. Lopez-Lopez and C. Garcia-Ruiz, "Infrared and raman spectroscopy techniques applied to identification of explosives," *TrAC, Trends Anal. Chem*, vol. 54, pp. 36–44, 2017.

[20] A. Hakonen, P. O. Andersson, M. S. Schmidt, and T. Rindzevicius, "Explosive and chemical threat detection by surface-enhanced raman scattering: A review," *Anal. Chim. Acta*, vol. 893, pp. 1–13, 2015.

[21] U.S. Food and Drug Administration, "The drug development process." `https://www.fda.gov/forpatients/approvals/drugs/`. Accessed: 2019-01-11.

[22] J. K. Woods, "Aberdeen proving ground advanced planning briefing to industry," tech. rep., Joint Project Manager for Nuclear, Biological, and Chemical Contamination Avoidance, Feb. 2016.

[23] M. A. Weibel, "Needs and challenges in the field detection and identification of military chemical threats," tech. rep., Joint Project Manager for Nuclear, Biological, and Chemical Contamination Avoidance, Sept. 2015.

[24] M. S. Center, "Mass spectrometry." `http://chemistry.emory.edu/msc/tutorial/mass-spectrometry.html`. Accessed: 2019-01-11.

[25] R. S. of Chemistry, "Ultraviolet - visible spectroscopy," tech. rep., Royal Society of Chemistry, 2009.

[26] S. M. Ali, F. Bonnier, H. Lambkin, K. Flynn, and V. McDonagh, "A comparison of raman, FT-IR and ATR-FT-IR micro spectroscopy for imaging human skin tissue sections.," *Analytical Methods*, vol. 5, pp. 2281–2291, 2013.

[27] N. Corporation, "FT-IR spectroscopy." `https://www.newport.com/n/introduction-to-ftir-spectroscopy`.

[28] D. A. Long, *The Raman Effect: A unified treatment of the theory of Raman Scattering in molecules.* Chichester, New York: Wiley, 2002.

[29] H. Rigneault and P. Berto, "Tutorial: Coherent raman light matter interaction processes," *APL Photonics*, vol. 3, no. 9, 2018.

[30] R. W. Boyd, *Nonlinear Optics.* Academic Press, second ed., 2003.

[31] S. Marshall and J. B. Cooper, "Quantitative raman spectroscopy when the signal-to-noise is below the limit of quantitation due to fluorescence interference: Advantages of a moving window sequentially shifted excitation approach," *Appl. Spectrosc*, vol. 70, no. 9, pp. 1489–1501, 2016.

[32] E. L. Izake, "Forensic and homeland security applications of modern portable raman spectroscopy," *Forensic Sci. Int.*, vol. 202, pp. 1–8, Apr. 2010.

[33] J. Jehlicka, A. Culka, P. Vandenabeele, and H. G. Edwards, "Critical evaluation of a handheld raman spectrometer with near infrared (785nm) excitation for field identification of minerals," *Spectrochim. Acta, Part A*, vol. 80, pp. 36–40, 2011.

[34] S. Zhang, *Raman Spectroscopy and its Application in Nanostructures.* United Kingdom: John Wiley & Sons Ltd., 2012.

[35] C. Muehlethaler, M. Leona, and J. R. Lombardi, "Towards a validation of surface-enhanced raman scattering (sers) for use in forensic science: repeatability and reproducibility experiments," *Forensic Sci. Int.*, vol. 268, pp. 1–13, 2013.

[36] M. T. Cicerone and C. H. Camp, Jr., "Histological coherent raman imaging: a prognostic review," *Analyst*, vol. 143, no. 33, 2017.

[37] Y. J. Lee, S. L. Vega, P. J. Patel, K. A. Aamer, P. V. Moghe, and M. T. Cicerone, "Quantitative, label-free characterization of stem cell differentiation at the single-cell level by broadband coherent anti stokes raman scattering microscopy," *Tissue Eng Part C Methods*, 2013.

[38] E. C. L. Ru and P. G. Etchegoin, *Principles of Surface-Enhanced Raman Spectroscopy and related Plasmonic effects.* Great Britain: Elsevier, 2009.

[39] A. Alfarra, E. Frackowiak, and F. Beguin, "The hsab concept as a means to interpret the adsorption of metal ions onto activated carbons," *Appl. Surf. Sci.*, vol. 228, pp. 84–92, 2004.

[40] S. Mahajan, R. M. Cole, J. D. Speed, S. H. Pelfrey, A. E. Russell, P. N. Bartlett, S. M. Barnett, and J. J. Baumberg, "Understanding the surface-enhanced raman spectroscopy background," *J. Phys. Chem. C*, vol. 114, no. 6, pp. 7242–7250, 2010.

[41] J. Chen, X. Zheng, H. Wang, and W. Zheng, "Graphene oxide-ag nanocomposite: In situ photochemical synthesis and application as a surface-enhanced raman scattering substrate," *Thin Solid Films*, vol. 520, no. 1, pp. 179–185, 2011.

[42] J. Kostamovaara, J. Tenhunen, M. Kogler, J. Nissinen, and P. Keranen, "Fluorescence suppression in raman spectroscopy using a time-gated cmos spad," *Opt. Express*, vol. 21, pp. 31632–31645, 2013.

[43] F. Knorr, Z. J. Smith, and S. Wachsmann-Hogiu, "Development of a time-gated system for raman spectroscopy of biological samples," *Opt. Express*, vol. 18, pp. 20049–20058, 2010.

[44] H. Cheng-Yu, Z. Yi-Fan, Z. Meng-Xi, L. L. M. Gordon, and L. Li-Qiang, "Application of fbg sensors for geotechnical health monitoring, a review of sensor design, implementation methods and packaging techniques," *Sens. Actuators A Phys.*, vol. 244, pp. 184–197, 2016.

[45] M. Majumder, T. K. Gangopadhyay, A. K. Chakraborty, K. Dasgupta, and D. Bhattacharya, "Fibre bragg gratings in structural health monitoring—present status and applications," *Sens. Actuators A Phys.*, vol. 147, pp. 150–164, 2008.

[46] K. Bremer, M. Meinhardt-Wollweber, T. Thiel, G. Werner, T. Sun, K. Grattan, and B. Roth, "Sewerage tunnel leakage detection using a fibre optic moisture-detecting sensor system," *Sens. Actuators A Phys.*, vol. 220, pp. 62–68, 2014.

[47] J. Krasiński and G. Pearson, "Optical nonreciprocal devices and their applications," *Acta Phys. Pol. A*, vol. 86, 1994.

[48] M. M. Werneck, R. C. S. B. Allil, B. A. Ribeiro, and F. V. B. de Nazaré, "A guide to fiber bragg grating sensors," 2013.

[49] U. Nawrot, T. Geernaert, B. D. Pauw, D. Anastasopoulos, E. Reynders, G. D. Roeck, and F. Berghmans, "Development of a mechanical strain amplifying transducer with bragg grating sensor for low-amplitude strain sensing," *Smart Mater. Struct.*, vol. 26, no. 7, 2017.

[50] R. L. McCreery, *Raman Spectroscopy for Chemical Analysis.* New York: John Wiley & Sons, Inc., 2000.

[51] `https://www.mathworks.com/products/matlab.html`.

[52] `http://www.novae-laser.com`.

[53] `https://www.ascentta.com`.

[54] `http://www.exalos.com`.

[55] `https://www.mitutoyo.com`.

[56] `https://www.thorlabs.com`.

[57] `https://www.piceramic.com/en/`.

[58] E. Optics, "Understanding spatial filter." `https://www.edmundoptics.com/resources/application-notes/lasers/understanding-spatial-filters/`. Accessed: 2019-01-16.

[59] A. Khetani, A. Momenpour, and H. Anis, "Hollow core photonic crystal fiber as a robust raman biosensor," *Optics Express*, vol. 21, no. 10, 2013.

[60] S.-C. Her and C.-Y. Huang, "The effects of adhesive and bonding length on the strain transfer of optical fiber sensors," *Appl. Sci.*, vol. 6, no. 13, 2016.

[61] M. N. Cohen, *Pulse Compression in Radar Systems.* Boston, MA: Springer, 1987.

[62] T. V. Vorburger, J. F. Song, W. Chu, L. Ma, S. H. Bui, Z. Zheng, and T. B. Renegar, "Applications of cross-correlation functions," *Wear*, vol. 271, pp. 529–533, 2011.

[63] P. Z. Marmarelis and V. Z. Marmarelis, *Analysis of Physiological Systems: The White-Noise Approach.* New York: Plenum Press, 1978.

[64] P. A. Mosier-Boss, S. H. Lieberman, and R. Newbery, "Fluorescence rejection in raman spectroscopy by shifted-spectra, edge detection, and fft filtering techniques," *Appl. Spectrosc.*, vol. 49, no. 5, 1995.

[65] `https://www.sersitive.eu`.

[66] `https://www.silmeco.com`.

[67] `http://enspectr.com`.

[68] P. Rostron, S. Gaber, and D. Gaber, "Raman spectroscopy, review," *Int. J. Eng. Tech.*, vol. 6, no. 1, 2016.

[69] K. Eberhardt, C. Stiebing, C. Matthaus, M. Schmitt, and J. Popp, "Advantages and limitations of raman spectroscopy for molecular diagnostics: an update," *Expert Rev. Mol. Diagn.*, vol. 15, pp. 773–787, 2015.

[70] J. R. Ferraro, K. Nakamoto, and C. W. Brown, *Introductory Raman Spectroscopy.* San Diego, California: Academic Press, 2003.

[71] S. E. J. Bell, E. S. O. Bourguignon, and A. Dennis, "Analysis of luminescent samples using subtracted shifted raman spectroscopy," *Analyst*, vol. 123, pp. 1729–1734, 1998.

[72] B. L. Volodin, S. Dolgy, V. S. Ban, D. Gracin, K. Juraić, and L. Gracin, "Application of the shifted excitation raman difference spectroscopy (serds) to the analysis of trace amounts of methanol in red wines," in *Biomedical Vibrational Spectroscopy VI: Advances in Research and Industry* (A. Mahadevan-Jansen and W. Petrich, eds.), vol. 8939 of *Proc. of SPIE*, (San Francisco, California), Mar. 2014.

[73] J. Zhao, M. M. Carrabba, and F. S. Allen, "Automated fluorescence rejection using shifted excitation raman difference spectroscopy," *Appl. Spectrosc.*, vol. 56, no. 7, pp. 834–845, 2002.

[74] M. Maiwald, B. Eppich, A. Ginolas, B. Sumpf, G. Erbert, and G. Tränkle, "Compact handheld probe for shifted excitation raman difference spectroscopy with implemented dual-wavelength diode laser at 785 nanometers," *Appl. Spectrosc.*, vol. 69, no. 10, pp. 1144–1151, 2015.

[75] M. N. Leger and A. G. Ryder, "Comparison of derivative preprocessing and automated polynomial baseline correction method for classification and quantification of narcotics in solid mixtures," *Appl. Spectrosc.*, vol. 60, no. 2, pp. 182–193, 2006.

[76] E. Cordero, F. Korinth, C. Stiebing, C. Krafft, I. W. Schie, and J. Popp, "Evaluation of shifted excitation raman difference spectroscopy and comparison to computational background correction methods applied to biochemical raman spectra," *Sensors*, vol. 17, 2017.

[77] S. Tiwari, N. J. Vasa, and B. Srinivasan, "Fiber bragg grating-based wavelength modulation spectroscopy technique for trace gas sensing," in *Optical Sensing and Detection IV* (F. Berghmans and A. G. Mignani, eds.), vol. 9899 of *Proc. of SPIE*, (Brussels, Belgium), 2016.

[78] J. S. Greer, G. I. Petrov, and V. V. Yakovlev, "Raman spectroscopy with led excitation source," *J. Raman Spectrosc.*, vol. 44, pp. 1058–1059, 2013.

[79] M. A. da Silva Martins, D. G. Ribeiro, E. A. P. dos Santos, A. A. Martin, A. Fontes, and H. da Silva Martinho, "Shifted-excitation raman difference spectroscopy for in vitro and in vivo biological samples analysis," *Biomed. Opt. Express*, vol. 1, no. 2, pp. 617–626, 2010.

[80] Y. nan Zhang, Y. Zhao, and Q. Wang, "Low-cost and high-precision measurement of gas concentration by the way of wavelength modulation spectroscopy," *Optik*, vol. 126, pp. 4527–4530, 2015.

[81] A. C. D. Luca, K. Dholakia, and M. Mazilu, "Modulated raman spectroscopy for enhanced cancer diagnosis at the cellular level," *Sensors*, vol. 15, pp. 13680–13704, 2015.

[82] L. Wang, J. Wang, D. Bao, R. Yang, Q. Yan, F. Gao, and D. Hua, "Optimization design of the tuning method for fbg spectroscopy based on the numerical analysis

of all-fiber raman temperature lidar," *Opt. Fiber Technol.*, vol. 40, pp. 165–171, 2018.

[83] M. Buric, J. Falk, and K. P. Chen, "Piezo-electric tunable fiber bragg grating diode laser for chemical sensing using wavelength modulation spectroscopy," *Opt. Express*, vol. 14, no. 6, 2006.

[84] C. Conti, A. Botteon, M. Bertasa, C. Colombo, M. Realinia, and D. Sali, "Portable sequentially shifted excitation raman spectroscopy as an innovative tool for in situ chemical interrogation of painted surfaces," *Analyst*, vol. 141, pp. 4599–4607, 2016.

[85] S. Marshall and J. B. Cooper, "Quantitative raman spectroscopy when the signal-to-noise is below the limit of quantitation due to fluorescence interference: Advantages of a moving window sequentially shifted excitation approach," *Appl. Spectrosc.*, vol. 70, no. 9, pp. 1489–1501, 2016.

[86] S. Guo, O. Chemavskaia, J. Popp, and T. Bocklitz, "Spectral reconstruction for shifted-excitation raman difference spectroscopy (serds)," *Talanta*, vol. 186, pp. 372–380, 2018.

[87] S. Gui, O. Chernavskaia, J. Popp, and T. Bocklitz, "Spectral reconstruction for shifted-excitation raman difference spectroscopy (serds)," *Talanta*, vol. 186, pp. 372–380, 2018.

[88] K. Divya, K. Sulochana, and N. J. Vasa, "Superluminescent diode-based multiple-gas sensor for nh_3 and h_2o vapor monitoring," *IEEE J. Sel. Top. Quantum Electron.*, vol. 18, no. 5, pp. 1540–1546, 2012.

[89] A. E. Villanueva-Luna, J. Castro-Ramos, S. Vazquez-Montiel, A. Flores-Gil, J. A. Delgado-Atencio, and E. E. Orozco-Guillen, "Fluorescence and noise subtraction from raman spectra by using wavelets," *Optical Memory and Neural Networks (Information Optics)*, vol. 19, no. 4, pp. 310–317, 2010.

[90] Y. Jiang, J. Wang, L. Malfatti, D. Carboni, N. Senes, and P. Innocenzi, "Highly durable graphene-mediated surface enhanced raman scattering (g-sers) nanocomposites for molecular detection," *Appl. Surf. Sci.*, vol. 450, pp. 451–460, 2018.

[91] A. C. D. Luca, M. Mazilu, A. Riches, C. S. Herrington, and K. Dholakia, "Online fluorescence suppression in modulated raman spectroscopy," *Anal. Chem.*, vol. 82, pp. 738–745, 2010.